THE UNIVERSITY OF CALGARY

MOLECULAR HYDROGEN IN PLANETARY NEBULAE

by

Chengguang Li

A THESIS

SUBMITTED TO THE FACULTY OF GRADUATE STUDIES

IN PARTIAL FULFILMENT OF THE REQUIREMENTS FOR THE

DEGREE OF MASTER OF SCIENCE

DEPARTMENT OF PHYSICS AND ASTRONOMY

CALGARY, ALBERTA

January 1998

ABSTRACT

2.12μm and 2.14μm narrow band images and photometries of fifteen planetary nebulae are presented in this thesis. Eight of them show H_2 V1-0S(1) emission and Four are new detections. They are NGC6881, Hu2-1, Frosty Leo and IC4997. Statistics of about seventy reported molecular hydrogen detections confirmed the strong correlation between morphological types and H_2 emissions. A correlation between H_2 emission and central star masses of planetary nebulae is found.

Acknowledgements

Here I would like to thank those who helped me over the past two years. Many of the results of this thesis would never have been obtained without their guidances and helps.

First of all and foremost, I am indebted to my supervisor, Dr. Sun Kwok for his many aspects support: introducing me to the topics of the thesis, providing the observation data, giving me constructive criticism and suggestion, and pushing me going ahead, ... I also thank to him for his financial support during the period when most part of this work was done.

I would like to thank Dr. Bruce Hrivnak who helped me much more in beginning the data reduction. Without his help, the data reduction would be finished much later.

I also deeply thank Dr. Kevin Volk who have helped me in data reduction and given me many useful suggestions and advices not only during the period in which he was my interim supervisor but also during the period of completing this thesis. I also thank him giving me some data used in this thesis.

Also I thank Dr. Cheng-Yue Zhang helping me use IRAF and teaching me many useful techniques not only in data reduction but also in using the computing facilities.

Finally I want to thank Dr. D. Leahy and Dr. D. Hobill who gave me good constructive criticism and advice on this thesis.

Table of Contents

List of Tables

List of Figures

List of Plates

α_g	reaction rates for H+H surface reaction
γ_{ij} or γ_{ji}	collisional de-excitation or excitation rate
ε	emissivities
μ	reduced mass
$\mu(R)$	dipole moment
ν_0	characteristic vibration period
$\sigma_1(\nu)$	photon absorption cross section
χ_e	constant in vibration energy
ω_e	frequency
Γ	cascade entry rate
ψ	wavefunction
a_1, a_2, a_3, a_4	Dunham potential coefficients
a.u.	atomic unit
f_i	the fractional population of level i
g_i, g_j	statistical weight
n_0	total hydrogen number density
n_{crit}	critical number density
r_i, r_j	electrons position
t_{ev}	the thermal evaporation time
t_g^{-1}	formation rate of H_2

t_s	the sticking time
y_e	constant in vibrational energy
A_{ij}	Einstein A-coefficient
ADU	Analog-Digital Unit
AFGL	Air Force Geophysical Laboratory
AGB	Asymptotic Giant Branch
B(R)	$1/(2\mu R^2)$
BPN	bipolar planetary nebula
B_v, D_v, H_v, L_v, M_v	constants in rotational energy
D	the binding energy
D_e	constant in the Morse function
E	eigenvalue or energy
E_e	electronic energy
E_{rot}	rotation energy
E_{vib}	vibration energy
E_i, E_j	energy level
F	flux
(G_c)	cooling rate
$G_{n,J}$	the vibrational term values
H	Hamiltonian operator
H-R	Hertzsprung-Russell
I	intensity

IC	Infrared Catalogue
IRAF	Image Reduction and Analysis Facility
ISW	Interacting Stellar Winds
KPNO	Kitt Peak National Observatory
L_*	luminosity
$L_\odot$	luminosity of the sun
LTE	Local Thermal Equilibrium
M	dipole or quadrupole moment
M_α	nuclei mass
$M_\odot$	mass of the sun
NIR	Near-InfraRed
NOAO	National Optical Astronomical observatory
PDR	Photo Dissociation Region
P_{ic}, Q_{ic}	collisional dissociation rate from level i
P_{ij}, Q_{ij}	convertion rate from thermal energy into the internal energy
PN	Planetary Nebula
PPN	Proto-Planetary Nebula
Q	Quadrupole moment
R	distance of two nuclei
R(v"J", v'J')	rate of absorption
R_α, R_β	nuclei position
R_e	the equilibrium distance

T_e	kinetic energy of the electrons
T_n	kinetic energy of the nuclei
V(R)	potential energy
V_{ee}	Coulomb interaction energy among electrons
V_{en}	Coulomb interaction energy among electrons and nuclei
V_{nn}	Coulomb interaction energy among nuclei
VLA	Very Large Array
$X^1\Sigma_g^+$	ground state of H_2
Y_{lm}	spherical harmonic function
Z_α, Z_β	nuclei charge
ZAMS	Zero Age Main Sequence

Chapter 1 Introduction

1.1 A Brief Description of Evolution of a Solar Mass Star

It is believed that stars are born from the gravitational contraction of interstellar clouds of gas and dust. As an interstellar clouds contracts, gravitational potential energy is converted in part to thermal energy and in part to radiative energy. Eventually, the core heats up to the ignition temperature of fusion reactions, and a star is truly born. Prior to that event, the star goes through protostar and pre-main-sequence stages. The contracting cloud is a protostar before it establishes hydrostatic equilibrium. Between that stage and the ignition of fusion reactions, it is called a pre-main-sequence (PMS) star. The evolutionary path for protostars of different masses differ. Despite detailed differences, the theoretical calculations have the following common features: (1) the collapse starts out in free fall; that is, it is controlled only by gravity; (2) it proceeds very unevenly, for the central regions collapse more rapidly than the outer parts and a small condensation in hydrostatic equilibrium forms at the center; (3) once the core forms, it accretes material from the infalling envelope; (4) the star becomes visible to us either by accreting all the surrounding material onto itself or by somehow dissipating it. A PMS star shines by slowly shrinking and accreting. At this stage, the star's temperature is so low that its opacity is relatively high (even though its density is low). As the PMS star shrinks in size, the surface temperature at first does not change very much, and the luminosity decreases. Meanwhile the core continues to heat up. As it does, the interior reaches a

high enough temperature so that the opacity becomes low enough for radiation rather than convection to transport energy most efficiently. The zone of radiative transport starts at the core and slowly creeps outward as the inner layers heat up. Eventually the core heats up to a few million kelvins, high enough to start thermonuclear reactions. When the PMS star gets most of its energy from thermonuclear reactions rather than gravitational contraction, it is a truse star. It no longer contracts to provide energy; the heat from fusion reactions keeps it in hydrostatic equilibrium. The star is now called a zero age main-sequence (ZAMS) star. It settles down to the longest stage, the main-sequence star, in its life, calmly converting hydrogen to helium in its core. Most of the interior transports energy by radiation; only the outer region of the envelope is convective. Eventually the core hydrogen is exhausted. As a result of the gravitational contraction of the core, material just beyond the core is pulled into higher-temperature regions and hydrogen burning starts in a shell surrounding the helium core. The core is so dense that it supports the weight of material above it. When this equilibrium ends, the core contracts much more rapidly and heats up. When this happens, energy generation in the shell is accelerated and the outer envelope expands. During the last part of the expansion phase, convection develops in the envelope and the luminosity increases. This begins the red giant phase of the star's life. Temperatures in the interior continue to rise owing to core contraction. In the red giant, the rising core temperature eventually hits the minimum to start helium nuclear reactions by the triple-alpha process (a thermonuclear process in which three helium are fused into one carbon nucleus). This helium core is dense and degenerate. Once part of it has ignited, the energy spreads rapidly throughout the core

because a degenerate gas is a good conductor of heat. The rest of the core quickly ignites. The increased temperature runs up the rate of the triple-alpha process, generating more energy, further increasing the temperature, and so on. This runaway process is called the helium flash. The whole process is completed in a very short time-perhaps only a few minutes! The star now burns helium in the core and hydrogen in a layer around the core. This phase is the helium-core-burning analog to the star's main-sequence phase (that of hydrogen core burning). Eventually the triple-alpha process converts the core to carbon. The reaction stops in the core but continues in a shell around it. This situation--core shut down but the thermonuclear reactions going on in a shell--resembles that of the star when it first evolves off the main sequence. The burning shell makes the star expand. The star again becomes a red giant. The star shifts from blue to red and becomes markedly brighter. This is the asymptotic giant branch (AGB). The helium-burning shell becomes unstable. Bursts of triple-alpha energy cause thermonuclear explosions in the shell. Meanwhile, the star has developed a very strong outflow of mass from its surface, sometimes called a superwind to distinguish it from the normal stellar wind of a red giant. A hot core is left behind. The expelled material forms an expanding shell of gas, which we call a planetary nebula, heated by the hot core. The hot core appears as the central star of a planetary nebula. The nebula keeps expanding until it dissipates in the interstellar medium. The core never reaches the ignition temperature of carbon burning because the core has become degenerate and cannot contract and heat up to ignite carbon burning. Then it forms a white dwarf star.

So planetary nebulae (PNe) are expanding gaseous shells ejected from a star in the evolutionary transition phase from the red giant to the white dwarf stage. The name "planetary nebulae" came into use because the astronomers who first observed these nebulae through small telescopes thought the images resembled those of planets (Jovian). We know that planetary nebulae have no connection with planets or solar systems, but the name has persisted.

1.2 Interacting Stellar Winds Model

The commonly accepted model for the formation of planetary nebulae is the interacting stellar winds (ISW) model (Kwok, Purton & Fitzgerald 1978; Kwok 1982, 1994; Kahn 1983; Balick 1987; Balick, Preston & Icke 1987; Aller 1993).

The wind phenomenon can be divided in various phases following the evolution of the star. We can distinguish four main phases, each possibly with its own dominant mechanism for the production of the wind. Within each phase, some sub-phases might be identified from the specific stellar structure, which implies particular properties for the outer layers too, and consequently for the character of the wind. We have, in sequence: phase I, with sub-phases Ia (first red giant branch), Ib (horizontal branch), Ic (early asymptotic giant branch); phase II, with subphases IIa (pulsed asymptotic giant branch), and IIb (transition from the AGB up to the end of the "superwind" phase); phase III, which represents the remaining transition up to the appearance of the optical nebula to

which the proto-PN objects and the optically bright post-AGB stars belong; and phase IV, with sub-phase IVa (stellar luminosity approximately constant from the value at the end of the AGB phase down to 0.9 of it) and IVb (fading phase: stellar luminosity declines to 0.1 of the final value on the AGB). In this phase, with the regular optically visible nebula coming out, the central star exhibits a wind much faster than in the previous phases: it is called the fast wind. The evolutionary path in the Hertzsprung-Russell (H-R) diagram is shown in Fig.1.1. H-R diagram is a representation of the classification of stars according to their spectral class (or color or surface temperature) and luminosity (or absolute magnitude); the physical properties of a star are correlated with its position on the diagram, so a star's evolution can be described by its position on the diagram with time.

A solar mass star, while on the AGB phase, losses mass steadily through a wind with a velocity of about 10 km/s, and mass-loss rate $dM/dt = 10^{-4}$ to 10^{-5} $M_\odot$/yr. Toward the end of the asymptotic giant branch stage, the star switches to losing mass in the form of a fast wind with a velocity rising up to around 2000 km/s, albeit with a lower mass-loss rate of 10^{-8} to 10^{-6} $M_\odot$/yr. The fast wind catches up with the slow wind and drives a shocked shell through it. Wind mechanism for AGB stars can be generally clasified into (1) thermally driven, (2) wave driven, and (3) radiation pressure driven models.

A contact discontinuity is formed at the interface between the (shocked) slow and fast winds. The slow wind shell is identified with the visible boundary of the PN. The outer

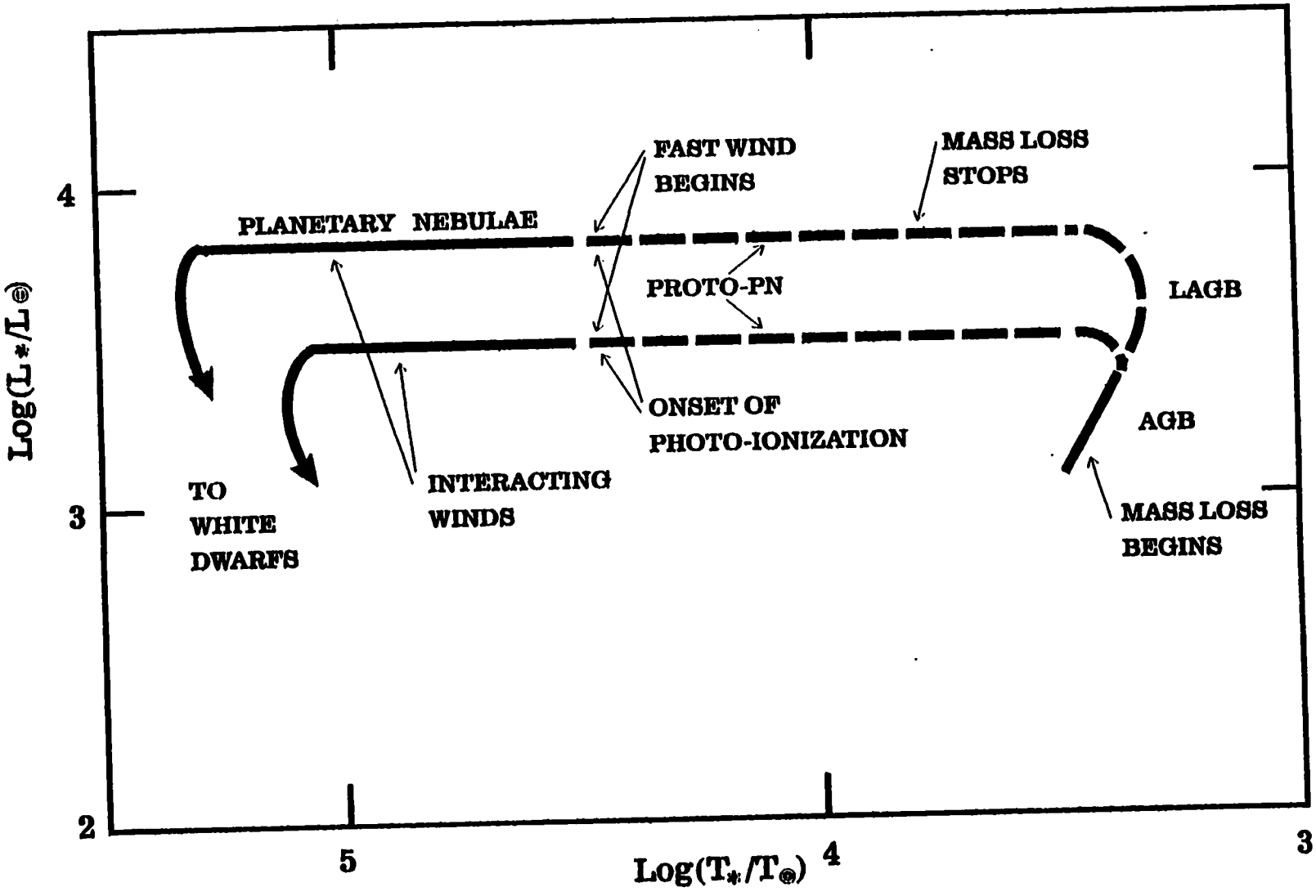

Fig. 1. Evolutionary paths from AGB to PN in the H-R diagram .

edge of the shell is the outward moving shock, whereas the contact discontinuity separates the shell from the shocked fast wind material. The unshocked fast wind material gives rise to a reverse shock. The high density shell built up at the interface of the two winds, over a period of several thousand years, will have all the observed properties of a planetary nebula. Fig.1.2 shows the interacting-winds model.

The importance of the winds in these various phases for the evolution of the central stars of planetary nebulae and for the relationship with the presently observed nebulae and with their history has been widely recognized. A great deal of work has been done in the specific area of the hydrodynamics of the interaction of the various type of winds, with the aim of explaining the morphology in "groups" of PNe as well as for individual objects.

A well understanding of PNe needs to take the central star and its circumstellar material as a whole thing, an evolutionary system.

1.3 Molecular Hydrogen Observation in Planetary Nebulae

With the advent of wide-field array detectors operating in the near-infrared (near-IR) spectral region, a new and potentially critical tool for the study of PNe is available. While PNe emit throughout the electromagnetic spectrum, the near-IR has many advantages over other wavelengths. The near-IR provides lower attenuation to important

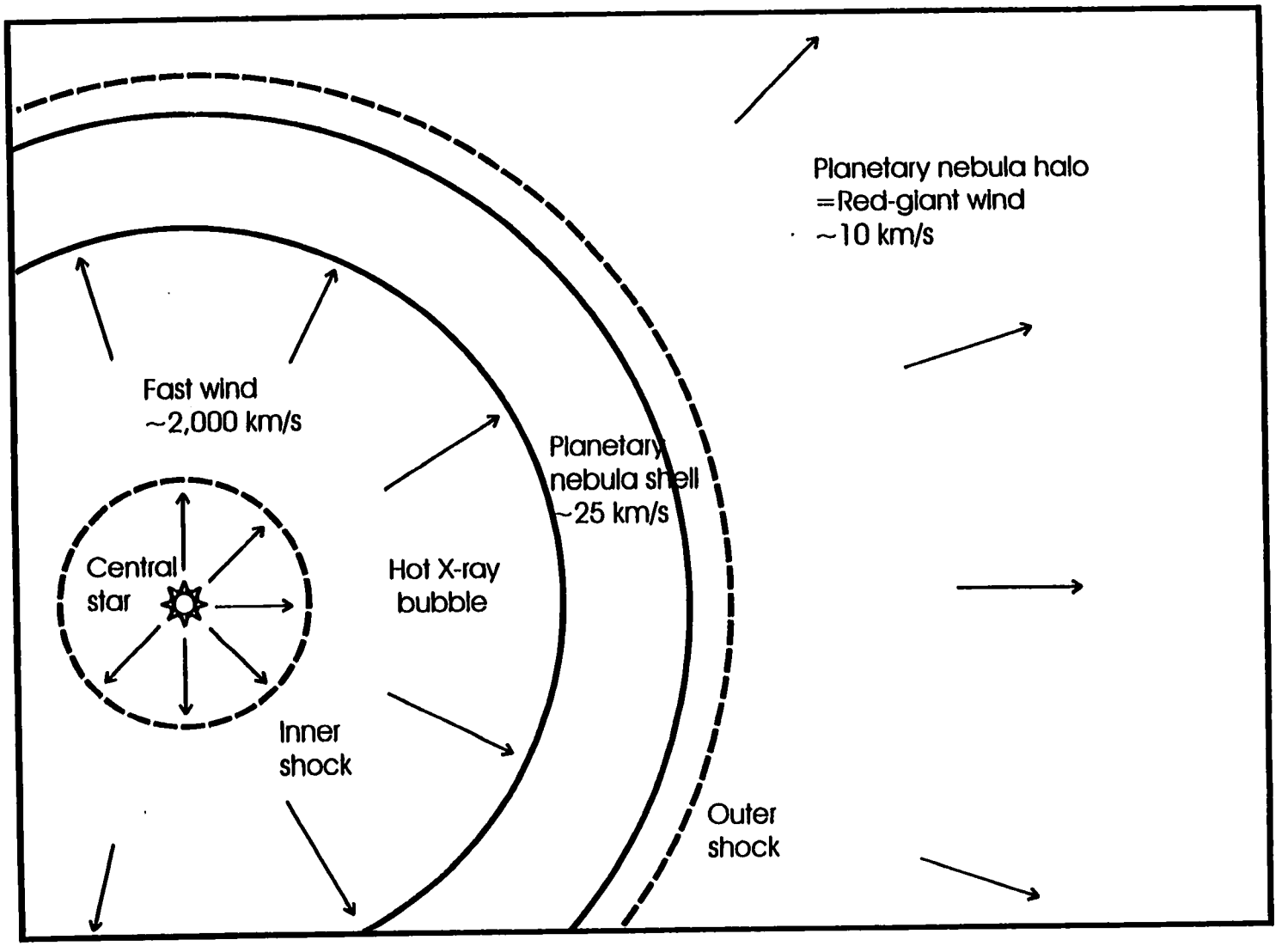

Fig. 1.2. Interacting Stellar Winds Model (ISW).

dense regions than the visible. Atmospheric seeing at near-IR wavelengths is typically reduced to high spatial resolution, this can help to resolve structure that is not normally seen at the shorter wavelengths. Many transitions from vibrationally excited H_2 fall in the near-IR. The ideas of mass loss discussed above suggest that there may be fairly large neutral shells around PNe, and that these shell might well contain molecules. Even they are easily destroyed by the intense UV radiation, in dense clumps, H_2 molecules can survive and be excited.

The first detection of infrared rotation-vibration lines of molecular hydrogen from a planetary nebula was made in 1976 by Treffers (1976). Since that time, over 70 planetaries have been searched for H_2 at various detection levels, notably by Beckwith (1978), Storey (1984), and Isaacman (1984). Table 1.1 lists the reported positive and null or faint detections. The methods used are also listed. It has become very clear that most planetaries show H_2 emission at some level.

Planetary nebulae (PNe) exhibit a wide range of morphologies. The class displaying bipolar symmetry is particularly common, including approximately 50% of all PNe (Zuckerman & Aller 1986). Therefore, understanding bipolar PNe is an important step in learning about PN formation and evolution.

A number of studies have pointed out a strong correlation of detectable molecular emission with PN morphological type. From these studies, it has been made clear that

Table 1.1 Reported H_2 Molecules Detections from PNe

Object	Method	Ref.	Object	Method	Ref.
positive:					
J900	sp.im.	3,19	NGC2346	sp.im.	8,9,24
NGC2440	sp.	1,3	NGC2818	sp.im.	6,8,20
NGC2899	sp.	8	NGC3132	sp.	6,8
Hf 48	sp.	8	NGC4071	sp.	8
NGC5189	sp.	8	IC4406	sp.	6
He2-111	sp.	8	He2-114	sp.	8
Mz 1	sp.	8	NGC6072	sp.	6
Mz 3	sp.	8	NGC6210	sp.	3
M2-9	sp.im.	5,18	NGC6302	sp.	4
NGC6445	sp.	8	NGC6720	sp.im.	2,10, 17,24
NGC6772	sp.im.	8,24	BD+30	sp.im.	2,15
NGC6853	sp.	9	NGC7027	sp.im.	7,14, 15,17,24
M1-78	sp.	3	IC5117	sp.	3
NGC7293	sp.	6	NGC7662	sp.	3
Hb12	sp.im.	2,11,18	AFGL2688	im.	21
AFGL618	im.	13	M1-16	sp.im.	16
NGC6781	im.	12,24	AFGL915	sp.	22
K3-93	im.	23	M1-7	im.	23
M2-53	im.	23	M4-14	im.	23
null or faint:					
NGC246	sp.	6	NGC1360	sp.	6
NGC1535	sp.	6	NGC1535	sp.	6
IC418	sp.	6	IC2149	sp.	3
IC2165	sp.	3	NGC2792	sp.	6
NGC3185	sp.	6	NGC3242	sp.	6
He2-36	sp.	8	He2-37	sp.	8
NGC3699	sp.	8	He2-84	sp.	8
He2-95	sp.	8	Me2-1	sp.	6
He2-161	sp.	8	NGC6153	sp.	6
He2-169	sp.	8	H2-3	sp.	6
Hb5	sp.	8	NGC6572	sp.	2,3
NGC6778	sp.	8	NGC6790	sp.	2
NGC6884	sp.	2	IC4997	sp.	2
NGC7009	sp.	8			

Note: sp.-spectrum; im.-image.

Ref.: 1. Beckwith (1978); 2. Beckwith et al. (1980); 3. Isaacman (1984); 4. Phillips & White (1983); 5. Phillips et al. (1985); 6. Storey (1984); 7. Treffers et al. (1976); 8. Webster et al. (1988); 9. Zuckerman & Gatley (1988); 10. Greenhouse et al. (1988); 11. Dinnerstein et al. (1988); 12. Zuckerman et al. (1990); 13. Latter et al. (1992); 14. Graham et al. (1993); 16. Aspin et al. (1993); 17. Kastner et al. (1994); 18. Hora & Latter (1994); 19. Shupe et al. (1995); 20. Schild (1995); 21. Latter et al. (1993); 22. Thronson (1982), 23. Hora & Latter (1996); 24. Kastner et al. (1994).

butterfly or bipolar morphological type. From these studies, it has been made clear that butterfly or bipolar morphological type appears to have much larger quantities of molecular material. Maybe we can say that if a PN is detected in H_2, it is a young bipolar nebula or a more evolved butterfly nebula.

The reasons that we have undertaken the study to be discussed were manyfold. First, we have looked for systematic differences between the near-IR appearance of PNe to that in the visible or other wavelengths, as well as acquired new, high spatial resolution data on extended H_2 emission. Second, to investigate the asymmetry of structure associated with the slow and/or fast wind and if the bipolar morphology develop gradually as the interacting wind process; Third, because the near-IR transitions of H_2 are excited only in hot gas, or that exposed to intense UV fields, it probes the gas closest to the photo-dissociation region or gas impacted by a shock. A focus of the study was on narrowband line imaging of H_2 and nearby continuum. Finally, it has been suggested that there is a strong correlation of molecular detection (particularly H_2) with PN morphological type and possibly progenitor mass, as well H_2 detection with PPNe. To more fully understand these correlations, attempts were made to make new detections of extended H_2 as well as image objects previously detected.

We will review the physics of diatomic molecules, especially molecular hydrogen in Chapter II. In chapter III, we discuss the excitation mechanisms of molecular hydrogen. Then we describe the data reduction in Chapter IV. The results and discussion will be

present in Chapter V. In Chapter VI, we discuss the relationships between PNe morphology, central star and H_2 emission properties, and also their distribution in the Galaxy. The last chapter gives the conclusions.

Chapter 2 Rotation and Vibration Spectrum of Molecular Hydrogen

(Reference: 1. Herzberg, G. 1950; 2. Penner, S. S. 1959; 3. Struve, W. S. 1989)

In this chapter, we discuss the rotation and vibration spectrum of molecular hydrogen. We will discuss diatomic molecules in general and H_2 as a special case.

The laws of motion for systems of molecular dimensions are the equations of quantum mechanics. The wavefunction for a steady-state system is determined by solving an eigenvalue problem (the Schrödinger equation) for the Hamiltonian operator

$$(H-E_i)\psi_i=0 \tag{1}$$

The dominant terms in the molecular Hamiltonian are the kinetic energy of the nuclei and electrons and the Coulomb interactions among them:

$$H=T_n+T_e+V_{nn}+V_{ne}+V_{ee} \tag{2}$$

$$=-\sum_\alpha \frac{1}{2M_\alpha}\nabla_\alpha^2-\sum_i \frac{1}{2}\nabla_i^2+\sum_{\alpha>\beta} \frac{Z_\alpha Z_\beta}{|R_\alpha-R_\beta|}-\sum_{\alpha,i} \frac{Z_\alpha}{|R_\alpha-r_i|}+\sum_{i>j} \frac{1}{|r_i-r_j|}. \tag{3}$$

Here $\alpha(\beta)$ sum over nuclei with mass M_α, charge Z_α, and position R_α; i(j) sum over electrons with position r_i. We use units such that $\hbar=m_e=e=1$ so that the units of distance are 1 a.u.=0.52918 Å and energy 1 a.u.=27.21 eV. The Shrodinger equation is thus a (3N+3n)-dimensional, second-order partial differential equation which cannot be easily solved.

2.1 Born-Oppenheimer Approximation

One of the most useful simplifying approximations for molecular calculations is the Born-Oppenheimer assumption of separable electronic and nuclear motions. Because the electrons are much lighter than the nuclei, they move much more rapidly so that we may expect them to adiabatically adjust to the instantaneous position of the nuclei. If we do not allow the nuclei to move - i.e. assume infinitely massive - the molecular Hamiltonian reduces to an effective electronic Hamiltonian

$$H_e(r;R)=T_e+V_{nn}+V_{ne}+V_{ee} \tag{4}$$

which depends parametrically on the nuclear coordinates because of V_{nn} (which is a constant) and V_{ne}. We are thus led to write the total wavefuction as a product

$$\psi(r;R)=\psi_e(r;R)\psi_n(R) \tag{5}$$

where ψ_e satisfies

$$[H_e(r;R)-E_e(R)]\psi_e(r;R)=0 \tag{6}$$

or

$$\psi_e[-\sum_\alpha (\frac{1}{2M_\alpha})\nabla_\alpha^2+E_e(R)-E]\psi_n=0 \tag{7}$$

Because $\psi_e \neq 0$, we have also the nuclear Schrodinger equation

$$[H_n - E]\psi_n = [-\sum_\alpha (\frac{1}{2M_\alpha})\nabla_\alpha^2 + E_e(R) - E]\psi_n = 0 \qquad (8)$$

where $E_e(R)$, the electronic energy as a fuction of nuclear coordinates,now plays the role of the potential in which the nuclei move. We write it as V(R) later for vib-rotation.

2.2 Vibration and Rotation

As indicated in the B-O approximation, nuclear motion is governed by a nuclear Hamiltonian

$$H_n = -\sum_\alpha (\frac{1}{2M_\alpha})\nabla_\alpha^2 + V(R). \qquad (9)$$

For a diatomic molecule, the sum over α is then over the two nuclei, and we make the usual change of variables to the center of mass

$$R_{CM} = \frac{\sum_\alpha M_\alpha R_\alpha}{\sum_\alpha M_\alpha}. \qquad (10)$$

and the internuclear coordinate

$$R = R_2 - R_1 \qquad (11)$$

Then the Hamiltonian reduces just as it does in classical mechanics to motion of the center of mass (which is not of interest) plus relative motion of the nuclei. The relative motion can further be separated into motion along R and perpendicular to R, the θ direction Thus

$$H_n = -\frac{1}{2\mu R^2}\frac{\partial}{\partial R}\left(R^2\frac{\partial}{\partial R}\right) + B(R)L^2 + V(R) \qquad (12)$$

where $B(R) = 1/(2\mu R^2)$ is the rotation constant; $\mu = M_1M_2/(M_1+M_2)$.

The first term is the radial momentum, and the second term is the angular momentum L. In this form, we explicitly see that H_n is separable, so that the wavefuctions can be written as

$$\psi \sim \frac{1}{R}\psi_{vib}(R)\psi_{rot}(\theta;\phi) \qquad (13)$$

Substituting this in the nuclear Schrodinger equation, we can separate out a vibrational and a rotational equation

$$\left[-\frac{1}{2\mu}\frac{d^2}{dR^2} + V(R) + E_{rot}(R) - E\right]\psi_{vib}(R) = 0 \qquad (14)$$

and

$$[B(R)L^2 - E_{rot}]\psi_{rot}(\theta;\phi) = 0 \qquad (15)$$

For a diatomic molecule, $\psi(\theta;\phi)$ are spherical harmonics Y_{jm} and the energies are

$$E_{rot}(R)=B(R)J(J+1)=(1/2\mu R^2)J(J+1). \quad (16)$$

For small oscillations it is useful to expand the potential in a Taylor series about R_e, the equilibrium distance

$$V(R)=\frac{1}{2}(\frac{\partial V}{\partial R})^2_{R_e}(R-R_e)^2+\frac{1}{6}(\frac{\partial^3 V}{\partial R^3})_{R_e}(R-R_e)^3+... \quad (17)$$

The Schrödinger equation for the harmonic oscillator can be readily solved if ignore the cubic term and higher oder terms. The energy levels are given by

$$E_{vib}=\omega_e(v+\frac{1}{2}) \quad (18)$$

where $v=0, 1, 2, ...$

The frequency ω_e is related to the force constant k and reduced mass as

$$\omega_e=\hbar\sqrt{k/\mu} \quad (19)$$

Real molecules, of course, are anharmonic oscillators. Another functional form for the vibrational potential which is fairly realistic, and which can be solved analytically, is the Morse function:

$$V=D_e(1-e^{-\beta x})^2 \tag{20}$$

The term D_e is called the spectroscopic dissociation energy and ß is an empirical constant characteristic of the molecule.

Then

$$E_{vib}=\omega_e(v+\frac{1}{2})-\omega_e\chi_e(v+\frac{1}{2})^2 \tag{21}$$

In general

$$E_{vib}=\omega_e(v+\frac{1}{2})-\omega_e\chi_e(v+\frac{1}{2})^2+\omega_e y_e(v+\frac{1}{2})^3+... \tag{22}$$

and the rotational energy:

$$E_{rot}=B_v J(J+1)-D_v J^2(J+1)^2+H_v J^3(J+1)^3+L_v J^4(J+1)^4+M_v J^5(J+1)^5+... \tag{23}$$

the coefficients of eq.(22) and eq.(23) are listed in Table 2.1.

2.2. Dunham Expansion.

Other than B-O approximation method, many methods were developed to calculate the energy levels. e.g.,the Heitler-London method for the hydrogen molecule,the molecular-

orbital method for hydrogen and the method of molecular orbitals. The solutions of the various approximate methods of the Schrodinger problem involving eq.(11) are very fully discussed by Slater (1963). Dunham (1932) used a reduced internuclear distance x defined by

$$x=\frac{(R-R_e)}{R_e} \qquad (24)$$

Table 2.1. Vibration-rotational Constants of H_2^+ (in cm^{-1})

B_0=	59.334611(30)
D_0=	0.04568891(30)
H_0=	$4.8873(100)\times10^{-5}$
L_0=	$-6.100(120)\times10^{-8}$
M_0=	$5.17(30)\times10^{-11}$
(Jennings et al 1984)	
V_{1-0}=	$4161.1782(6.7\times10^{-3})$
B_1=	$56.3722(1.9\times10^{-3})$
D_1=	$-0.04388(1.5\times10^{-4})$
H_1=	$3.97\times10^{-5}(3.1\times10^{-6})$
V_{2-0}=	$8087.000(1.5\times10^{-2})$
B_2=	$53.4823(4\times10^{-3})$
D_2=	$-0.04272(2\times10^{-4})$
H_2=	3.387×10^{-5}
V_{3-0}=	$11782.355(1.7\times10^{-2})$
B_3=	$50.6245(4\times10^{-3})$
D_3=	$-0.04080(1.7\times10^{-4})$
H_3=	3.68×10^{-5}
ω_e=	$4401.217(6\times10^{-2})$
$\omega_e x_e$=	$-121.343(3\times10^{-2})$
$\omega_e y_e$=	$0.8145(0.7\times10^{-2})$
(Fink et al 1965)	

where the Schrödinger equation for a rotating vibrator is given by

$$\frac{d^2\Psi}{dx^2}+\frac{2mR_e^2}{\hbar^2}\left[E-V-\frac{\hbar^2J(J+1)}{2mR_e^2(1+x)^2}\right]\Psi=0 \qquad (25)$$

the last term in the square bracket is obviously due to the certrifugal force of rotation (interaction of rotation and vibration), and is called V_r to distinguish it from V, the potential opposing the internuclear motion. V is expanded in a series around x=0

$$V=hca_0x^2(1+a_1x+a_2x^2+a_3x^3+\ldots) \qquad (26)$$

with

$$a_0=\frac{\bar{\nu}_e^{\,2}}{4B_e}cm^{-1};B_e=\frac{\hbar}{4\pi mR_e^{\,2}c}cm^{-1} \tag{27}$$

The Dunham coefficients for H_2 are listed in Table 2.2.

Table 2.2 Dunham Potential Coefficients of H_2 Molecules

$a_1=-1.6096(2.8\times10^{-3})$
$a_2=1.909(1.1\times10^{-2})$
$a_3=-2.060(3.8\times10^{-2})$
$a_4=1.86(3\times10^{-1})$

Consider first the rotationless state with J=0, Dunham showed that it is possible to solve the resulting Schrodinger equation using WKB method. The vibrational term values are written as the series

$$G_{v,0}=\Sigma Y_{n,0}(v+\frac{1}{2})^n \tag{28}$$

where the first two Dunham coefficients are

$$Y_{00}=\frac{B_e}{8}(3a_2-\frac{7}{4}a_1^{\,2}) \tag{29}$$

$$Y_{10}=\bar{\nu}_e[1+\frac{B_e^{\,2}}{4\bar{\nu}_e^{\,2}}(25a_4-\frac{95}{2}a_1a_3-\frac{67}{4}a_2^{\,2}+\frac{459}{8}a_1^{\,2}a_2-\frac{1155}{64}a_1^{\,4})] \tag{30}$$

the term values for rotating oscillator with J is not zero are given by

$$G_{v,J}=\Sigma Y_{n,j}(v+\frac{1}{2})^{n}J^{j}(J+1)^{j} \tag{31}$$

where the Y_{10} are given by Eq(30) and the term Y_{01} by

$$Y_{01}=B_e[1+\frac{B_e^{2}}{2\overline{\nu}_e^{2}}\{15+14a_1-9a_2+15a_3-23a_1a_2+\frac{21}{2}(a_1^{2}+a_1^{3})\}] \tag{32}$$

2.3. Selection Rules

In the Born-Oppenheimer approximation, the total diatomic wave fuctions in the upper and lower states are

$$|\psi'(r,R)>=|\psi_e'(r,R)>|\psi_{v'}(R)\psi_{J'}(\theta,\phi)> \tag{33}$$

and

$$|\psi''(r,R)>=|\psi_{el}''(r,R)>|\psi_{v''}(R)\psi_{J''}(\theta,\phi)> \tag{34}$$

Since changes in rotational and vibrational as well as electronic state are possible, we must consider both the r- and R- dependence in the total dipole or quadrupole moment operator when calculating transition probabilities,

$$M=M_{el}+M_{nucl} \tag{35}$$

we must then have

$$<\psi'|M|\psi''>=<\psi'_{el}\psi_{v'}|M_{el}+M_{nucl}|\psi''_{el}\psi_{v''}> \tag{36}$$

$$=<\psi'_{el}|\psi''_{el}><\psi_{v'}|M_{nucl}|\psi_{v''}>+<\psi'_{el}\psi_{v'}|M_{el}|\psi''_{el}|\psi_{v''}>\neq 0 \tag{37}$$

These expressions ignore rotation. The term proportional to $<\psi'_{el}|\psi''_{el}>$ vanishes due to orthogonality of the electronic states.

$$\int dR\psi^*_{v'}\psi_{v''}\int dr\psi'^*_{el}(r,R)M_{el}(r,R)\equiv\int dR\psi^*_{v'}(R)\psi_{v''}(R)M_e(R) \tag{38}$$

where $M_e(R)$ is the (R-dependent) electronic transition moment function. If $M_e(R)$ varies slowly over the range of R, we can write

$$<\psi'(r,R)|M|\psi''(r,R)>=\overline{M_e}\int dR\psi^*_{v'}(R)\psi_{v''}(R)=\overline{M_e(R)}<v'|v''> \tag{39}$$

The probability of the electronic transition is then proportional to

$$|<\psi'(r,R)|M|\psi''(r,R)>|^2=|\overline{M_e(R)}|^2|<v'|v''>|^2 \tag{40}$$

Since the vibrational states $|v'>$ and $|v''>$ belong to potential energy functions having different shape, factor $|<v'|v''>|^2$ can assume any value ≤ 1 regardless of v' and v''. So, no selection rules for Δv.

Examination of the total wavefunction for molecular states indicates that it must be either

symmetric or antisymmetric to the exchange of all elementary particles (nuclei and electrons). This exchange is carried out by the inversion symmetry operation, whereby all particles are inverted through the origin into their negative coordinates. If the total wavefunction is given as

$$\psi_{total}=\psi_e\psi_v\psi_r \tag{41}$$

where the subscripts signify the electronic, vibrational, and rotational wavefunctions, we can examine what the effect will be on each individual term of the product. The inversion operation for an electronic wavefunction is equivalent to a rotation of the molecule through 180 degrees about an axis perpendicular to the internuclear axis, followed by a reflection at a plane perpendicular to this rotational axis and passing through the internuclear axis. The first operation leaves ψ_e unaffected, since the electronic coordinates relative to the nuclei are unaltered, whereas the second, which affects only the electrons, changes sign for Σ^- states and is unchanges in sign for Σ^+, e.g. $H_2(^1\Sigma^+)$, where the superscript plus indicates that the electronic wavefunction is symmetric with respect to the reflection operation perpendicular to a plane through the molecular axis. The ground vibrational wavefunctions of linear molecules are also symmetric since the nuclear separations or magnitudes are unchanged in sign on the simple exchange of nuclei. The result in the case of linear molecules is that the symmetry of the total wavefunction on inversion depends on the symmetry of ψ_r. This wavefunction is found to be symmetric (+) or antisymmetric (-) parity respectively, for even or odd J states of a + electronic state, i.e., Σ^+, and the reverse for - electronic states, i.e., Σ^-. Thus, for $<J'|M|J''>$ to

be nonzero in this case of alternating J state symmetries, it must have the form

$$\langle J'(even)|\mu(odd)|J''(odd)\rangle \tag{42}$$

for dipole moment. So the selection rule is: $\Delta J = \pm 1$.

and

$$\langle J'(even)|Q(even)|J''(even)\rangle \quad or \quad \langle J'(odd)|Q(even)|J''(odd)\rangle \tag{43}$$

For quadrupole moment. So the selection rule is: $\Delta J = 0, \pm 2$. S($\Delta J=2$), Q($\Delta J=0$), and O($\Delta J=-2$) branches are observed. Some possible emission lines for H_2 molecules are shown in Fig. 2.1. The emission lines of H_2 molecules detected in planetary nebula are listed in Table 2.3.

Electronic quadrupole transitions are usually referred to as forbidden transitions because of their low intensity and presence only as second-order effects.

2.4. Ortho and Para Modifications

For homonuclear molecules with nonzero nuclear spin the selection rule (antisym.←|→sym.) even though no longer rigorous still holds sufficiently strictly because the transition probability between symmetric and antisymmetric states is extremely small. As a result, gases such as H_2, D_2, N_2, and so forth, may be regarded as mixtures of two

Table 2.3 The observed emission lines of H_2 in PNe

v'--v"	lines
0-0	S(0), S(2), S(3), S(8), S(9),S(12), S(13) S(14), S(15)
1-0	S(0), S(1), S(2), S(3) Q(1), Q(2), Q(3), Q(4), Q(5), Q(6), Q(7)
2-0	S(0) Q(1), Q(2), Q(3), Q(6), Q(7) O(2)
2-1	S(0), S(1), S(2), S(3), S(5)
3-1	S(0), S(1), S(2), S(3), S(4), S(5) Q(3) O(5)
3-2	S(1), S(2), S(3), S(4), S(5)
4-2	S(1), S(3), S(4), S(5) O(3), O(6)
4-3	S(3)
5-3	S(4), S(5), S(6) Q(1), Q(2), Q(4), Q(7)
6-4	S(1) Q(1), Q(3), Q(4) O(2)
7-5	S(3) Q(1), Q(2) O(5)
8-5	S(0) Q(3)
8-6	O(2), O(3), O(5)
9-6	S(1) Q(1)
9-7	S(0) Q(2) O(3), O(4)
11-7	O(3)

Ref. 1. Hora & Latter (1996); 2. Dinerstein et al. (1988); 3. Thronson (1982);Hora & Latter (1994).

Note: We did not list the reference for the several lower transitions. These were in most papers about H_2 moleclues in PNe.

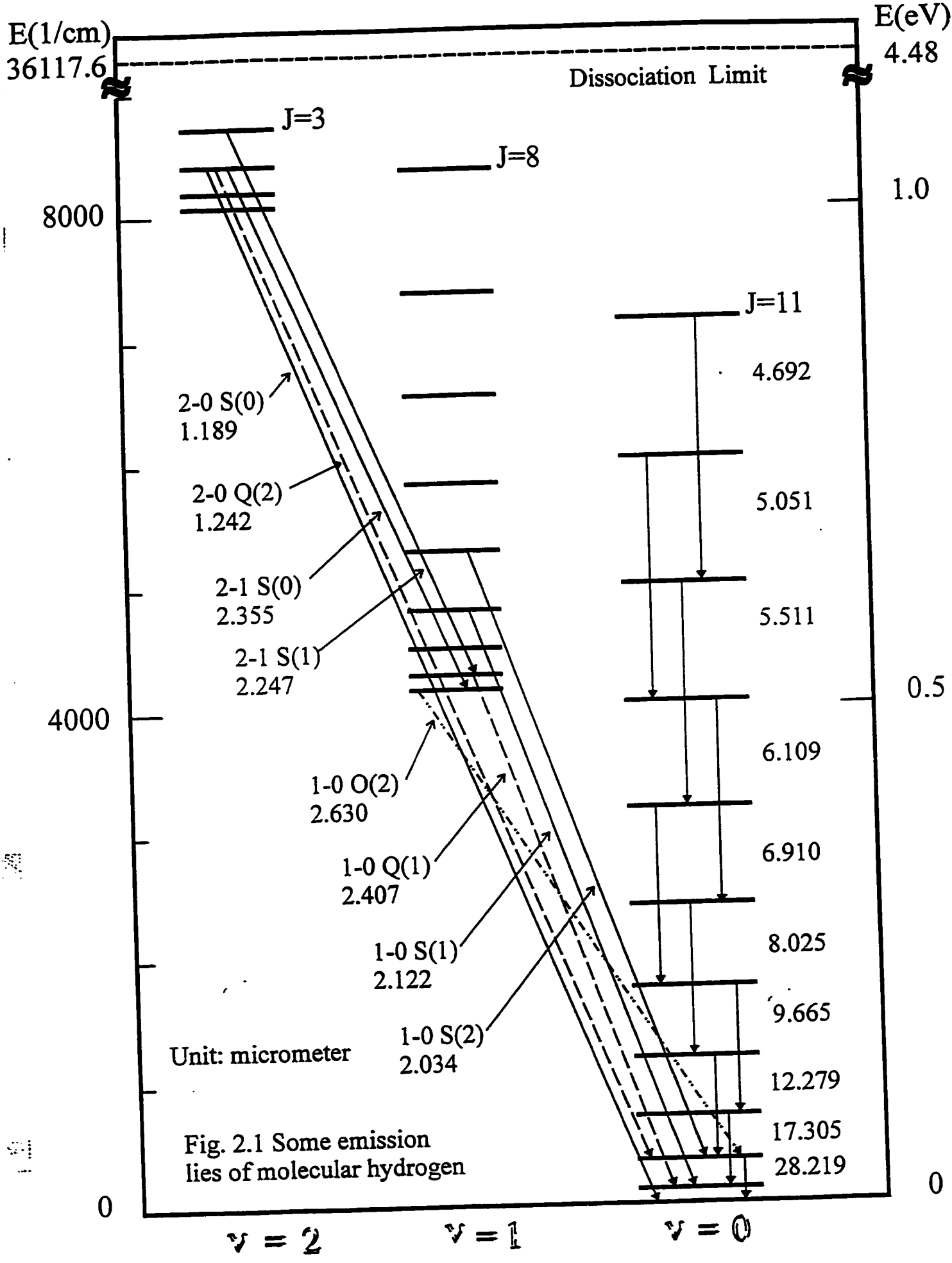

Fig. 2.1 Some emission lies of molecular hydrogen

modifications--a symmetrical with only even-numbered rotational levels and an antisymmetrical with only odd-numbered rotational levels.

Actually, in the case of hydrogen, it is possible to obtain these two modifications separately. When the gas is cooled to a very low temperature, without taking into consideration the rule sym.←|→ antisym., one would expect practically all the molecules to go over to the lowest rotational level, J=0, whereas, considering the selection rule, only those molecules that were originally in the higher even-numbered rotational levels go to the lowest even-numbered, J=0, while all the molecules originally in the higher odd-numbered rotational levels go to the lowest odd-numbered state, J=1. This means that the distribution of rotational levels at the low temperature does not correspond to thermal equilibrium. However, when the gas is kept for a long time at the low temperature, even the molecules that were at first in the state J=1 will eventually go into the state J=0 belonging to the symmetric system; that is, thermal equilibrium should eventually be obtained. If the gas is now allowed to warm up again to normal temperature, the molecules at first can only go from J=0 to the higher even-numbered (symmetric) levels, and not to the odd-numbered (antisymmetric) levels. This means that for some time only the one modification should be present.

The modification with the greater statistical weight is usually called the ortho modification and that with the smaller weight the para modification. We differentiate correspondingly between ortho H_2 and para H_2. The ground state $X^1\Sigma^+_g$ rotational level populations in a

thermal gas gain factors (2I+1)I for even J and (2I+1)(I+1) for odd J. The designations o(ortho) and p(para) are added to the rotational levels

s0(p1x1), a1(o3x3), s2(p1x5), a3(o3x7), s4(p1x9), a5(o3x11), ...

s means symmetric and a means antisymmetric, the statistical weights are written in the parenthesis.

2.5 The Quadrupole Vibration-rotation Transition Probabilities of Molecular Hydrogen

The probability of a spontaneous electric quadrupole transition from an upper level described by quantum number v'J' to a lower level v"J" is given by

$$A(v'J'v''J'')=1.4258x10^{4}(E_{v'J'}-E_{v''J''})^{5}x|<X_{v'J'}|Q(R)|X_{v''J''}>|^{2}f(J'J'')s^{-1} \quad (44)$$

where R is the internuclear distance, $X_{vJ}(R)$ is the nuclear rotation-vibration wave function. $(E_{v'J'}-E_{v''J''})$ is the transition energy. Q(R) is the quadrupole moment, can be defined as

$$Q=R^{2}-2(3z^{2}-r^{2}) \quad (45)$$

where z and r are electronic coordinates in a molecule fixed frame with z axis along the internuclear axis and origin midway between the nuclei.

The branching ratio f(J'J") is given by

$$f(J'J'') = \frac{3(J'+1)(J'+2)}{2(2J'+1)(2J'+3)} \quad for \quad J''=J'+2 \tag{46}$$

$$= \frac{J'(J'+1)}{(2J'-1)(2J'+1)} \quad for \quad J''=J'-2 \tag{47}$$

$$= \frac{3J'(J'-1)}{2(2J'-1)(2J'+1)} \quad for \quad J''=J' \tag{48}$$

The rotation-vibration wave function can be obtained by numerical integration of the radial Schrodinger equation

$$\frac{d^2}{dR^2}X_{v,J}(r) + 2\mu[E_{nuJ} - V(R) - \frac{J(J+1)}{2\mu R^2}]X_{v,J}(R) = 0 \tag{49}$$

where μ is the reduced mass of H_2 measured in units of the electron mass and V(R) is the interaction potential in atomic units of the ground electronic $X^1\Sigma^+_g$ state of the molecule.

2.6. Some Data of H_2.

Table 2.4 gives the line frequencies. We just list the line frequencies for the several lower levels. For unit transfer $1cm^{-1}$ corresponds to 1.2398424×10^{-4} eV. Please note that the dissociation energy for ground state is only 4.48eV but direct photo-dissociation into the continuum requires 14.7eV. In a region where hydrogen is photoionized, the H_2 molecules is rapidly dissociated.

Table 2.4 Emission Line Frequencies

Line	Frequency(cm^{-1})	Reference
0-0 band		
S(0)	354.37355(14)	1
	354.37350(40)	2
S(1)	587.03231(15)	1
	587.03211(17)	2
S(2)	814.42473(8)	2
S(3)	1034.67024(3)	2
S(4)	1246.09811(17)	2
S(5)	1447.27882(41)	2
S(6)	1637.05(5)[a]	2
S(7)	1814.5(1)[a]	2
S(8)	1979.8(4)	3
	1979.7(10)	4
S(9)	2131.1(10)	4
S(10)	2289.9[b]	5
1-0 band		
S(0)	4497.8385	6
S(1)	4712.9088	6
S(2)	4917.0118	6
S(3)	5108.4066	6
Q(1)	4155.2575	6
Q(2)	4143.4668	6
Q(3)	4125.8718	6
O(2)	3802.3	c
O(3)	3571.4	c
2-0 band		
S(0)	8410.4	c
S(1)	8604.2224	6
S(2)	8787.3	c
S(3)	8952.6	c
Q(5)	7917.7	c
Q(4)	7974.5	c
Q(3)	8019.2	c
Q(2)	8051.5	c
2-1 band		
S(0)	4246.3	c
S(1)	4450.4	c
S(2)	4642.5	c
S(3)	4823.9	c

a, b, c: calculated using constants in Table 2.1, b does not calculate error. Ref: 1. Bragg et al. (1982); 2. Jennings & Brault (1983); 3. Beck & Beckwith (1983); 4. Knacke & Young (1981); 5. Jennings et al (1984); 6 Fink et al. (1965)

Table 2.5 Dissociation Energies (cm^{-1}) for H_2 (Kolo & Wolniewicz 1975)

v\J	0	1	2	3	4
0	36117.552	35999.056	35763.150	35411.974	34948.657
1	31955.473	31842.890	31618.775	31285.197	30845.175
2	28028.799	27921.999	27709.417	27393.052	26975.824
3	24332.633	24231.529	24030.306	23730.900	23336.139
10	4962.296	4903.826	4787.763	4615.840	4390.606

Chapter 3 Excitation of Molecular Hydrogen in Planetary Nebulae

3.1 Formation and Destruction

3.1.1 Formation

It is generally accepted that H_2 in planetary nebulae is formed by association on the surfaces of dust grains.

Kahn (1955) drew attention to the possibility that surface reactions might give a possible mechanism for the formation of H_2. Since then surface reaction mechanisms have had an interesting development. McCrea and McNally (1960) discussed the formation of H_2 on grain surfaces. They assumed that a grain could become coated with a mono-molecular layer of hydrogen atoms and that collisions of H atoms from interstellar gas either led to the production of a molecule and its subsequent release into interstellar space, or replenished the atomic hydrogen layer. The nature of surface reactions was investigated in more detail by Gould and Salpeter (1963). They investigated the nature of the interaction between hydrogen atoms and a surface to see if a better estimate of the efficiency of these reactions could be made. Gould and Salpeter also investigated the mobility of H atoms on a surface.

Keeping the atomic-H attached to the grain until a second H-atom sticks has always been

the chief problem for H_2 formation. That is, the thermal evaporation time for atomic-H must be longer than the sticking time, $t_{ev} > t_s$. For a regular surface with no impurities (Watson, 1974)

$$\nu_o^{-1}\exp(D(H)/kT_g) \geq (n_{gas}V_{gas}r_g^2)^{-1} \tag{50}$$

Here T_g is grain temperature, $\nu_o \approx 10^{-12}$s is a characteristic vibration period for the absorbed particle, D is surface binding energy, n_{gas} and V_{gas} are the number density and thermal velocity of the gas, and r_g is the grain radius.

Due to its greater mass and polarizability, molecular hydrogen is normally expected to be bound more tightly by physical adsorption than is atomic-H

$$D(H_2)/k > D(H)/k \tag{51}$$

Formation of H_2 on grains is predicted to occur at a rate per H-atom in the gas,

$$t_g^{-1} = \alpha_g n_0/2\,\mathrm{sec}^{-1} \tag{52}$$

where α_g is the reaction rates for H+H surface reaction $\alpha_g \approx 10^{-16}$ to 10^{-17} cm^3s^{-1} and n_0=total hydrogen($H+2H_2$) density.

3.1.2 Destruction

Not only is vibrationally excited H_2 more reactive than its ground state counterpart but it is vulnerable to destruction by photons with wavelengths $\lambda > 911.7$Å through continuous photo-dissociation and photo-ionization. In shock-heated regions at high temperature, H_2 can also be destroyed by collisional processes. Interest in the dissociation of H_2 in such regions led to the recognition that the collisional process at low densities cannot be characterized by an equilibrium dissociation rate derived from laboratory measurements at high pressures. A large contribution to the equilibrium dissociation rate arises from excitations out of levels close to the dissociation limit, whose populations tend to be highly nonthermal under interstellar conditions. Dove and Mandy (1986) note that H is likely to be more effective in collisionally destroying H_2 than He or other H_2.

3.2 Excitation of H_2

Two mechanism for H_2 excitation are generally considered: radiative excitation in photo-dissociation regions (i.e. excitation by UV absorption and the associated cascade to the ground vibrational state) and collisional (shock) excitation. The relative strengths of upper level lines have been used in the past as a diagnostic of the dominant excitation mechanism in specific regions. However, above a certain gas density ($n_{crit} \sim 10^5$ cm^{-3}), collisional de-excitation of radiatively excited H_2 produces emission that can mimic shock-excited emission. Given a density $n < n_{crit}$, shock-excited emission gives a value of the ratio of the fluxes

$F(V=1\text{-}0S(1))/F(V=2\text{-}1S(1)) \sim 10$

while fluorescent emission gives a value of ~2 (Burton 1992).

For the PNe which have been detected with H_2 lines, the excitation mechanism is collisional (shock) excitation for most of the PNe and radiational excitation for Hb12, M1-16, NGC7027.

3.2.1 Collisional Excitation of H_2.

(Draine et al. 1983)

The distribution of H_2 molecules among their excited vibrational and rotational levels can be used to probe the temperature, density, and intensity of ultraviolet radiation in planetary nebulae. The population distribution is governed by the distribution upon formation, relaxation by slow vibration-rotation transitions, absorption of ultraviolet radiation and subsequent fluorescence, inelastic collisions, and reactive collisions.

As mentioned in 3.1, the details of formation of H_2 on grain surfaces are poorly understood, while the vibration-rotation transition probabilities are well determined as mentioned in Chapter 2, section 7. Vibrational and rotational excitation of H_2 by collisions with H, H_2, He, and electrons has been studied extensively. Cross section and rate data relevant for the temperatures of interstellar molecular shocks ($T \approx 300\text{-}3000K$)

have been summarized by Draine et al (1983).

Inelastic collisions of H_2 molecules with neutral particles remove thermal energy from the neutral fluid at a rate

$$(G_n)_{H_2} = -n(H_2)\Sigma f_i[P_{ic}<E_{ic}>_n + \Sigma_{j\neq i}P_{ij}(E_j - E_i)] \quad (53)$$

where the index i runs over all the rotation-vibration levels of H_2, f_i is the fractional population of level i, and E_i is its energy. The first term in brackets represents dissipation due to collision-induced dissociation from level i at a rate P_{ic} with an average energy loss of $<E_{ic}>_n$ per dissociation. The other terms give the rate at which thermal energy is converted into the internal energy of H_2 and into H_2 quadrupole radiation in terms of P_{ij}, the rate of transitions from level i to level j induced by collisions with neutral particles. The cooling of the electron fluid by inelastic electron-H_2 collisions is given by

$$(G_e)_{H_2} = -n(H_2)\Sigma f_i[Q_{ic}<E_{ic}>_e + \Sigma_{j\neq i}Q_{ij}(E_j - E_i)] \quad (54)$$

in which the neutral impact transition rates have been replaced by rates Q_{ij} for transitions produced by collisions with electrons.

For normal the preshock conditions, the level populations of H_2 attain a steady state on a time scale much shorter than the average time between dissociative collisions. The f_i are therefore the solutions of the equations of statistical equilibrium

$$f_i[\Sigma_{j\neq i}(P_{ij}+Q_{ij}+\Sigma_{j<i}A_{ij}]=\Sigma_{j\neq i}f_j(P_{ij}+Q_{ij})+\Sigma_{j>i}f_jA_{ij} \quad (55)$$

in which the depopulation of bound levels by collision-induced dissociation has been neglected and where A_{ij} is the Einstein A-coefficient for the electric quadrupole transition connecting levels i and j. Because few of the collision rates that appear in the equations have been measured or calculated, people further simplify the problem by writing each level population as the product of independent vibrational and rotational distributions. Using known de-excitation rates of Draine et al. (1983), rates for excitation of H_2 by collisions with electrons, H and He atoms can be calculated.

Since all the probability coefficients will have their values in the local thermal equilibrium (LTE), the excitational rates are given by

$$g_j\gamma_{ji}=g_i\gamma_{ij}\exp(-E_{ji}/kT) \quad (56)$$

where $E_{ji}=E_i-E_j$; with the usual convention that level i lies above level j, E_{ji} is positive; γ_{ji}, γ_{ij} are rate coefficients for excitation and de-excitation respectively; g_i and g_j are statistical weights.

Rates for excitation of H_2 by collisions with electrons, H and He, and H_2 molecules are listed in Table 3.1.

Table 3.1. Rate coefficients for $M+H_2(v_l)\rightarrow M+H_2(v_u)$

M	$v_l \rightarrow v_u$	$\langle \sigma v \rangle$ ($cm^3 s^{-1}$)
e	0→1	$1.8\times10^{-10} T_e^{1/2} (1+x/2)^{-1} e^{-x}$
H	0→1	$5.0\times10^{-12} T_n^{1/2} \exp(-1000/T_n) e^{-x}$
He	0→1	$6.5\times10^{-13} T_n \exp(-95.2/T_n^{1/3}) e^{-x}/(1-e^{-\theta/Tn})$
H_2	0→1	$3.3\times10^{-13} T_n \exp(-80.0/T_n^{1/3}) e^{-x}/(1-e^{-\theta/Tn})$

$x=(E_i-E_j)/kT=6784/T$, $\theta=6784$ K

After corrections for different extinction, observed H_2 quadrupole line intensities can be used to infer ratios of column densities N(v,J) from which an apparent excitation temperature can be obtained

$$\theta(v_2,J_2;v_1,J_1)=\frac{[E(v_2,J_2)-E(v_1,J_1)]}{k}\left[\ln\frac{g(J_2)N(v_1,J_1)}{g(J_1)N(v_2,J_2)}\right]^{-1} \qquad (57)$$

where g(J) is the degeneracy of level (v,J). Such excitation temperatures are independent of the unknown angle between the line of sight and direction of propagation of the shock, and provide a useful diagnostic.

Given the excitation temperature, the mass of shocked molecular gas is easily derived from the nebula's distance and brightness from the Boltzmann distribution:

$$M_{shock}=\frac{4\pi d^2 Q(T_{ex})e^{E/T_{ex}}m_{H_2}I_{\nu}}{g_s(2J+1)h\nu A_{\nu J}} \qquad (58)$$

3.2.2. Radiative Excitation of H_2.

(Black & Dalgarno 1976)

In planetary nebulae, the excitation and abundance of H_2 are closely linked through the absorption of ultraviolet starlight and subsequent fluorescence to the vibrational continuum or to the various bound levels of the ground state. The ultraviolet fluorescent excitation is thought to be responsible for the nonthermal rotational population distributions observed in planetary nebulae and is predicted to maintain measurable populations of vibrationally excited H_2 in planetary nebulae (Black and Dalgarno 1976). Ultraviolet fluorescence to excited vibrational levels will produce infrared line emission in the ensuing cascade of quadrupole vibration-rotation transitions. The fluorescent line emission is characterized by high vibrational excitation temperature that exceed the rotational excitation temperatures, resulting in relatively high fluxes in the lines at wavelengths $\lambda < 2$ μm, which help to distinguish it from thermal emission in shock-heated molecular gas.

The population, $n^*(v',J')$, of a level (v',J') of one of the excited electronic states is governed by

$$\Sigma_{v''}\Sigma_{J''} n(v''J'')R(v''J'',v'J') = n^*(v'J')A^*(v'J') \qquad (59)$$

where n(v"J") refers to the population of a level in the ground state, and $A^*(v'J')$ is the total probability of radiative transitions out of the level (v'J') of the excited state to the bound levels of $X^1\Sigma_g^+$ and to the vibrational continuum. The quantity R(v"J",v'J') is the rate of absorption in a particular line,l, where l stands for all the quantum numbers. Thus

$$R(v''J'',v'J') = \int_0^\infty \sigma_l(\nu)\phi(\nu)d\nu \quad s^{-1} \qquad (60)$$

where the quantity $\phi(\nu)$ is the ultraviolet flux at frequency ν in photons $cm^{-2}s^{-1}Hz^{-1}$ and $\sigma_l(\nu)$ is the photon absorption cross section in cm^2.

Once the populations $n^*(v'J')$ are determined from the equation, the cascade entry rates are easily evaluated

$$\Gamma(v_oJ_o) = \Sigma_{v'}\Sigma_{J'} n^*(v'J')A^*(v'J',v_oJ_o) \qquad (61)$$

where $A^*(v'J',v_oJ_o)$ is the probability of a specific electronic transition.

Every transition in the rotation-vibration cascade gives rise to an infrared photon. In doing the cascade calculation, the equilibrium level populations n(vJ), are computed, so that the infrared line emissitivities

$$\epsilon(v'J',v''J'')=n(v'J')A(v'J',v''J'') \quad photons \quad cm^{-3}s^{-1} \tag{62}$$

follow directly. Calculation of the intensity in a line

$$I(v'J',v''J'')=\frac{1}{4\pi}\int\epsilon(v'J',v''J'')dx \quad photons\ cm^{-3}s^{-1}Sr^{-1} \tag{63}$$

involves an integration over the path through the cloud.

The fluorescent line intensities are of considerable diagnostic value; their interpretation requires accurate transition probabilities for both the ultraviolet and infrared transitions and a means of modelling the depth-dependent abundances and excitation rates for realistic cloud properties.

Chapter 4. Observation and Data Reduction

Observation was made on Oct. 10-14, 1995 at Kitt Peak National Observatory (KPNO) by Dr. Sun Kwok and Dr. Bruce Hrivnak, using the 2.1m telescope, instrument COB, detector INSB 256x256. There are 15 program objects and 3 standard stars. They are listed in Table 4.1 with their position coordinates.

Table 4.1 program objects and standard stars

object	RA(1995)	DEC(1995)
M 4-18	04:25:32	60:06:39
AFGL 618	04:42:38	36:06:16
IC 418	05:27:18	-12:42:05
IC 2149	05:56:06	46:06:10
IC 2165	06:21:32	-12:59:07
Frosty Leo	09:39:40	12:00:01
Hu 2-1	18:49:36	20:50:56
K 3-52	20:03:01	30:32:46
NGC 6881	20:10:43	37:24:24
IC 4997	20:19:57	16:43:11
M 3-35	20:20:54	32:28:54
NGC 7027	21:06:52	42;13:47
21282+5050	21:29:51	51:03:20
IC 5117	21:32:22	44:35:12
Hb 12	23:26:06	58:09:59
HR 1552 *	04:51:00	05:35:45
HR 8143 *	21:17:16	39:23:37
HR 8541 *	22:24:22	44:35:12

* standard stars

4.1. The telescope, instrument and detector

4.1.1. Some Characteristics of Detector

The instrument is called COB. COB has been reconfigured into a high angular resolution instrument. It is known as the Diffraction Limited InfraRed IMager, or DLIRIM.

The detector array is a 256x256 HgCdTe array developed by Rockwell International and designated as a NICMOS 3 device. It reads out in quadrants and is operated in a double correlated sampling (read, reset, read) mode with capability for multiple nondestructive reads.

There are some "bad" pixels on the detector:

a) There are about 250 nonresponsive pixels scattered uniformly across the array, typically singly or in 2x2 clumps.

b) There are about 250 pixels with noisy dark current; i.e., a standard deviation calculated from a series of darks is >2 sigma above the mean for the whole array.

c) There are about 900 pixels with response outside the range mean 25% or equivalently mean 2 sigma.

d) There are about 1000 pixels with noisy response; i.e., a standard deviation calculated

from a series of flatfield exposures which is >2 sigma above the mean for the whole array.

Clearly some pixels fall in more than one category. A bad pixel map can be constructed interactively using IRAF tools and applied during the reductions.How to deal with bad pixels will be discussed later.

Following lists the detector charateristics which is related to the reductions.

Detector bias	1000 mV
System gain	10.46 electrons/ADU
Read noise	35 electrons RMS
Dark current	approximately 2 electrons/sec; this does NOT scale simply with time
Full well capacity	400,000 electrons@1000mv bias
Minimum integration time	382 msec; if using multiple reads to reduce read noise, minimum integration=382 x number of reads.
Unresponsive pixels	about 250, scattered across array
Cosmetics	bad pixels tend to clump in two and fours. Higher dark
current in bottom	20%.

4.1.2. Linearity and Dark Current

HgCdTe detector utilizes a hybrid architecture in which each pixel has an associated unit cell which controls the biasing and readout of that pixel. Thus, each pixel is essentially independent of the others and effects seen in CCDs, such as charge bleeding or trailing from saturated pixels, are not present. However, this independence also means that such properties as linearity and dark current can vary from pixel to pixel, and it is necessary to calibrate these effects for optimum scientific performance. When a pixel is reset, the voltage difference (bias) between the pixel and detector substrate creates a depletion region which acts as a potential well for the collection of (mostly) photo-generated carriers. Electrically, one may consider this potential well as a capacitor. As charge accumulates in the pixel, the depletion region fills in, increasing its capacitance and that of the entire pixel node. Coupled with the steadily decreasing bias on the pixel this yields a sub-linear voltage-charge relationship which quickly rolls off (saturates) when the pixel voltage reaches that of the detector subtrate(zero bias). Technically, a pixel will continue to accumulate charge even into forward bias, but its reponse by that time will be significantly nonlinear.

While one may loosely define a full well of about 400,000 electrons, the response has already fallen by 6% at 350,000 electrons. The read noise and dark current of the array are quite low. However, the dark current has a rather complex character and cannot be simply scaled with time. Necessary dark frames (e.g., for construction of flatfields or dark+bias subtraction of linearity sequences) must be taken separately at each integration time desired. In addition, it is strongly suggested that linearity sequences contain repeated

"check" observations at one integration time to verify the stability of the source. The array quantum efficiency improves by a factor of two from 60K to 77K, so the device was operated at a temperature ~75K, and all tabulated values are referred to this temperature.

4.1.3. Sky Background

There are two predominant sources of infrared sky background, which are essentially independent, both physically and spectrally. At short wavelengths, the sky is dominated by emission lines from OH in the upper atmosphere (typically 90km altitude). The strength of these lines can vary over the course of a night; in addition, upper level winds create inhomogeneity and motion of the airglow. As a result, the intensity of background can vary unpredictably during the night. At longer wavelengths, thermal emission from the telescope optics and optically thick telluric lines predominates. The transition between these two regimes occure at approximately 2.3μm, so the background with filters other than K' or K is primarily OH airglow. The typical sky levels at f/15 are listed below

Filter	ADU/sec
2.12μm	35
2.14μm	42

4.1.4. Signal Levels

Below presents the integrated flux on stars observed on the 2.1-m telescope, averaged over high and low response on the array. These have been converted to the flux for a 10.0 mag star in 1 sec integration time.

Filter	ADU/sec
2.12μm	750
2.14μm	800

4.2. Observation

Because of the high brightness of the infrared sky, often greater than that of the objects under study, and the complex dark current, the technique of subtracting a bias (dark) frame and dividing by a flatfield works poorly in the infrared. Some technique of subtracting the sky prior to flatfielding is necessary. In practice, this is accomplished by several observations of the object field, separated by small motions of the telescope, so that the stars in the field are imaged onto different sets of pixels in each of the images (this is sometimes referred to as "dithering"). If the object density of the field is relatively low, then combining the images using a median algorithm will result in an average from which the astronomical sources have been removed; i.e., a sky frame. This may be done using the IRAF "imcombine" task. If the sky amplitude varies from frame to frame, it may be necessary to scale the frames by their means to obtain a good median average. The resultant sky frame may the be subtracted from each of the raw images to yield sky-

subtracted images which then may be flatfielded and reduced. Note that the detector dark current is also removed in this process. Creating the sky frame from a number of raw images also reduces in increase in statistical noise resulting from arithmetic operations on the images.

Under these considerations, in order to get pure 2.12μm emission line images of PNs, we can subtract the nearby continuum (2.14μm) from the 2.12μm(H_2 line emission + continuum). For each object and each filter, we made a set of 5 observations. These 5 were made such that in the first one the program object was in the center of the upper half of the chip, and then the next 4 object was displaced in a square pattern around the first one about 20" apart. The data we have are: 5 frames which objects are at different position on the images for both filters 2.12μm and 2.14μm; 9 dark frames with exposure time of 60 seconds; and observations of standard bright stars.

4.3. Calibration Data

By "calibration data" we refer both to what is needed to remove the "instrumental signature" as well as what is needed to provide photometric and/or flux calibration. The goal is to not let the quality of the calibration data degrade our signal-to-noise in any way. In this regime the quality of our flat fielding is all important if we want to get the most out of our data.

The following list contains the type of calibration images we need.

a) Over-scan and bias frames: with every exposure there is a pedestal level which is added to the output signal:"the bias", typically several hundred ADUs. As the temperature of the electronics changes during the night this bias level will also change by a few ADUs. Fortunately, current set of CCDs basically have little bias-structure. The detector we used is just~4 ADU in bias level. So we can ignore it. One more reason is that when we subtract the sky frame the bias is subtracted too.

b) Dark Current: All CCDs suffer from thermal "noise" as electrons jitter around in the metallic layers and are occasionally liberated; these nonphoton events are trapped in the potential well. To reduce the size of this dark current the CCDs are cooled approximately -100°C with the result that dark current on our chips is barely detectable(3-4 e/hr/pixel). The dark current is usually quite uniform and hence has no effect on photometry if the sky value is being determined from the program frames themselves. One might still wish to take several dark frames to substantiate that the effect is small. In practice, light-leaks can exceed the level of the dark current level, so care should be done to do this with the dome darkened. The exposure time on our dark frames should equal or exceed our longest exposure time, and if there is any possibility that we may actually need to use dark frames to correct our data, we should take a minimum of 3 of these to allow cosmic-rays and radiation-events to be filtered out in determining the average. These long exposures are taken with the shutter closed. In our case, the longest exposure time is 60

seconds, we have 9 dark frames. These should be enough.

c) Flat-field: Each pixel in the CCD responds to light a little differently. In practice there are slight wavelength-dependent gain differences between each pixel that must be removed. To remove this pixel-to-pixel gain variation one needs a series of well-exposed "flat", obtained through each filter. The total exposure in one's flats should be such that one never degrades the signal-to-noise in one's program frames; in practice, accumulating 4 or 5 flats with 20,000 e/pixel will amply suffice to remove the pixel-to-pixel variations. However, even if the telescope were being illuminated completely uniformly the CCD is unlikely to be illuminated uniformly. Instead, vignetting due to guider mirrors, non-uniformities in the filters (and dust on the filters) require that large-scale flat-fielding is necessary. Usually dome flats or projector flats (exposures of a quartz lamp illuminating the spectrograph slit) will suffice to remove the pixel-to-pixel variations. We will want to expose that dome or projector flats so that we get sufficient counts to not degrade the signal-to-noise of the final images. If we are after 1% photometry per pixel then we will need to have several times more than 10,000 electrons accumulated in our flats, but we need to be careful not to exceed the good linearity limit in any single flat exposure. Generally if we have 5 or more flats each with 10,000 electrons per pixel we are probably fine. We will need a set like this for every filter or every grating tilt, and we probably will want to do a new sequence every day. If our program frames are relatively sparse and contain sky levels at least 100 e above bias, we can probably use these frames themselves as the ultimate correction for large scale illumination errors. We will have to

combine them with scaling by the mode and experiment with the various rejection algorithms to remove all our interesting stuff and leave only sky (Using the task COMBINE in IRAF). Alternatively, we can obtain 4-5 exposures (the more the better) of relatively "blank sky" fields, offsetting the telescope by 30 arcsec or more between each exposure. When done we will be able to "clip" out the stars and smooth the result. Still, we will want at least 100 e per pixel above sky if we want to use these to correct to a small fraction of the night sky. For 2.1-m telescope at KPNO, dome flats agree with dark-sky flats.

d). Dealing with Cosmic Rays: If we were to take a 15-minute "dark" exposure you would be struck by the large number of 1-2 pixel radiation events present. Fortunately, most of these are of modest amplitude and would be lost in the sky-noise for broad-band work. However, some would not. These "radiation events" are often dubbed " cosmic rays events", although in fact many of them originate in the CCD substrate itself. We will see later that, in our case, most of the cosmic rays are always in the same position at the chips. So when we subtract the sky-dark frames, the cosmic rays are also removed.

e). Flux calibration: The system sensitivity with the two different filters, 2.12μm and 2.14μm, is different. In order to calibrate the effect, we observed several bright stars at these wavelengths. From the known values of spectral intensity and the observed ones, we can find the ratio of system efficiency.

4.4 Data Reduction Procedure

All our data are reduced using the software IRAF. IRAF is a general Image Reduction and Analysis Facility providing a wide range of image processing tools for the user. IRAF is a product of the National Optical Astronomy Observatories (NOAO) and was developed for the astronomical community.

a). To get the sky frame for each filter, we use task IMCOMBINE to combine the 5 images in each filter to get the average, with the reject set to reject the bright pixels (avsigclip) that objects will contribute. Since the objects move around on the 5 frames, they can be easily rejected leaving only a frame with sky in it.

b). The resulting average sky frame in each filter can be subtracted from the 5 images of the program object. This is done separately for each object. This leaves 5 sky-subtracted images for each object in each filter. In this process, the dark current is also removed.

c). To get the flat field to correct for pixel-to-pixel sensitivity, we use the longest average sky frames that we have for which we also have dark observations. We subtract the corresponding average darks from the combined sky frames of the same exposure times. If there were several objects which were observed at this exposure time then there are several average skies at each filter to use. We then produce an average flat field in each

filter by combining the dark-subtracted average sky images.

d). The resulting flat fields are divided into the sky-subtracted objects images to correct the variations in pixel sensitivity.

e). To get the combined images, 4 of the images need to be shifted to match the position of the one which is on the middle of image. We find the center by using the tasks DAOPHOT and IMEXAMINE. For NGC7027, we used the small star by the side of the object to find shift parameters.

f). Observation include the filters 2.12μm and 2.14μm. Since the longest dark that we have is 60 seconds, then the flat field for each of the 2 filters should be based on the average skies obtained with 60s exposures. We have 4 objects which have same exposure times.

g). Since we are looking at differential measures on and off H_2 to investigate H_2 emission, we did not do the extinction. The standard stars were used to get calibration parameter for filters efficiency and corrected the ration flux(2.12)/flux(2.14) values by this calibration parameter before we subtract the continuum.

4.5. The Calibration Parameter

There are two methods to find the calibration parameter

a). Using the standard stars

Supposing that the flux of the standard star at 2.12μm and 2.14μm are same, we can measure the flux of the standard star in our image at these two wavelengths. The ratio flux(2.12μm)/flux(2.14μm) is the calibration parameter. This can be done using the task "imexamine" or "phot". We find the magnitude or total flux at these two wavelengths or say filters to obtain the calibration parameter. Table 4.2 lists the standard stars magnitude and flux as well as the calibration parameter.

Table 4.2. Derivation of Filters Efficiency Using the Standard Stars

standard star	filter	mag.	flux	ratio
HR8143	2.12μm	11.010	394763	
	2.14μm	10.440	666032	0.59
HR1552	2.12μm	11.302	301379	
	2.14μm	10.772	491594	0.61
HR8541	2.12μm	11.302	302028	
	2.14μm	10.712	518389	0.58
HR1552	2.12μm	11.170	341086	
	2.14μm	10.592	579278	0.59
average				0.59

b). Using the star appears in the program object field

This happens in NGC7027. A small nearby star appears in the same image with NGC7027. Supposing the flux at 2.12μm and 2.14μm are same for the small star, we find the magnitude or flux then get the ratio, which is the calibration parameter. Using different task parameter, we get different values. But they are very close. The result is listed in Table 4.3.

Table 4.3 Derivation of Filters Efficiency Using the Nearby Star

aperture radii	width of sky annulus	filter	mag.	ratio
5	3	2.12μm	15.070	
		2.14μm	14.442	0.564
	4	2.12μm	15.042	
		2.14μm	14.398	0.553
6	3	2.12μm	14.942	
		2.14μm	14.302	0.555
	4	2.12μm	14.934	
		2.14μm	14.276	0.546
average				0.555

Also, we can use the profile of the line through the same point. Because this point is easy to be found only at the center, we get only one parameter with this method. The peak values are 330 and 580 respectively. So we get the ratio=330/580=0.57

At last, we get three values using three different methods. We choose the average to be the last calibration parameter which is 0.57.

Chapter 5 Results and Discussion

5.1 Results

Table. 5.1 lists the radius of the photometry, flux and FWHM (Full Width of Half-Maximum). The flux within the circular aperture is computed by simply summing the values with centers within the specified radius of the center position. In order to get flux, we use the standard star HR8541 which its flux at 2.12μm is 14Jy (Evens et al.1987). At 2.14μm, we suppose the same value. Even though the two different filters' sensitivities are different, the direct comparing with the flux of standard star gives the physical flux values.

The FWHM is the result of Gaussian fitting. The unit is pixel number, 1 pixel=0.2". All these can be done using the task "imexamine" in IRAF.

From the table, we found that all the 15 PNe except IC2165 have 2.12μm emission after subtracted the continuum. However, because the contamination from HeI, we can not say that they all have 2.12μm line emission of H_2 molecules. These will be discussed individually.

5.2 Individual

NGC 7027

Molecular hydrogen was first detected by Treffers et al. (1976) in NGC7027. Three lines of the 1-0 quadrupole spectrum of molecular hydrogen were detected. They are 1-0S(1), Q(3), Q(1). This was the first identification of molecular hydrogen in a planetary nebula.

High spatial resolution images at 2.12μm were presented by Graham et al.(1993).

Table 5.1 Flux and FWHM of the PNe

object	filter	radius	flux(Jy)	FWHM
NGC7027	l+c	145.23	2.446	49.95
	c	146.07	1.606	48.75
	l	144.75	0.897	56.85
K3-52	l+c	26.43	1.112E-2	8.87
	c	22.01	7.039E-3	7.34
	l	24.06	3.328E-3	6.98
M3-35	l+c	27.87	6.533E-2	9.29
	c	27.90	5.902E-2	9.30
	l	23.64	7.992E-3	7.71
NGC6881	l+c	37.77	3.655E-2	12.69
	c	36.96	2.321E-2	12.34
	l	41.87	1.639E-2	13.84
IC4997	l+c	18.06	9.367E-2	6.02
	c	18.43	8.246E-2	6.14
	l	15.05	1.382E-2	5.02
21282	l+c	23.23	1.107	7.74
	c	21.59	0.104	7.21
	l	10.75	8.050E-2	7.60
Hb12	l+c	20.15	0.183	6.71
	c	20.90	0.161	6.97
	l	18.47	2.795E-2	6.16
IC418	l+c	16.61	6.540E-2	5.53
	c	18.22	5.312E-2	6.07
	l	13.36	9.140E-3	4.46
IC2165	l+c	100.18	4.681E-2	32.17
	c	97.48	4.332E-2	33.07
	l	2.18	3.303E-5	4.40
IC5117	l+c	27.75	0.123	9.25
	c	27.81	0.101	9.27
	l	17.89	1.993E-2	6.08
M4-18	l+c	17.04	4.431E-2	5.66
	c	23.09	4.641E-2	7.70
	l	10.05	2.392E-3	3.51
AFGL618	l+c	19.08	0.285	6.48
	c	17.22	0.184	5.76
	l	40.32	0.159	16.43
IC2149	l+c	14.65	3.932E-2	4.90
	l	13.57	3.582E-2	4.52
	c	10.99	2.800E-3	5.16
Frosty	l+c	30.39	1.013	10.15
	c	28.62	0.930	9.54
	l	55.13	0.305	20.39
Hu2-1	l+c	23.17	4.431E-2	7.72
	c	23.40	3.944E-2	7.80
	l	13.76	5.836E-3	4.64

The H_2 1-0S(1) emission is composed of two components: (1) an incomplete elliptical ring of knots which bounds the ionized gas; (2) a remarkable thin shell which loops around the HII region with fourfold symmetry. The morphology of NGC7027 can be described as a photodissociation region which separates the ionized and molecular gas. They suggest that the exterior H_2 loops are due to molecular gas heated by the far-UV emission escaping from the HII region. From the location of H_2 emission, they suggest that the excitation mechanism is UV radiation excitation.

This suggestion was also presented by Cox et al (1997). Using an instrument called BEAR, they mapped the H_2 velocity distribution. It demonstrates that the kinematics of the hot gas traced by H_2 is firmly linked to the outer molecular envelope. The H_2 emission in NGC7027 is consistent with excitation in the UV photon dominated region (PDR) at the interface of the ionized and molecular gas. They also revealed new morphological details. The H_2 emission is distributed at the periphery of the ionized gas, along a four-lobed clover pattern with an equatorial torus which is seen for the first time in its entirety. They do not confirm the presence of a second inner H_2 loop bounding the ionized gas as found by Graham et al (1993). They argued that it was a result of inadequate subtraction of the continuum and, to a lesser extent, to contamination by the nearby HeI 4^3S-3^3P^0 line at 4733.4 cm^{-1}.

Our 2.12μm image is very closed to that of Graham et al. (1993). An broken elliptical ring of knots which bounds the ionized gas is seen. The second shell loops the HII region with fourfold symmetry. This fourfold loop has a major axis of about 18" at N degree to W and minor axis 14". The inner ring is elongated in NW-SE direction with major axis 10" and minor axis 8". The two peaks are located at the shoulder of the inner ring and separated by about 6". Note that the two major axises have an angle about 25 degrees. Beyond the outer shell, there is very faint emission.

Frosty Leo (IRAS 09371+1212)

Forveille et al (1987) identified this as an evolved star with substantial CO outflow, and suggested icy grains as the source of its unusual infrared emission. This was confirmed by Hodapp et al. (1988) and Rouan et al. (1988).So the nebula was nicknamed "Frosty Leo".

Roddier et al (1995) presented near-infrared, 0.1" resolution images of this bipolar nebulae and suggested a binary star formation mechanism for the nebula from their images.In their image the west star is round, the east star image is elongated in the direction of the west star. It also has an arm extending toward the north and a hint of another one extending toward the southeast. It seems same in our images.

Langill et al. (1994) discussed the possibility that the Frosty Leo nebula is not a post-AGB star but a pre-main-sequence object formed in isolation from interstellar clouds.

Our result shows that this young nebula has strong H_2 emission. The strongest inner elliptical part is elongated in the N-S direction with major axis 6" and minor axis 5". The outer faint elliptical part is elongated in NW-SE direction with major axis 14" and minor axis 12". In the center there are two peaks separated 1.4" at SE-NW direction. Note the two major axes have an angle about 45 degree. Because emission is extensive, the excitation mechanism is shock excitation.

AFGL618

AFGL618 is one of the best-known proto-planetary nebulae. It was the subject of an extensive infrared and visual study by Westbrook et al (1975), who first suggested the evolutionary stage of the object on the basis of its emission spectrum and geometry. This object is a bipolar nebula. The bipolar structures of roughly 2"-3" diameter are separated by ~7" in the east-west direction (Calvet & Cohen, 1978). Centimeter-wavelength radio

observations reveal an elongated compact source aligned with the bipolar lobes (Kwok & Bignell 1984). Latter et al. (1992) suggested that the bipolar axis is inclined to the plane of the sky by i~45°.

Beckwith et al. (1984) detected the 1-0S(1) line at 2.12μm. This is indicative of expanding, shocked material and, along with the visual emission lines, suggests an energetic, active source. H_2 is associated with the front (east) lobes, indicating that it is produced in the shocked region.

Observations at 10.0, 11.2, 13.2 and 20.2 μm (Hora et al 1995) demonstrates the source was extremely compact at all wavelengths. Comparision with observations of a point source showed evidence for extension in the E-W direction on the order of 0."1-0."2. The object is not as extended in the N-S direction, with the source size$<$0."05 at 10.0,11.2 and 13.2 μm, and $<$0."1 at 20.2μm.

Latter et al. (1995) argued that the excitation is due to both shock exciation and PDR.

This object has strong 2.12μm emission. We can describe this object as a peanut with two peas. They are located in east and west. The two peaks at the center of the peas which separated about 4.4". The whole scale is about 12" and the bridge which connects the two peas has a scale about 2". From 2.12μm and 2.14μm images, we can see that the 2.14μm continuum emission is associated with the east lobe. This indicates that the central star is associated with the east lobe suggesting the axis of bipolar is inclined to the plane of sky by a significant angle.

Hu2-1

On the basis of the VLA images, Kwok & Aaquist (1993) suggest a double-shell structure for Hu2-1 consisting of an outer butterfly-like shell and an inner ring-like shell.

Long-slit spectra of high spectral and spatial resolution of the nebula show that the main structure of Hu2-1 is a bipolar shell consisting of a compact (radius $\approx$0."9), slowly expanding ($\approx$15 km/s) bright equatorial and two faint bipolar lobes expanding at 30km/s (Miranda 1995). Three compact condensations have been detected in the nebula. Two of them form a pair of highly collimated, high velocity bipolar condensations separated by $\approx$6" on the sky. They move at higher velocity and present a higher collimation than the bipolar lobes. The bipolar condensations present noticeable differences in velocity, velocity dispersion, collimation angle and distance from the central star. The third compact condensation is not related to the main nebular axis. The deduced ionized nebular mass($<10^{-2}M_{\odot}$) and kinematical age (~660yr) of these components indicate that Hu2-1 is a very young planetary nebula. All these structures are surrounded by a faint spherical halo (radius~12"). The formation of Hu2-1 could be explained assuming that the central star is a mass exchanging binary.

Our 2.12μm image shows that this object has a typical butterfly morphology with two lobes elongated 2.6" in the SE-NW direction and 2.0" at NE-SW direction. The inner ionized region has a diameter of about 0.5". The inner part of the shell is stronger than that of the outer part. It is difficult to figure out whether this nebula has a double shell. From the distribution of 2.12μm, the excitation of H_2 maybe due to UV fluorescence.

Hb12

Radio continuum images have shown Hb12 to be a bipolar nebula, aligned roughly north-south (Bignell 1983). Miranda & Solf (1989) obtained long-slit spectroscopy and confirmed the bipolar nature of the source. Their observation showed that the north lobe is receding while the south lobe is approaching. Dinerstein et al. (1988) mapped the central region and found the 2.122 μm emission to be distributed in a "doughnut-like" shell with inner and outer dimensions 4" and 8". Near-IR images and spectra of Hb12 (Hora & Latter 1994) reveal its large-scale bipolar morphology. The images suggest a toroidal or cylindrical structure, which delineates an equatorial density enhancement that

is channeling the bipolar flow.

Shocks are common in PNs, and in most PNs observed to date in which H_2 emission has been detected it appears to be purely shock-excited or has a significant shock-excited contribution. However, Hb12 represents one of the clearest cases known of fluorescent molecular hydrogen emission, first determined by Dinerstein et al.(1988) and confirmed by Ramsay et al. (1993) and Hora & Latter (1994).

In our 2.12μm image this nebula appears two butterflies morphology. For the outer part, the big butterfly, the two lobes are elongated about 4.4" almost in the E-W direction with weak emission, while for the inner part, the small butterfly, the two lobes are elongated 3" in the N-S direction with strong emission. The south part is stronger than the north one.

NGC6881

This object has optical diameter 5" (Jacoby & Kaler 1989). 8.4Ghz observations (Kwok & Aaquist 1990) suggested a butterfly morphology and were confirmed by the optical structure (Hua et al. 1993). The Hα image displays a central roundish core (2.5") surrounded by an elongated (SE-NW) diffuse shell (7") while [NII] image shows a "crab" structure with opposite (SE-NW) extension up to 6" from the nucleus.

Our 2.12μm images reveal a butterfly morphology. It is consistent with the result of Kwok & Aaquist (1990). The two lobes lie in the SE-NW direction with an elongation of about 3.4". The width in the SW-NE direction is 4". The ionized region has a diameter of 2". The morphology can also be described as an elliptical shell with four emission loops at four corners. The strong emission lies the elliptical shell which is overlapping part of the two lobes. The extensive emission distribution suggests that the excitation mechanism is shock excitation.

IC4997

Tamura et al. (1990) show a radio continuum map at 1667 MHz in which IC4997 appears elongated at position angle (PA) $\approx 54^{\circ}$, suggesting nonspherical mass motions. The 3.6 cm radio continuum map (Miranda 1996) shows that IC4997 is a double shell planetary nebula consisting of a faint, knotty outer shell of size 2.7'x1.4", elongated at position angle about 54°, and a bright, circular inner shell of 0.28' in diameter. The outer shell presents an hourglass-like morphology and exhibits a striking mirror symmetry with respect to its minor axis.

The 2.12μm morphology is very closed to that of AFGL618. It is elongated about 1.7" in the E-W direction and 1.3" at N-S direction suggesting a bipolar or butterfly morphology. Because the emission is close to the central star, if these emission is due to H_2 emission, the excitation mechanism may be fluorescence. However, short of the ratio of two H_2 rotation-vibration lines make the diagnostic difficult.

IRAS 21282+5050

This is an unusual planetary nebula discovered by IRAS (Infrared Astronomical Satellite). It is a young PN (Cohen 1987). The VLA images at wavelengths of 2 and 6 cm show that the ionized region is a shell or torus with an extent of about 3"x4". The major axis is oriented roughly north-south. High resolution CO J=1-0 interferometer maps by Shibata et al. (1989) show a clumpy expanding shell elongated N-S. Meixer et al. (1993) found that the structure is remarkably similar across the infrared spectrum. The 3.3, 8.5, 10, 11.3 and 12.5μm narrow band images of the object reveal a 4.5"x6" nebula with two prominent peaks aligned almost E-W and separated by 1.7'-2.1'. The star as seen at K band is situated between the peaks. They interpreted the observed structure to be an expanding torus with its polar axis aligned E-W and lying in the plane of the sky. High resolution optical images by Kwok et al. (1993) clearly show it to be extended and elongated along the N-S direction, with a size of 6.5"x4.8".

Our 2.12μm image shows that it has faint 2.12μm emission only in the inner part. A bipolar morphology is presented. Two lobes are elongated in the SE-NW direction. From its location, we can know this may be due to HeI emission.

M3-35

From our images, this nebula has a round morphology. The 2.12μm emission maybe from HeI because the location is very close to the ionization region.

IC2165

Continuum map at 3.6 cm exhibit an elliptical morphology (Miranda 1995), with the major axis at position angle (PA)=105. It presents two maxima along the minor axis (PA=15), separated by ~0.5'.

Our results show that this object has an elliptical outer and rectangular inner parts. The outer part is elongated 4" in the SW-NE direction and 3.2" in the SE-NW direction with weak emission. The inner irregular rectangular has a strong emission which extends 1.4" at S-N direction. Because the extreme faint 2.12μm line emission, we can know that this object has very faint HeI emission at 2.12μm.

IC2149

IC2149 is a small (optical diameter 8.5") PN. The planetary nebula exhibits a more or less homogeneous circular Hα image (Hua et al.) while the [NII] map display four symmetrical condensations well separated in two lobes. Although the asymmetric optical image of IC2149 does not fall into any standard morphology (Balick et al. 1993), the overall shape and its radio frequency image show a bilateral symmetry (Feibelman et al. 1994).

This object has very faint 2.12μm emission.

IC418

IC418 is a young, low-excitation, elliptical shaped nebula with two axis symmetry (Balick 1987 and Louise et al. 1987). The IR emission from IC418 shows several distinct components. NIR spectrophotometry reveals a substantial excess (Willner et al. 1979) and there is evidence that components of emission lie exterior to main HII shell (Willner 1979, Philips 1984). An extended halo is seen in the K and H images which extends approximately 13" farther than the peaks of the main lobes, for a total nebular diameter of 36" along the minor axis and 40" along the major axis of the nebula (Hura et al. 1993).

Our result is very close to that of Hura et al. (1993). However, we have some difficulty to figure out the 2.12μm line emission due to H_2 or HeI.

K3-52

This nebula has relative strong 2.12μm emission. However, we can not figure out whether due to H_2 emission because of its small size.

M4-18

Very faint 2.12μm emission.

5.3 Discussion

5.3.1 Contamination

It is important to note that there can be a contribution from HeI 3^3P^0-4^3S at λ=2.114μm

in the H_2 narrowband images because the resolution of the filters can not separate them (Fig. 5.2). Such a contribution can sometime be determined from the location of the emission. In general, within ionized region the 2.12μm image traces a blend of H_2 and HeI, but only H_2 beyond the edge of the ionized gas. In fact, any contribution from HeI 2.114μm line should largely trace the Brackett-γ emission. Unfortunately, we didn't take the Brackett-γ images. Since the main aim of this program is to study the morphology of PNe, any information, from H_2 line emission, or HeI line emission, or both of them is useful for us to find the morphology. But we should be careful when we discuss the distribution of H_2 in planetary nebulae. From eq.(59), we can derive the shocked molecular hydrogen mass. however, because of the contamination of HeI and short of the two wavelengths intensities, we can't derive the total H_2 molecules mass.

5.3.2 Distribution of Molecular Hydrogen in PN

In general, the appearance of the H_2 maps resembles the brighter features of the optical photographs very closely. It has been established by the work of Beckwith et al. (1978) and Storey (1984) that the excited molecular hydrogen zones lies further from the center than the ionized hydrogen zone and very close to the transition region of the nebula. Further investigation shows that weaker H_2 emission can also be detected well inside the ionized area. However, because of contamination by HeI 2.114μm, it is difficult for us to figure out the distribution of H_2 molecules in our program objects. But we did use the idea that HeI line emission lies within the ionization region to figure out whether the PN has molecular hydrogen line emission.

IRIM NARROWBAND FILTERS

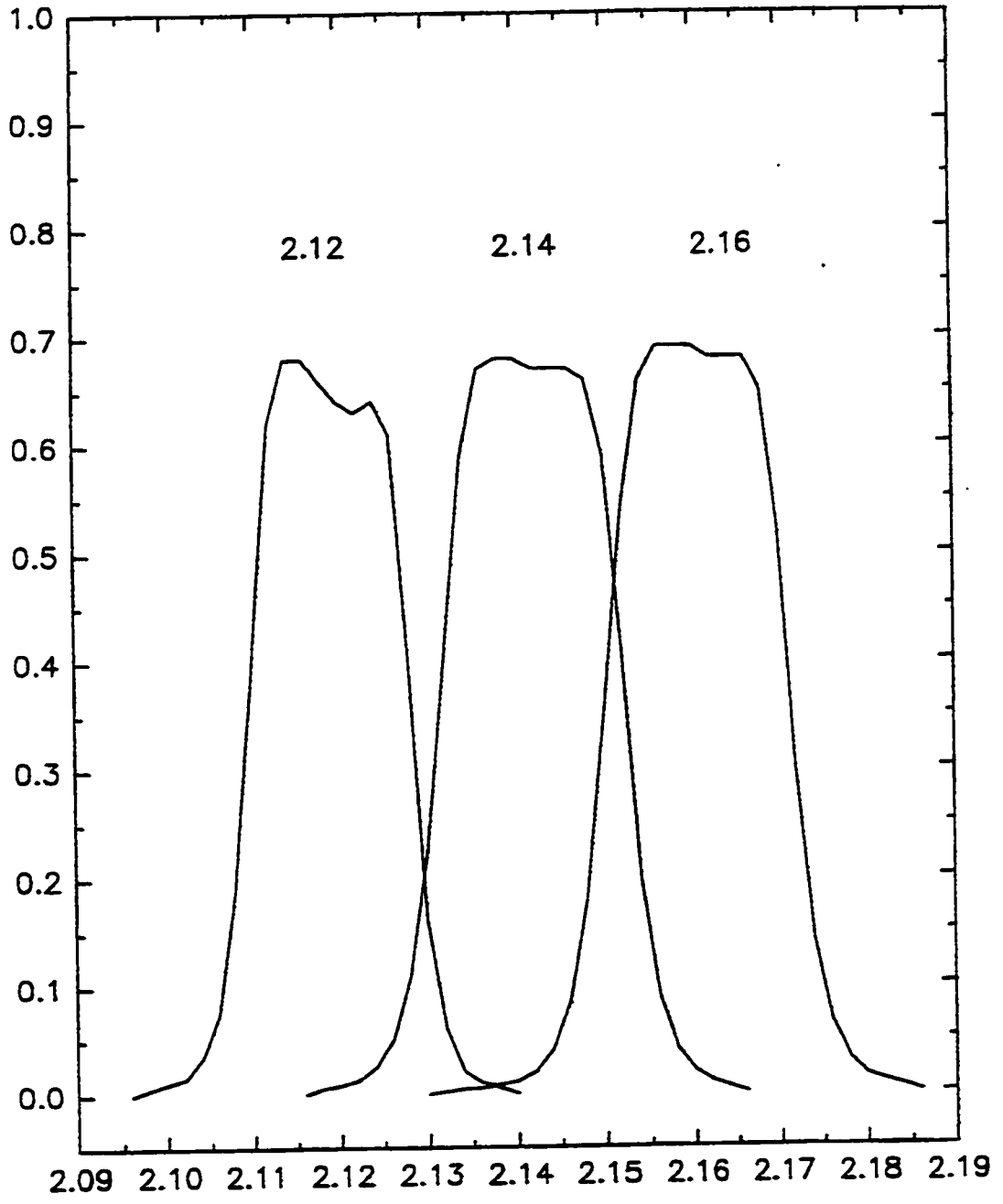

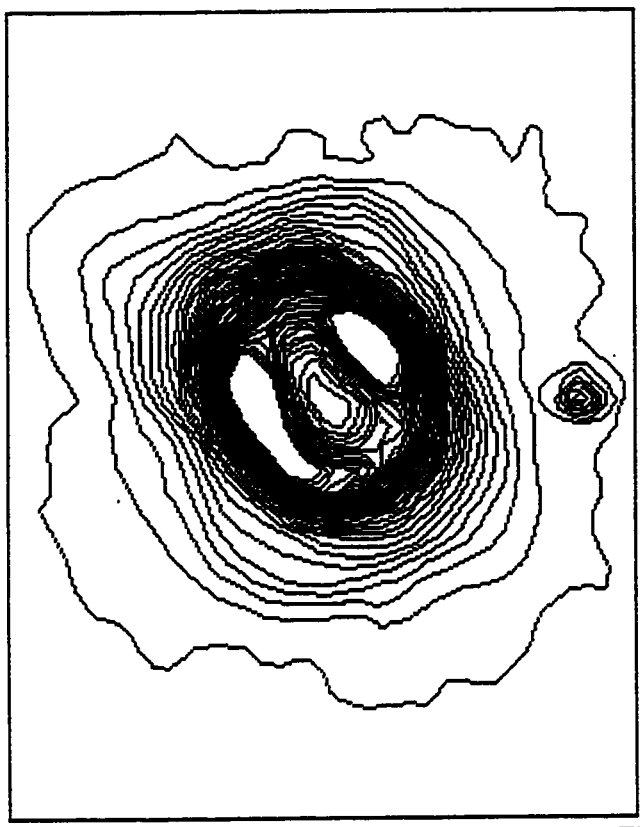

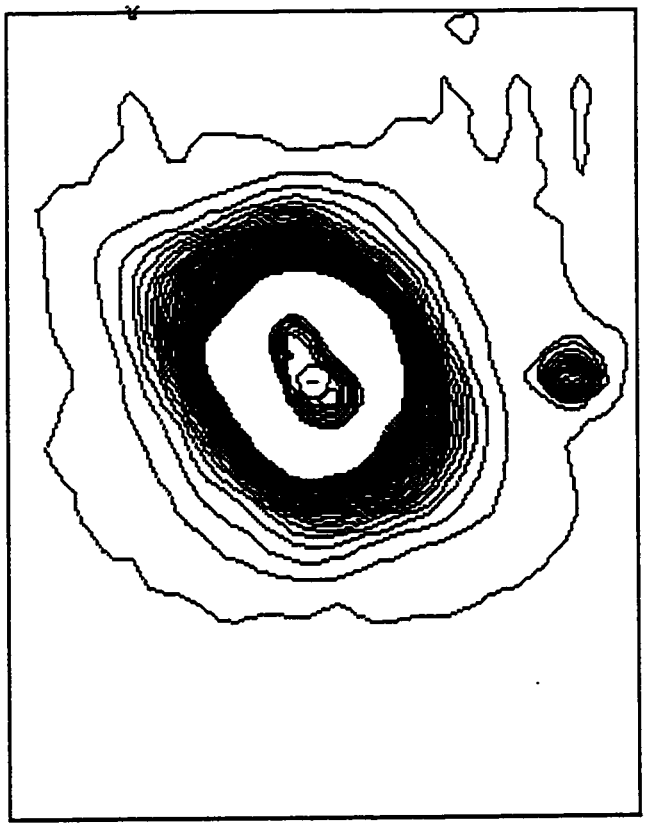

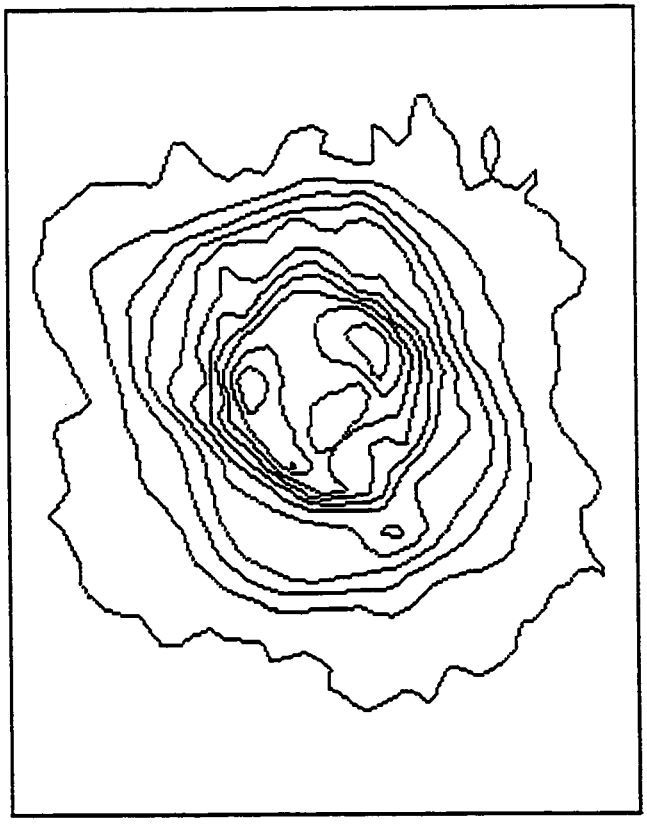

Fig. 5.1 NGC7027

Topleft: line+continuum
topright: continuum
left: line
All contour maps are block averages by 5 in x and 5 in y. Interval is 25 (pixel value)

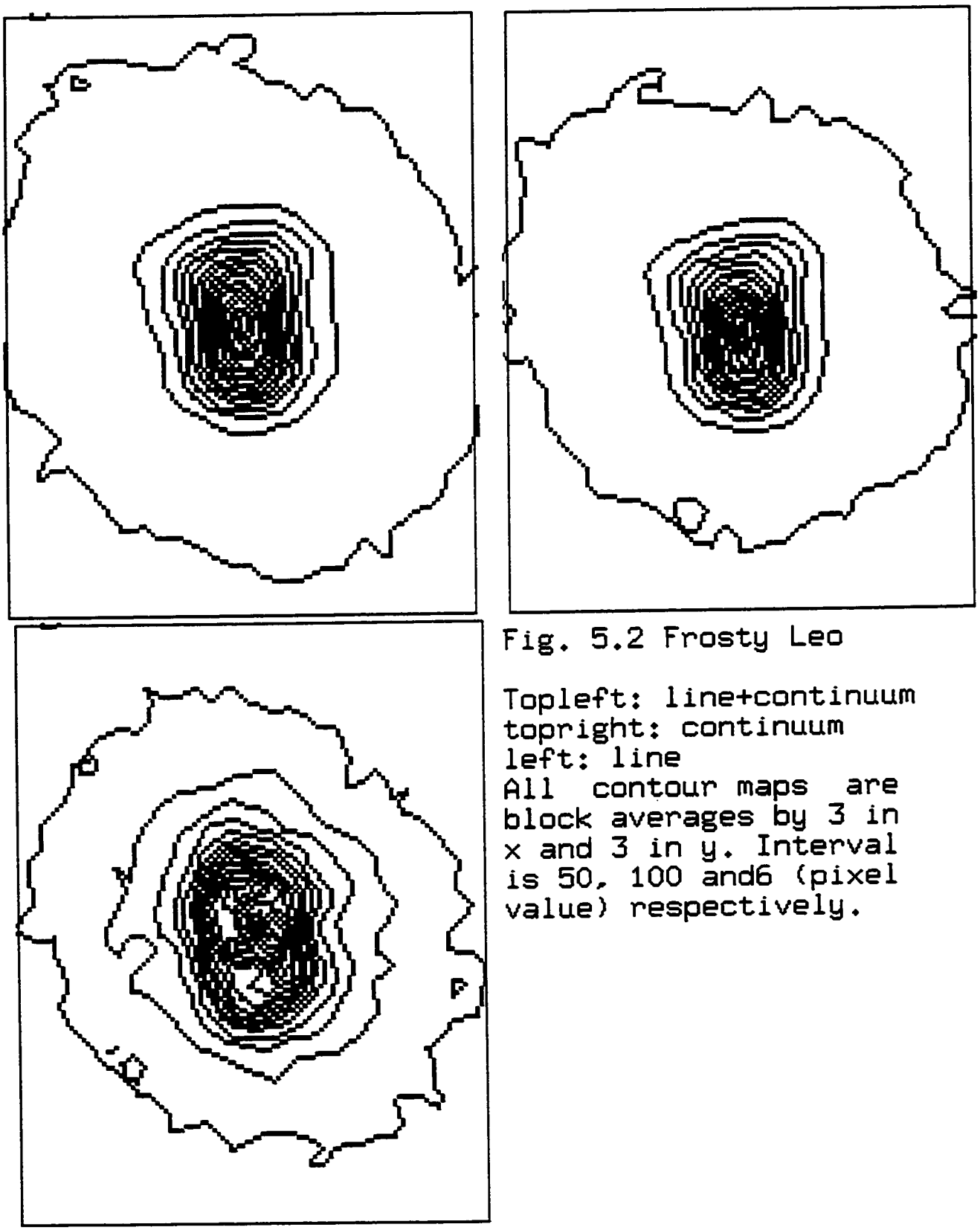

Fig. 5.2 Frosty Leo

Topleft: line+continuum
topright: continuum
left: line
All contour maps are block averages by 3 in x and 3 in y. Interval is 50, 100 and6 (pixel value) respectively.

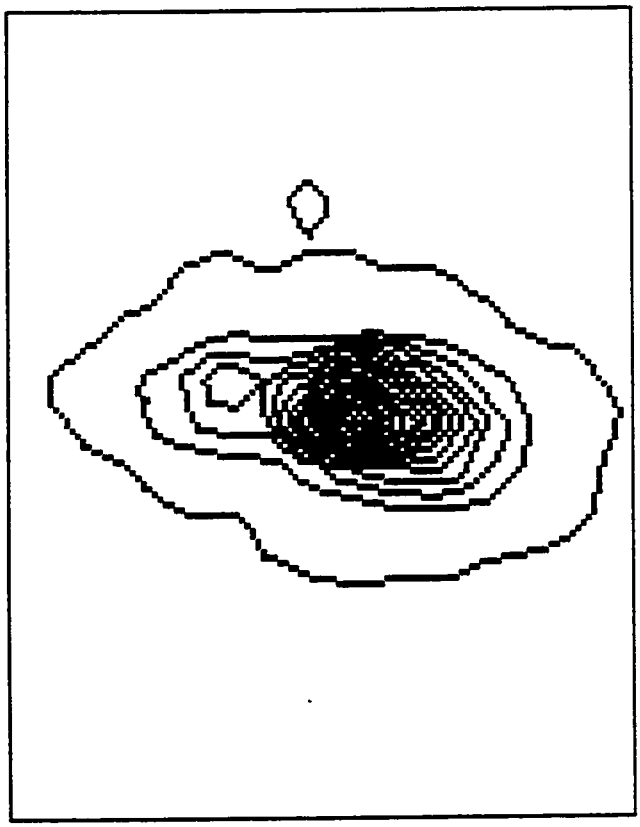

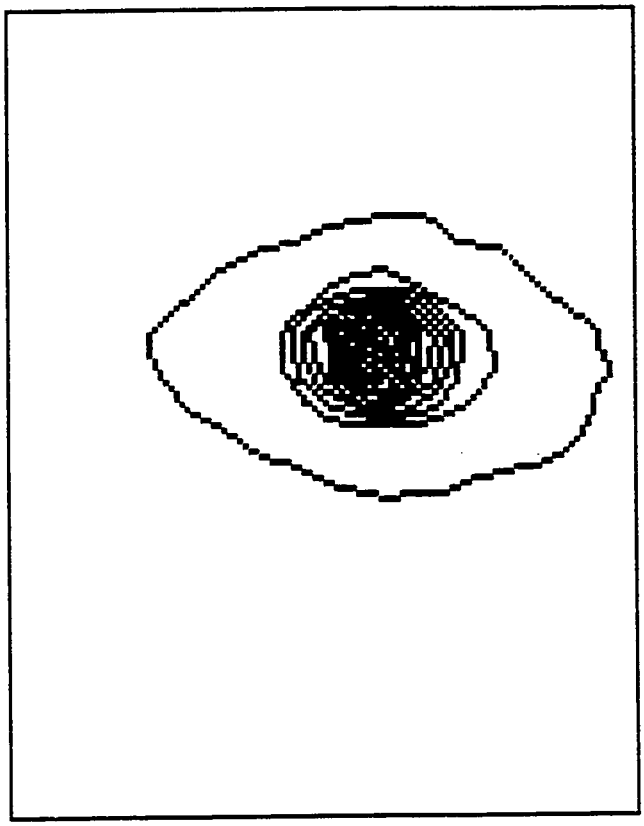

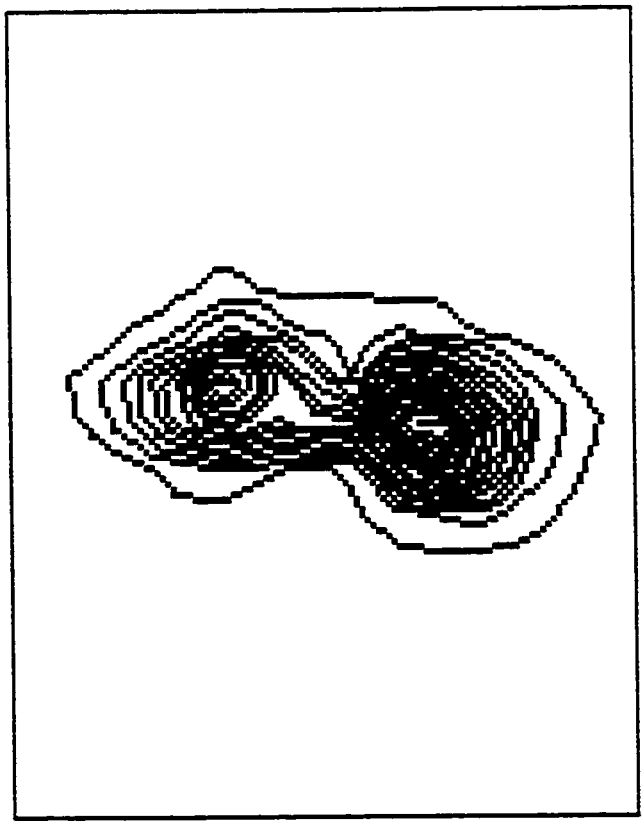

Fig. 5.3 AFGL618

Topleft: line+continuum
topright: continuum
left: line
All contour maps are block averages by 5 in x and 5 in y. Interval is 20, 40 and 5 (pixel value) respectively.

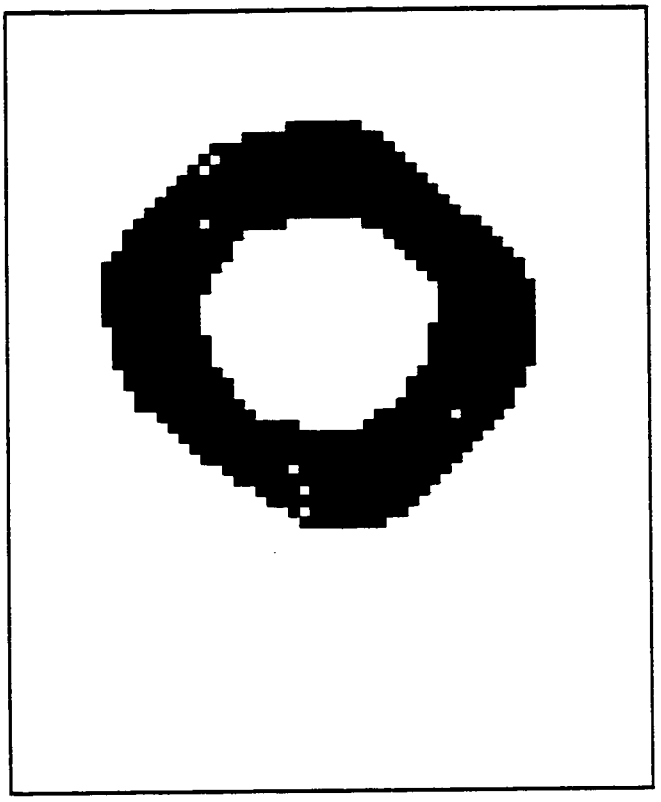

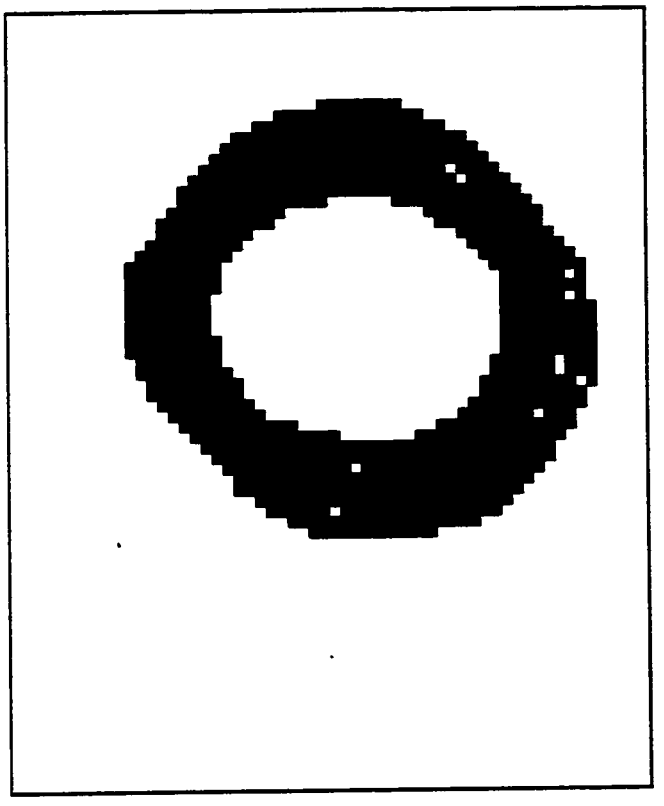

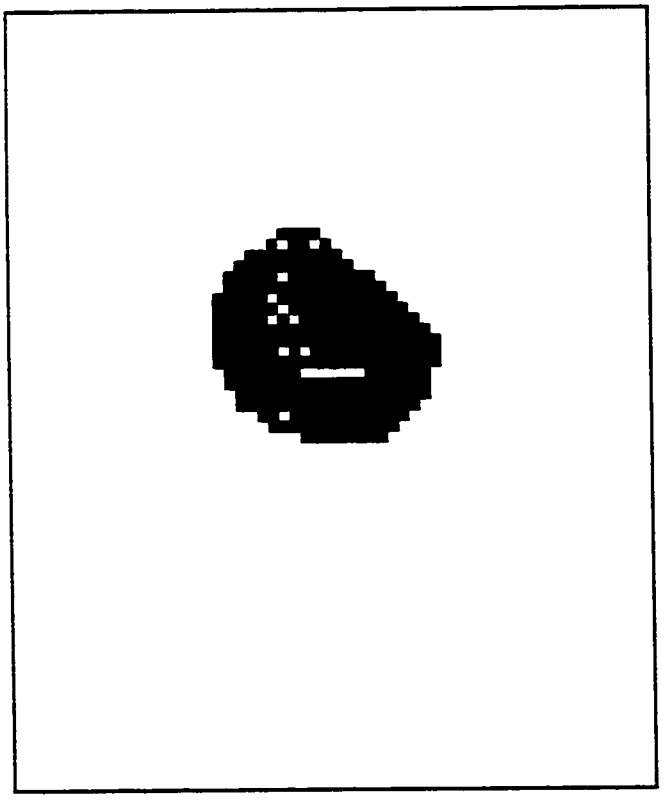

Fig. 5.4 Hu2-1

Topleft: line+continuum
topright: continuum
left: line
All contour maps are block averages by 5 in x and 5 in y. Interval is 0.5 (pixel value).

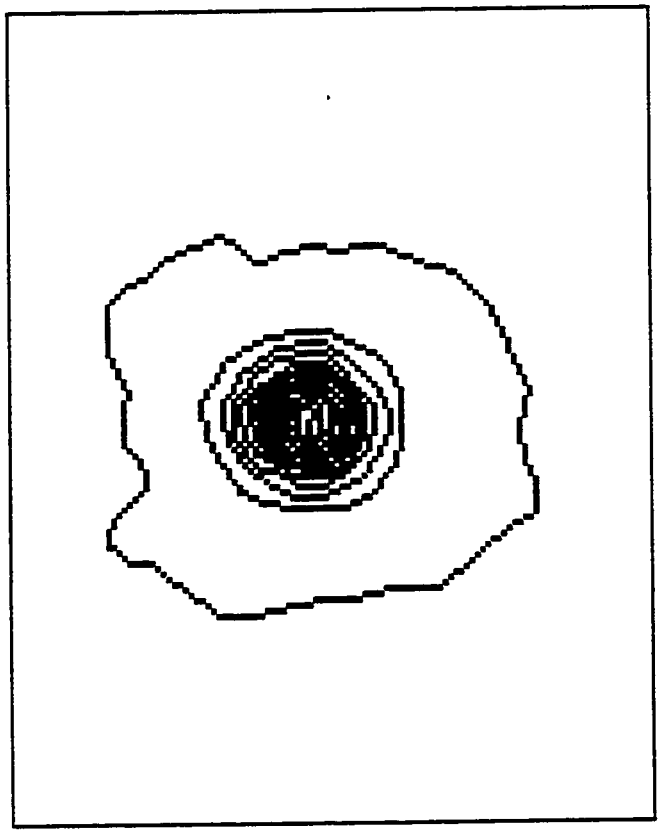

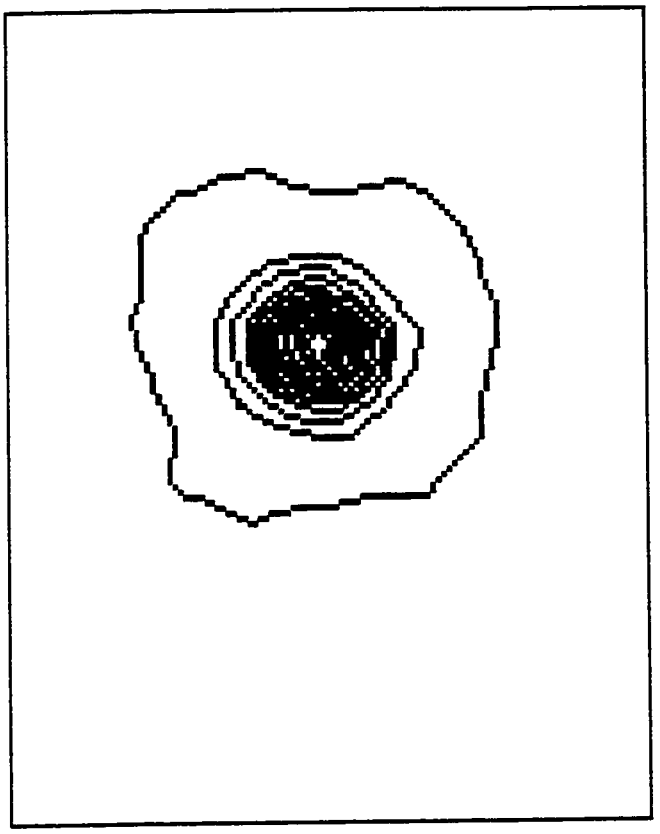

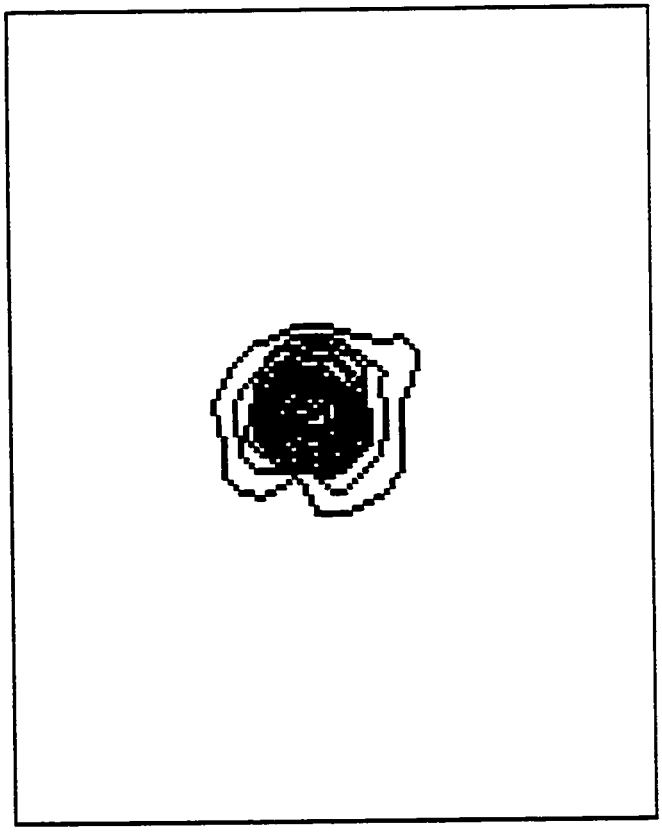

Fig. 5.5 Hb12

Topleft: line+continuum
topright: continuum
left: line
All contour maps are block averages by 5 in x and 5 in y. Interval is 3 (pixel value).

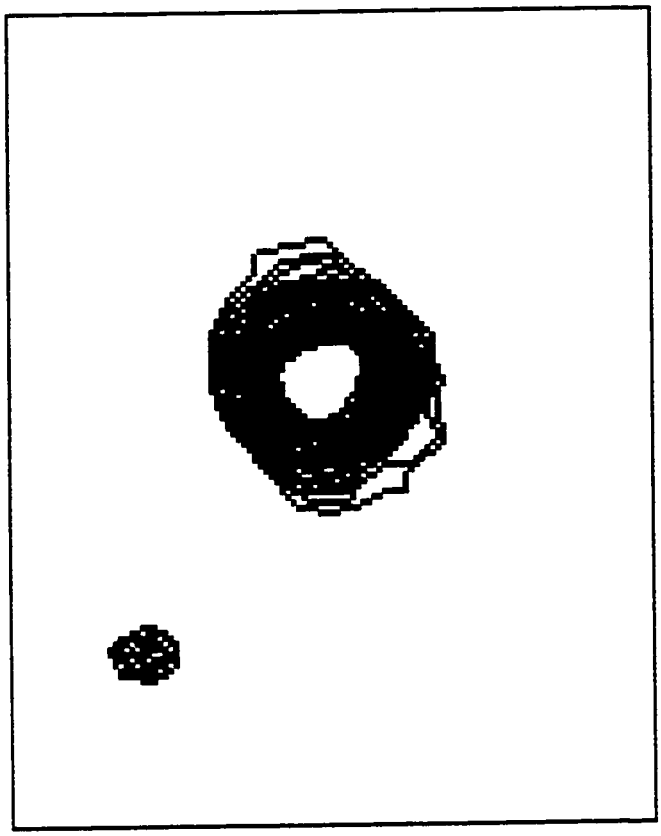

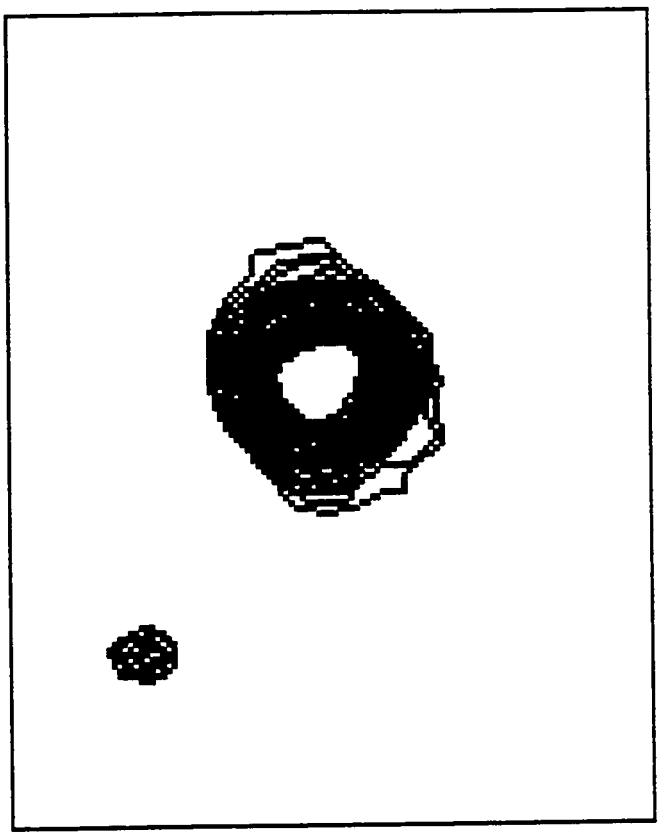

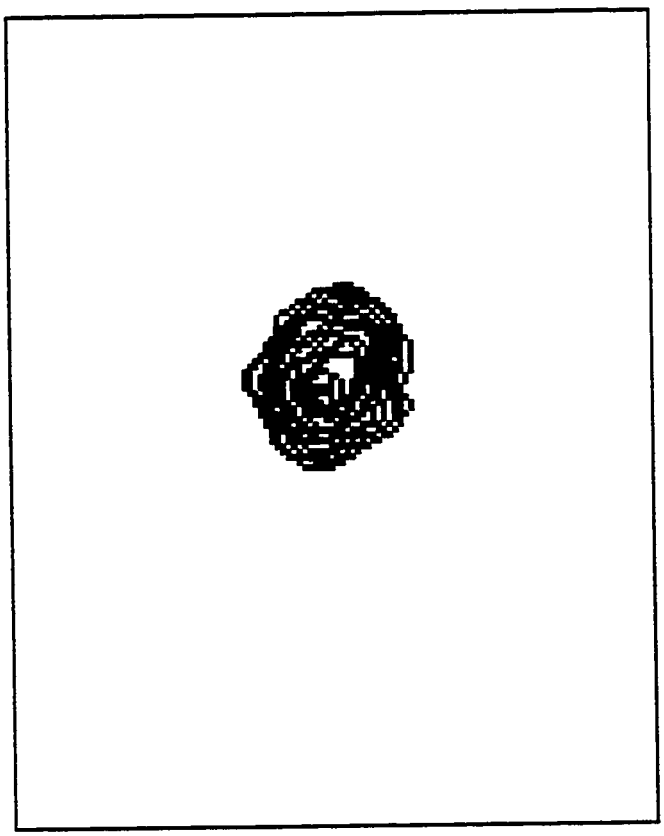

Fig. 5.6 NGC6881

Topleft: line+continuum
topright: continuum
left: line
All contour maps are block averages by 3 in x and 3 in y. Interval is 1 (pixel value).

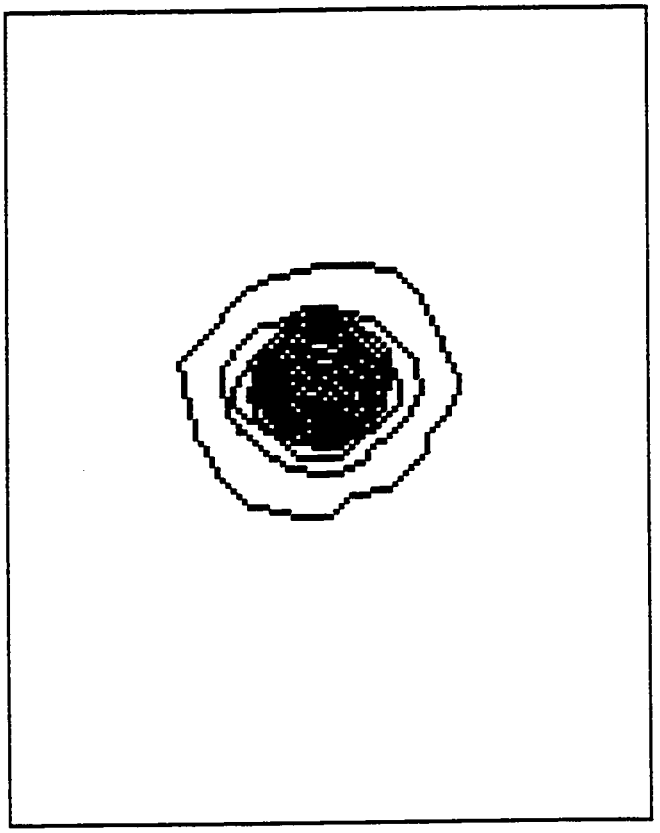

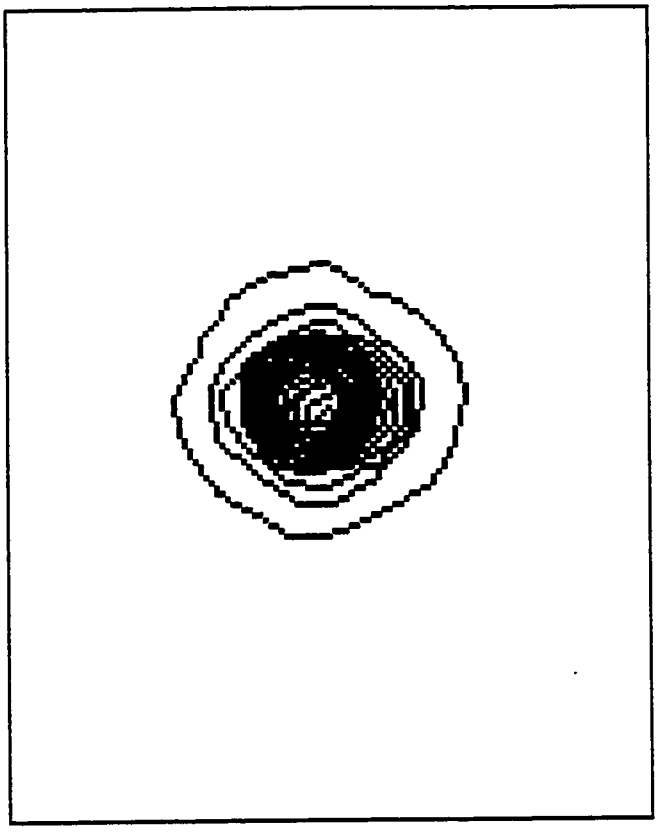

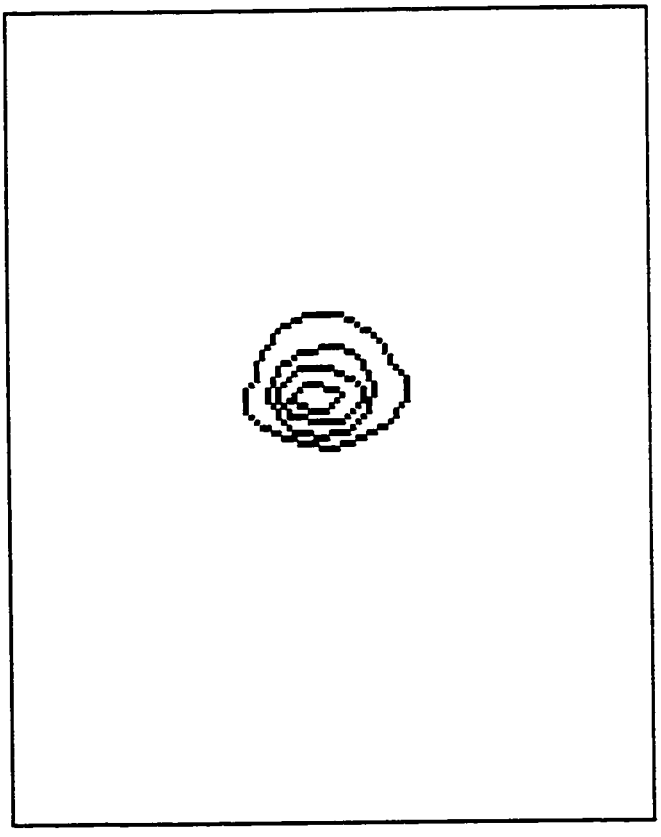

Fig. 5.7 IC4997

Topleft: line+continuum
topright: continuum
left: line
All contour maps are block averages by 5 in x and 5 in y. Interval is 10 (pixel value).

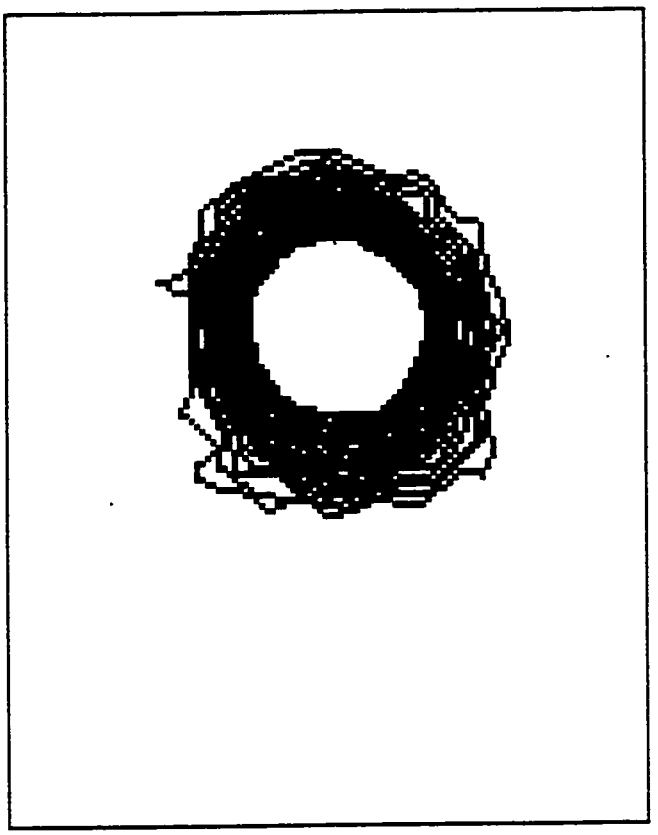

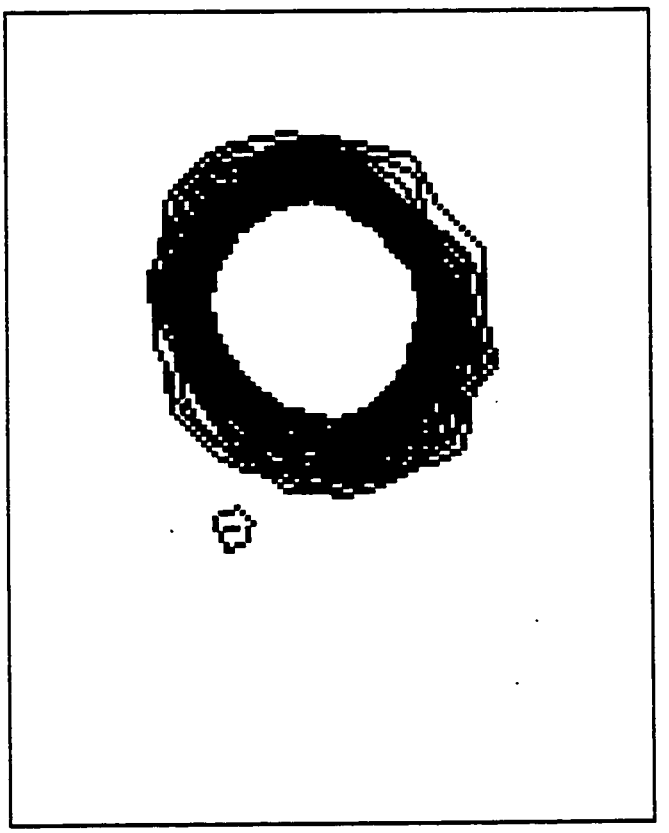

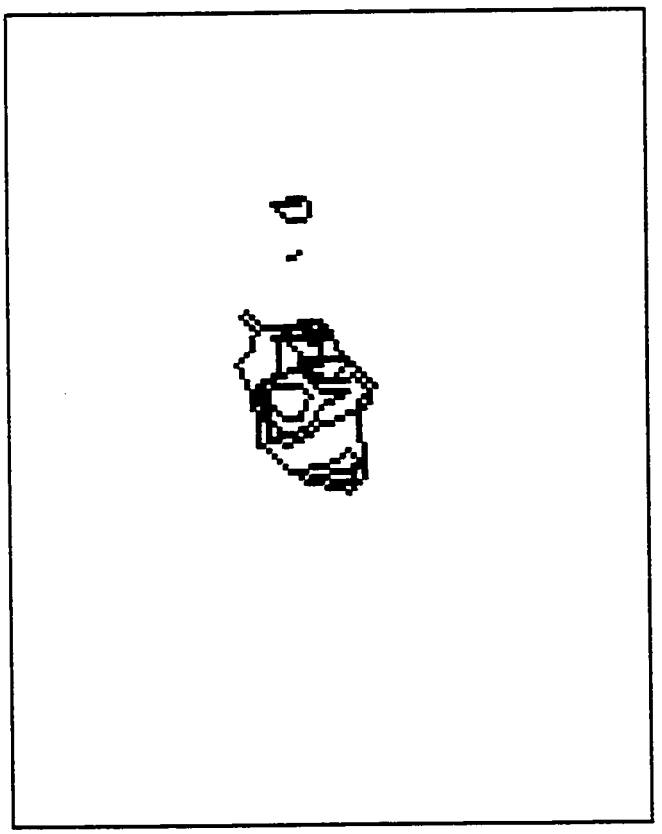

Fig. 5.8 21282+5050

Topleft: line+continuum
topright: continuum
left: line
All contour maps are block averages by 3 in x and 3 in y. Interval is 0.5 (pixel value).

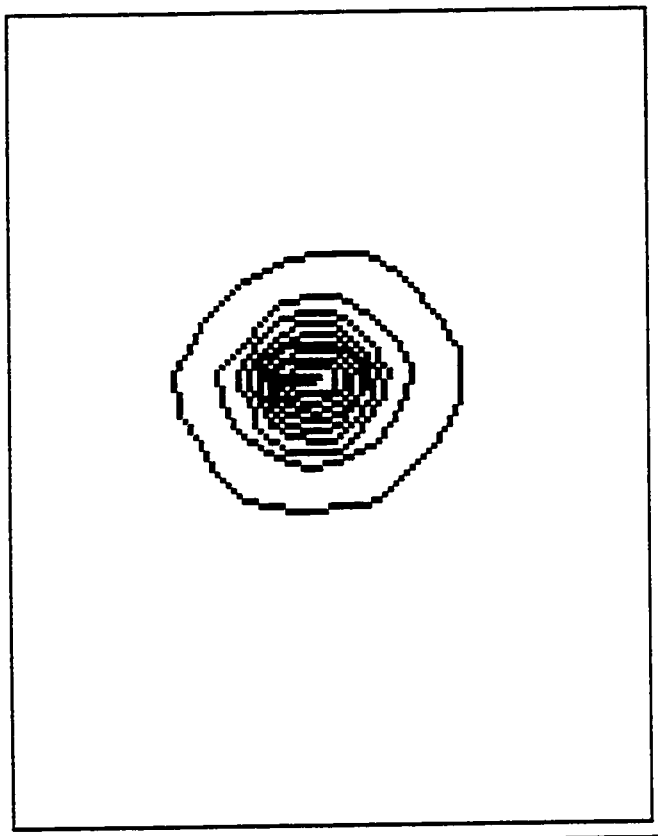

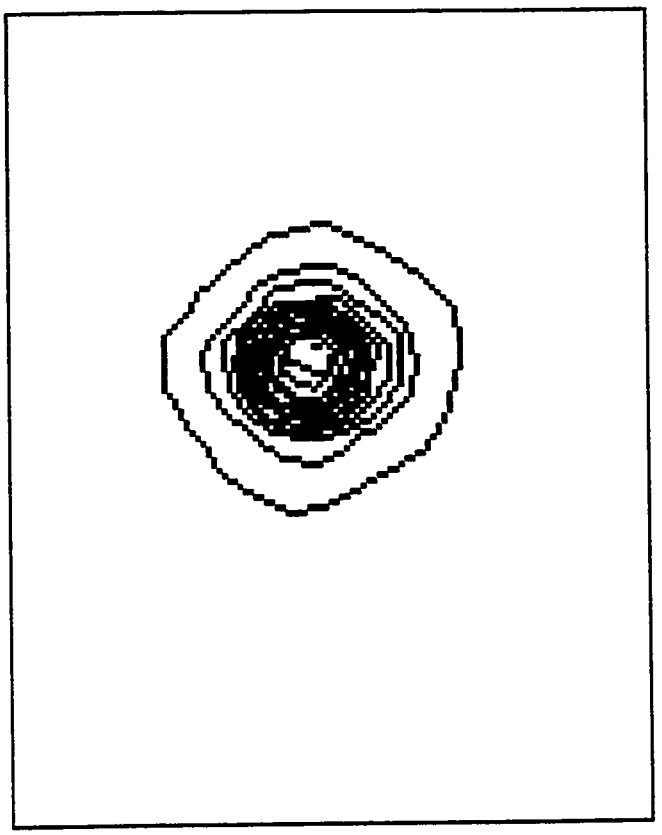

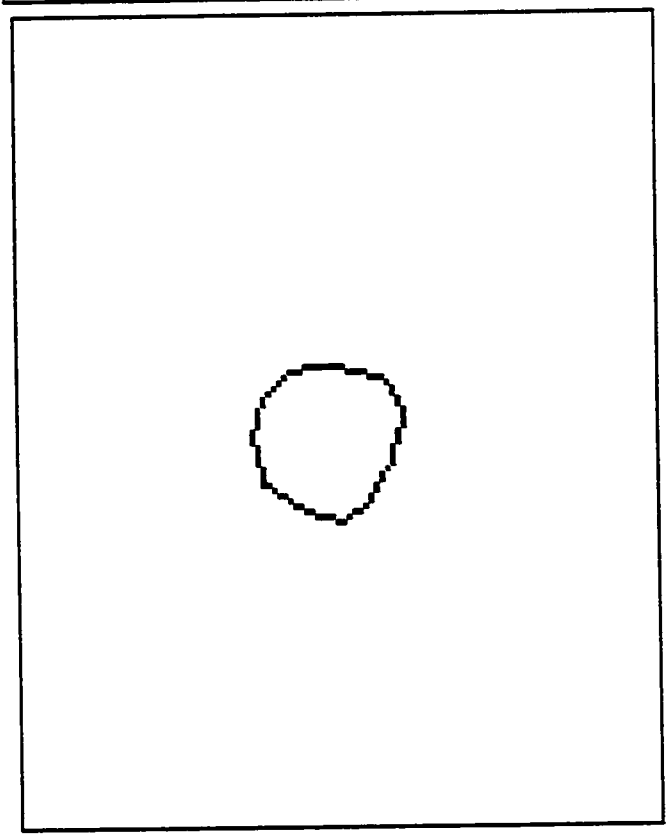

Fig. 5.9 M3-35

Topleft: line+continuum
topright: continuum
left: line
All contour maps are block averages by 5 in x and 5 in y. Interval is 20 (pixel value).

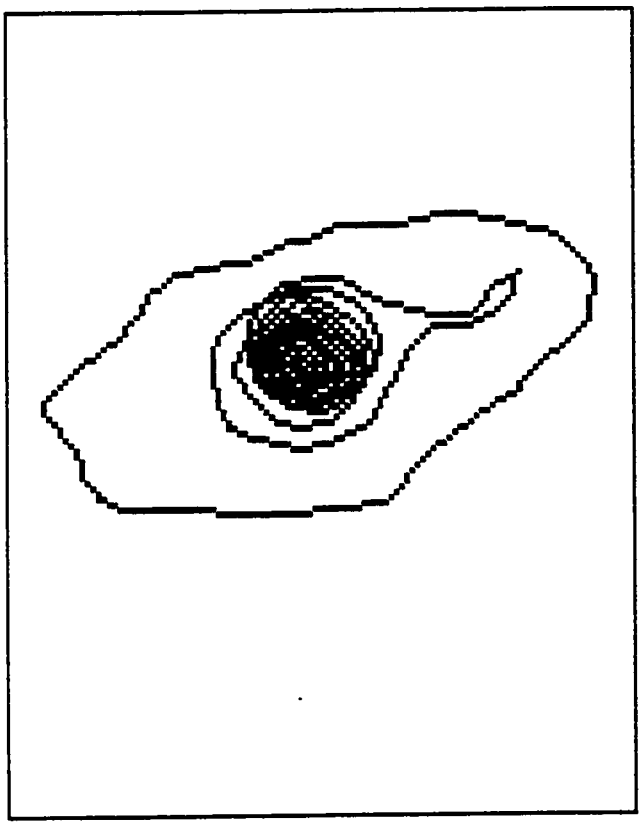

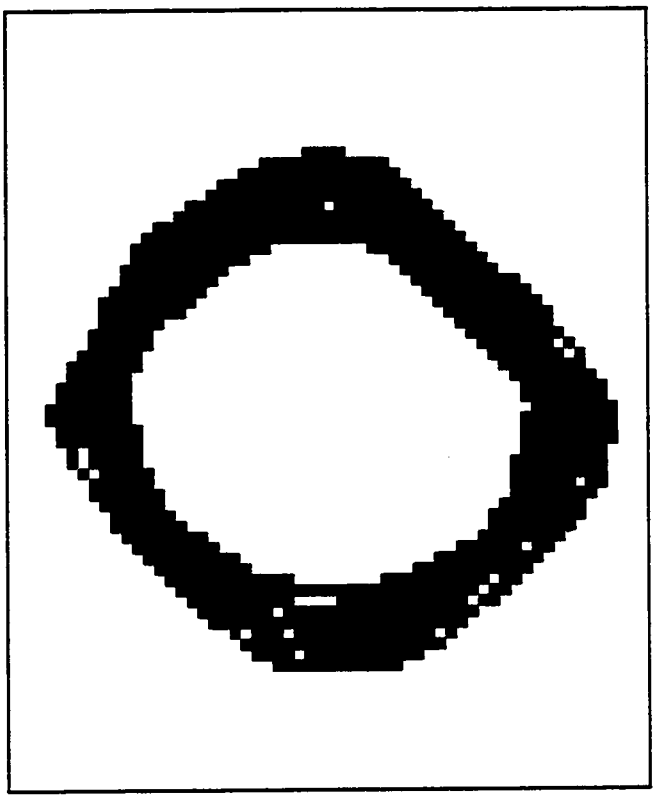

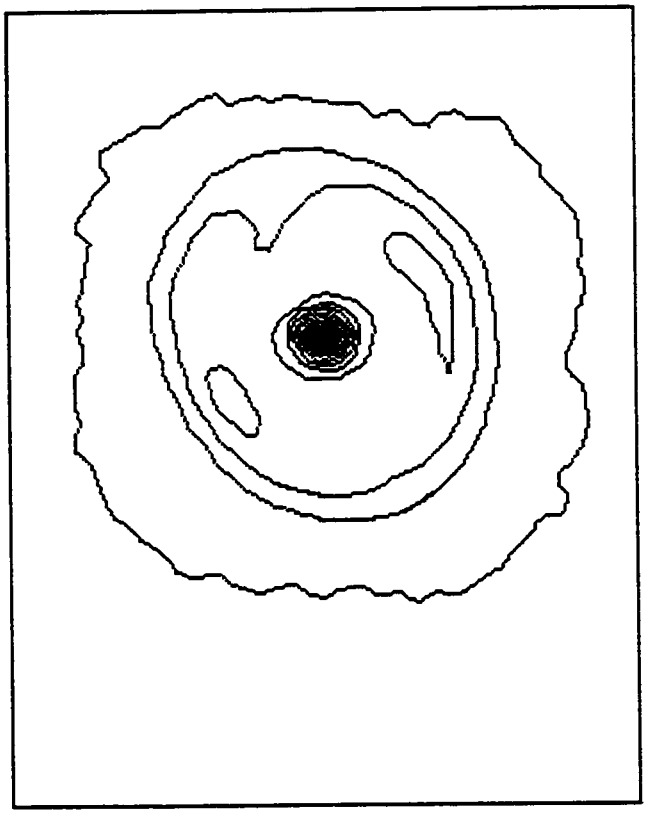

Fig. 5.10 Continuum contour maps

Topleft: IC2149
topright: IC5117
left: IC418
The contour maps are block averages by 5x5, 5x5, 4x4 and interval is 0.5, 9 and 20 (pixel value) respectively.

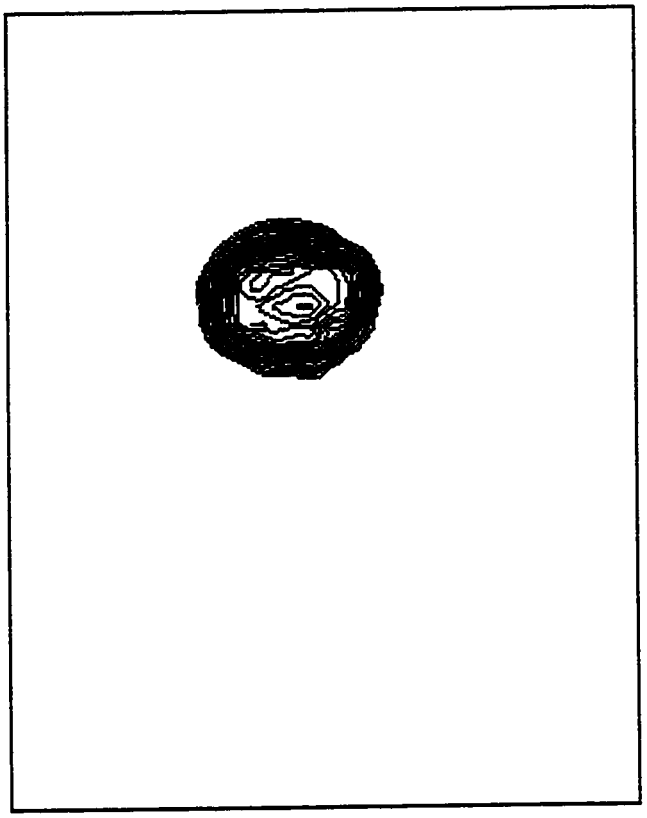

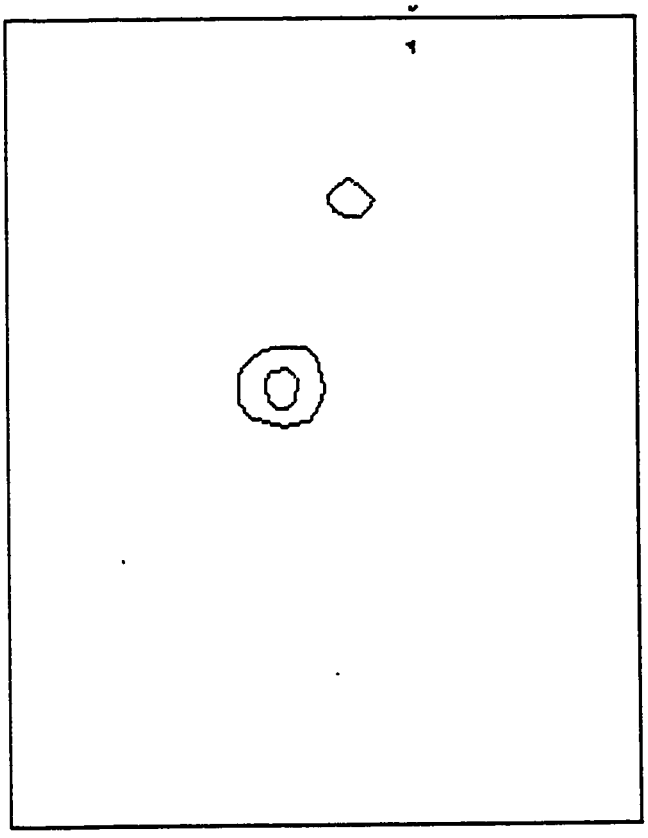

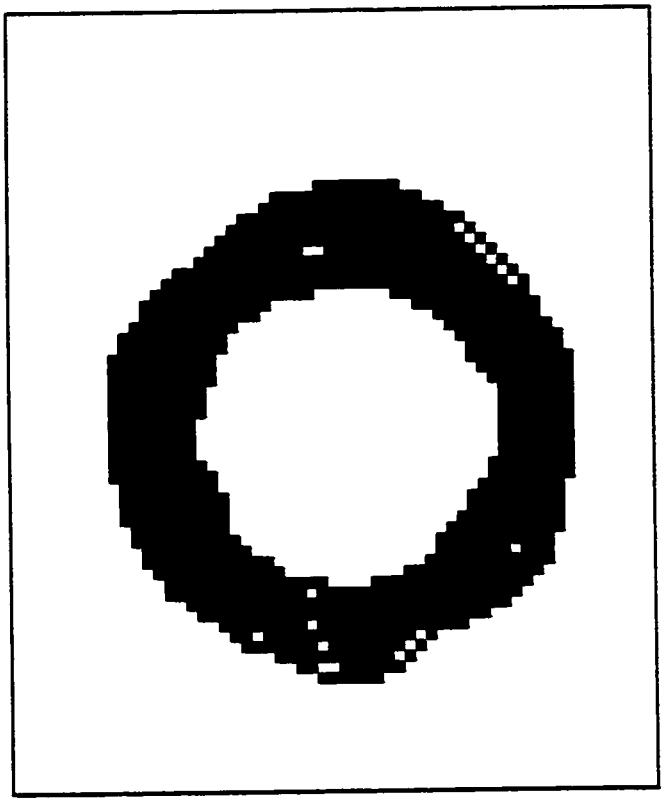

Fig. 5.10 Continuum contour maps

Topleft: IC2165
topright: K3-52
left: M4-18
The contour maps are block averages by 5x5, 4x4, 5x5 and interval is 20,0.6 and 20 (pixel value) respectively.

Chapter 6 Planetary Nebulae Morphologies, Central Star Masses and Molecular Hydrogen Emission

6.1 Introduction

The correlation between PN morphologies and H_2 detection was first suggested by Webster et al. (1988). In the survey of 22 PNe, strong H_2 emission was detected in 11 of these, and all planetaries with strongly excited molecular hydrogen belong to a particular class of PNe--bipolar PNe. They explained that: (1) bipolars arise from massive progenitors and massive progenitors may lead to a larger mass of ambient material accumulating around the post-AGB star or to greater mass loss at the AGB stage. This could lead to more suitable conditions for the formation and preservation of H_2; (2) most BPNe contain the hottest and probably most luminous central stars, leading to very high ionization levels in the nebular shells. Thus, the ultraviolet radiation may be more suitable for excitation of the vibrational levels from which the infrared H_2 lines arise; and (3) BPNe have high expansion velocities because of their hot central stars. If the excitation mechanism is shock excitation, which is favoured at present, then these high expansion velocities may produce shocks with appropriate temperatures to excite the required levels.

The correlation between H_2 detection and BPNe was proven by further researches. Hora and Latter (1997) reported on results from a program of studying the distribution of

molecular hydrogen emission in BPN by high spatial resolution imaging in the 2.12μm line and nearby continuum. Most of the BPN observed had spatially distinct H_2 emission in the equatorial region and/or the bipolar lobes, confirming previously observed correlations between BPN and H_2 emission.

The relations between PN morphologies and central star masses, and between central star masses and expansion velocities, were studied by Gorny et al. (1997). Statistics of 80 PNe shows that (1) BPN, compared to the other morphological classes, have the highest mean value of central star masses; (2) a poor correlation between the nebular expansion velocity and central star mass was found.

However, the direct correlation between H_2 emission, central star masses and expansion velocities has not been studied yet. H_2 emission observations are accumulating. We collected as many as possible PNe H_2 observation and compared the distribution obtained for different morphological types. We investigate the relation between H_2 emission, BPN, central star masses and expansion velocities. That means the relation between H_2 emission and BPN, BPN and central star masses, H_2 emission and central star masses, BPN and expansion velocities, and H_2 emission and expansion velocities.

6.2 Shapes and Morphological Classes

We use the classification of Balick (1987), defining four broad morphological classes:

round or ring (R), elliptical (E), butterfly or bipolar (B) and irregular(I) which doesn't belong to any class above.

Table 6.1.and 6.2. list all the H_2 observation of PNe with positive and null detection. Column 1 is object name. Column 2 lists the morphological type, which based on published photographs of varying quality. Column 3 lists the central star masses. The data are mainly from two papers. First we use the data of Gorny et al. (1997). For the PNe are not listed in it, then we obtained from Zhang & Kwok (1993), both values derived from their two models, termed A and B. Column 4 lists the expansion velocities.

6.3. The Relations Between H_2 Emission, PN Morphologies, Central Star Masses and Expansion Velocities

6.3.1 The Correlation Between H_2 Emission and BPN

Fig 6.3 presents the positive and null H_2 detection number among the defferent morphological classes. It indicates a strong correlation between H_2 emission and BPN. If we take account of some round, which, in fact, are bipolar but observed at pole-on, and the elliptical, which, in fact, are bipolar but presenting elliptical because of the resolution of instruments, the number of bipolar or butterfly nebulae will be larger and the correlation might be stronger. From the diagram we know that 72% positive H_2 detection

Table 6.1 Positive detection with H_2

Name	Type	M($M_\odot$)	V_{exp}(km/s)
J900	B	0.615	18.0
NGC2346	B	0.598(0.598)	8.0(12.5)
NGC2440	B	0.932	22.5
NGC2818	B	0.940	35.5(36.0)
NGC2899	B	0.562(0.563)	23.5(25.0)
Hf 48	B		
NGC5189	B	0.578(0.572)	36.0(24.5)
IC4406	B	0.756	<6.0(14.0)
He 2-111	B		12.0
He 2-114	B		7.5(12.0)
Mz 1	B	0.696	<6.0
NGC6072	B	0.910	<6.0(10.0)
Mz 3	B	0.615(0.628)	
M 2-9	B	0.560(0.554)	
NGC6302	B	0.836(0.836)	8.0
M 1-16	B		
He 2-161	B	0.573(0.565)	
He 2-84	B		
He 2-37	B		30.7
He 2-169	B	0.650(0.669)	
NGC6445	B	0.852	38.0
NGC7293	B	0.930	14.0(24.0)
Hb 12	B	0.800(0.802)	14.0
AFGL2688	B		
AFGL618	B		
AFGL915	B		
Frosty Leo	B		
NGC6881	B	0.703(0.722)	16.5
Hu 2-1	B	0.712(0.730)	9.5(17.0)
K 3-93	B		
M 1-7	B	0.598(0.598)	12.0
M 2-53	B		11.0
M 4-14	B	0.594(0.594)	
NGC4071	E	0.698	14.1
NGC6720	E	0.590(0.590)	26.5
NGC6772	E	0.601	10.2(25.0)
NGC6853	E	0.598(0.598)	15.0(31.5)
NGC7027	E	0.652	21.5(23.5)
NGC7662	E	0.626(0.634)	27.5(29.0)
NGC6781	E	0.573	12.0
IC4997	R	0.772(0.785)	14.5(21.5)
NGC3132	R		14.7(21.0)
BD+30	R	0.703(0.724)	23.0(28.0)
M 1-78	R		
IC5117	R	0.802(0.804)	16.5(21.5)
NGC6210	I	0.605	21.0(35.5)

Table 6.2 Null or faint detections

Name	Type	M($M_\odot$)	V_{exp}(km/s)
NGC246	R		39.0
NGC1360	R	0.558(0.587)	28.0
NGC1535	R	0.581	20.0
NGC3195	R	0.570(0.564)	25.5(30.0)
Me 2-1	R	0.724	13.0
NGC6572	R	0.657(0.680)	16.0
NGC6790	R	0.805(0.807)	15.0
NGC6884	R	0.634(0.667)	23.0
NGC7009	R	0.605	14.0(20.0)
M 4-18	R		<7.5(17.0)
K 3-52	R		
21282+5050	R		
M 3-35	R		17.0(30.0)
IC2149	I	0.577	<10.0(20.0)
NGC6778	I	0.607	20.0
NGC3699	B	0.650(0.650)	26.6(28.0)
Hb 5	B	0.644(0.660)	
He 2-36	B		
He 2-95	B		
IC418	E	0.573	<6.0(12.0)
IC2165	E	0.617	20.0
NGC2792	E	0.606	19.5
NGC3242	E	0.603	20.0(27.5)
NGC6153	E	0.603	17.5(17.0)

are butterfly or bipolar. 54% null detections are round or ring PNe.

6.3.2 The Central Star Masses Distribution for Different Morphological Types

Table 6.3. compares, for the different morphological types, the mean and standard deviation of the central star masses. The number of PN with derived central star masses in each class is given in parenthesis. This table indicates that the bipolar PN have, on average, higher central star masses than the rest of PN in the sample. In particular, bipolar PN tend to have higher central star masses than elliptical PN and round ones (however, the statistics is rather poor in the latter case). But, bipolar PN, compared to the other morphological classes, have the widest distribution of central star masses.

Table 6.3 Central star masses distribution for different morphological type

		M($M_\odot$)	
type	number	A	B
bipolar	23	0.709(0.130)	0.712(0.130)
elliptical	12	0.612(0.033)	0.612(0.034)
round	11	0.674(0.088)	0.684(0.087)
irregular	3	0.596(0.014)	0.596(0.014)

6.3.3. The Relation Between H_2 Emission and Central Star Masses

Table 6.4. lists the mean values of central star masses of positive and null H_2 detection groups. It is very clear that, on average, those PNe with positive H_2 detection have higher

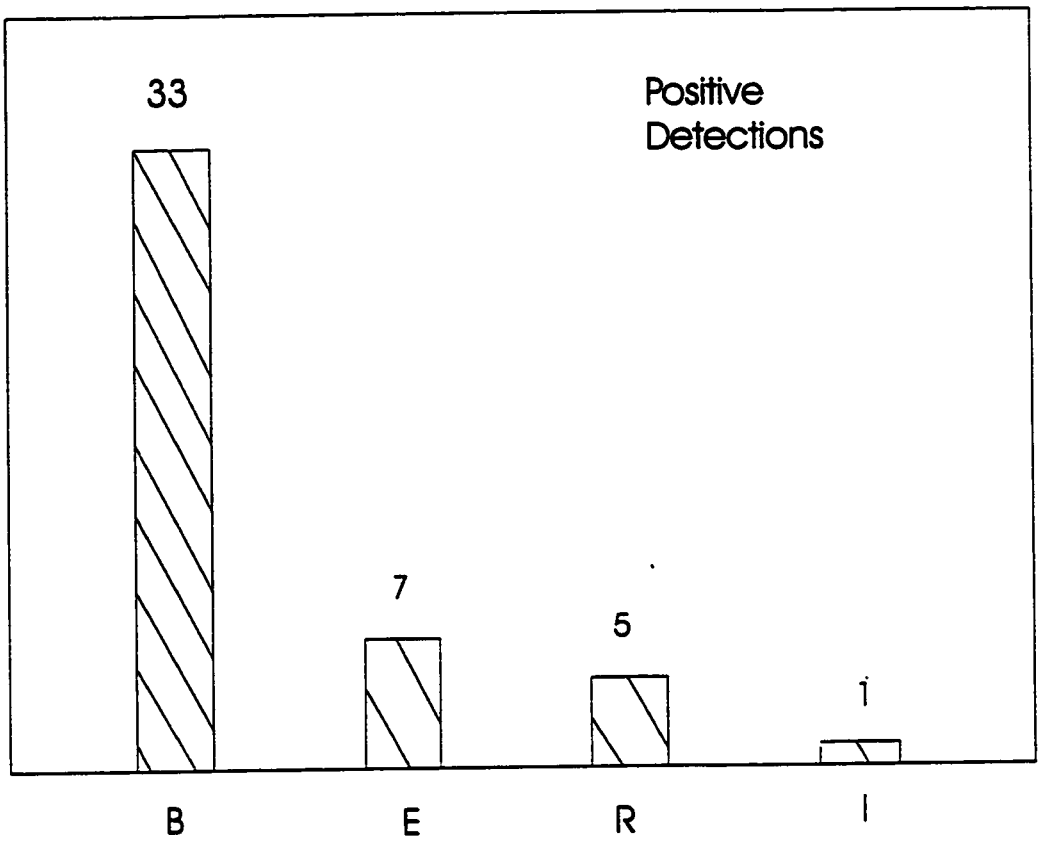

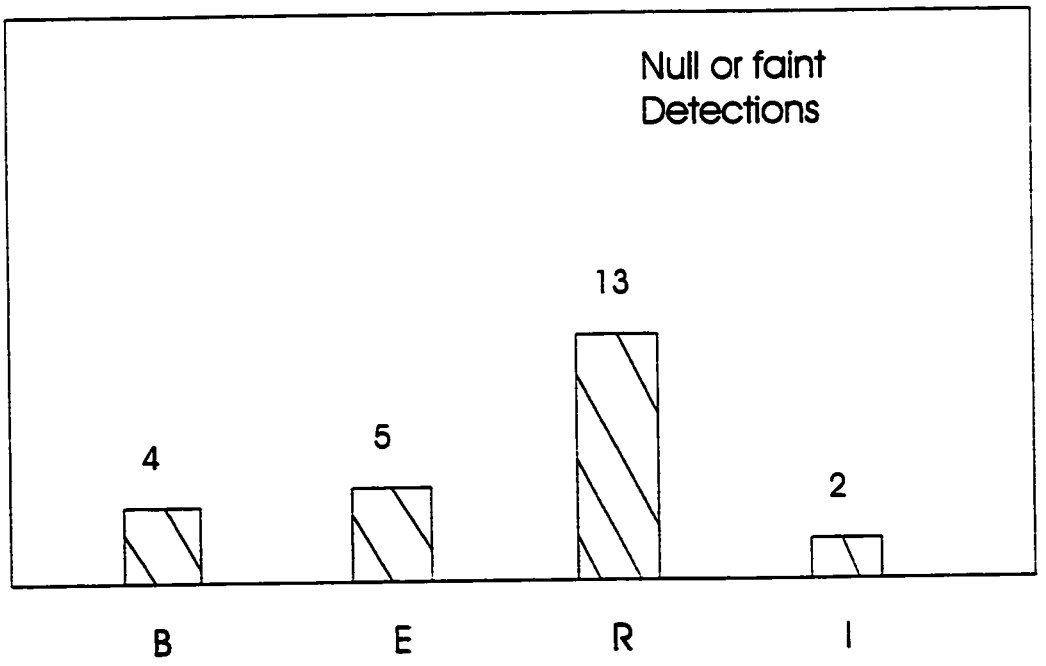

Fig.6.1: Morphological types distribution

central star masses than those with no H_2 detection. This agrees with the explanation of Webster et al. (1988).

Table 6.4 Central star masses related to the H_2 emission

		M($M_\odot$)	
	number	A	B
positive detection	32	0.695(0.120)	0.701(0.124)
null detection	17	0.624(0.060)	0.630(0.061)

6.3.4 The Relation Between Morphological Types and Expansion Velocities

Table 6.5. lists the mean expansion velocities for different morphological types. No relation was found. The standard deviations are so large that we can't find the relation between them.

Table 6.5 Different type PNe with expansion velocity

		expansion velocity(km/s)	
type	number	A	B
bipolar	21	17.2(10.4)	18.7(8.9)
elliptical	13	17.5(6.0)	21.5(6.0)
round	15	19.1(7.4)	22.9(6.7)
irregular	3	17.0(5.0)	25.2(7.3)
positive	32	17.2(8.9)	20.4(8.5)
null	19	18.9(7.5)	21.8(6.7)

6.4 Galactic Distribution

The space distribution of planetary nebulae shows a pronounced concentration to the galactic plane. A general concentration towards the galactic centre is also observed. The distribution of PNe with H_2 emission, as part of PNe, concentrate to the galactic plane too. The H_2 emission (Webster et al. 1988;Zuckerman & Gatley 1988) is correlated with galactic latitude, bipolarity. We reexamine this correlation and the result is listed in Table 6.6. Since the total number observed by H_2 detections around the galactic centre is small, the distribution doesn't show any concentration.

Table 6.6 Latitude distribution of PNe

	number	latitude	deviation
positive	42	7.0	10.2
null	23	17.0	18.8
BPNe	33	7.0	9.7
not BPNe	32	15.8	16.8

38 out of 42 PNe with positive detections are concentrate between b=-15 and +15 while 53 out of 65 all PNe with positive and null detections concentrate in this region.

A rough statistics on the central star masses is listed in table 1. Statistics shows that the central star masses decrease when longitudes increase for all PNe observed by H_2 detections, as well for those with null H_2 detections, while those with positive H_2 detections do not show this relation but show higher central star masses in general.

Table 6.7 Central star masses distribution in Galactic

longitude	positive	null	all
0–|30|	A:0.757(0.136)(5)	0.657(0.050)(3)	0.720(0.122)(8)
	B:0.758(0.136)	0.662(0.049)	0.722(0.121)
|30|-|90|	A:0.672(0.093)(19)	0.647(0.070)(7)	0.666(0.088)(26)
	B:0.677(0.095)	0.654(0.073)	0.671(0.090)
|90|-|180|	A:0.730(0.146)(7)	0.588(0.020)(7)	0.650(0.126)(14)
	B:0.731(0.145)	0.592(0.015)	0.662(0.124)

6.5 Discussion

We investigated the correlations between H_2 emission and BPN, BPN and central star masses, H_2 emission and central star masses, BPN and expansion velocities, and H_2 emission and expansion velocities. However, the last two correlations were not found and the second and the third correlations are poor. These may be due to the selection effect and also the uncertainty of central star derivations. In fact, whether we detect H_2 or not from a planetary nebula is related to the formation, dissociation, excitation, and emission intensity of H_2 molecules. When we investigate the relations, how the BPNe are formed is important. It is now a generally accepted idea that a planetary nebula is

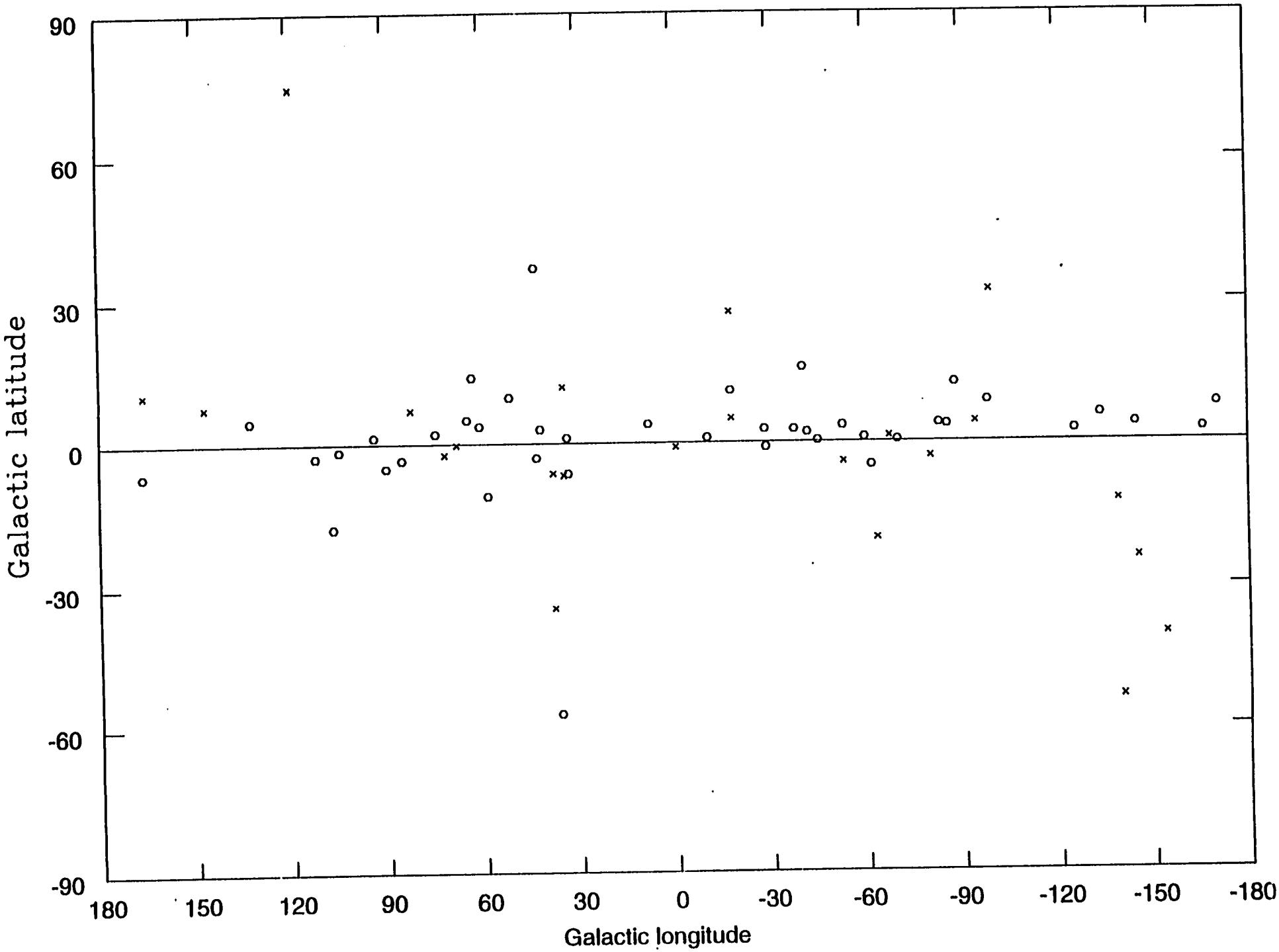
90
60
30
0
-30
-60
-90
Galactic latitude
180
150
120
90
60
30
0
-30
-60
-90
-120
-150
-180
Galactic longitude

formed from the gas lost by a low- to intermediate mass star, during the AGB phase. Work of e.g. Habing et al. (1989), shows that the late AGB stars are indeed the most likely progenotors of PN stars. As the material surrounding them moves out, and mass loss stops, a PN may form.

One of the more successful scenarios for the formation of spherical PNe from this AGB-wind remnant is the interacting winds model (ISW), proposed by Kwok et al. (1978). According to this model, a PN forms through the interaction of a fast wind, originating from the central star, with the AGb-wind remnant (or slow wind).

The ISW model offers a nice explanation for the asphericity of many PNe. As Balick (1987) pointed out, one can obtain many of the different observed morphologies by assuming a density distribution of what is taken to be axisymmetric with higher densities in the equatorial plane and lower densities in the direction of the polar axis. Balick proposes a morphological scheme in which the form of PNe varies from round (R) through elliptical (E) to butterfly (B) shapes, and he explains this sequence as one of increasing density ratio between pole and equator.

Numerical hydrodynamical simulations (Mellema et al. 1991) of the emergence of aspherical planetary nebulae show that a wide range of morphologies can be formed by assuming that intermediate-mass stars, in thermal phases of their evolution, lose mass in at least two successive hydrodynamical stages. During the first stage, which presumably

takes place while the star is on the AGB phase, the stellar wind is slow, dense, and aspherical. The second stage consists of a fast, tenuous, spherical wind which collides with the remnants of the preceding slow wind. The interaction between these two winds produces a pattern of hydrodynamic events which gives rise to nebular shapes that can be identified with observed morphologies. The elliptical and "butterfly" type nebulae form as a consequence of different density distributions in the slow wind.

Numerical hydrodynamical models (Mellema 1997) support the connection between massive stars and PNe with a bipolar morphology. The model shows that it is more difficult for lower mass stars to acquire a PN with bipolar morphology, even if the initial conditions are favourable. The reason for this is that for lower mass stars the ionization front is more likely to modify the surrounding density distribution, making it less equatorially concentrated. To produce bipolar nebulae one needs a density distribution with a high degree of concentration towards the equator. Around more massive stars the original density structure is more likely to remain intact because either the material is so dense that it remains neutral and the ionization front lies within the wind sept shell, or the ionization is almost instantaneous (because of the rapid evolution) and does not modify the density structure.

Since an equatorially concentrated, disk-like density distribution is required for the formation of bipolar shapes, any mechanism giving rise to aspherical mass loss on the AGB should be able to produce this type of density distribution.

Chapter 7 Conclusions

Since the first detection of H_2 emission in a planetary nebula, over 70 PNe have been searched for such radiation and detections at some level succeeded in a majority of cases. Molecular hydrogen provides an important probe to investigate planetary nebulae.

Emission line at 2.12μm has been detected in eleven out of fifteen planetary nebulae surveyed. Even though the line is contaminated from HeI 2.114μm, it is clear that eight of them have been detected with H_2 emission. Four detections are new. They are NGC6881, Frosty Leo, Hu2-1 and IC4997. The first three have bipolar or butterfly morphologies.

2.12μm and 2.14μm images are obtained. They give us the information about the morphology, spatial structure (i.e. AFGL618). They are useful for us to compare with the optical and radio or other wavelength images to find out the systematic differences.

The flux at 2.12μm and 2.14μm and FWHM are gotten for each of the fifteen planetary nebulae for the two wavelength.

The statistical study has focused on the relations between the PN morphological types, central star masses, expansion velocities, galactic distribution and H_2 molecular emission.

It has confirmed the previous suggestion that the is a strong correlation between H_2 detection and bipolar or butterfly morphology. If a nebula is detected with H_2 emission, it most probably is a BPN, or vice versa. The new detections and statistics confirmed this correlation.

Bipolar planetary nebulae, compared to the other morphological classes, have the widest distribution of central star masses, with the highest mean value. This is consistent with the fact that, as also found by our studies, they are on average closer to the Galactic plane. The distribution of PN above the Galactic plane as a function of central star mass is qualitatively consistent with the existence of an initial-final mass relation between PN central stars and their progenitors. The wide distribution of central star masses for bipolar planetary nebulae indicates that even though the central star mass play an important role in developing bipolar morphology, the geometrical distribution of the slow winds is more essential.

The new correlation between H_2 detections and central star masses is found. For positive detections, the central star mass is higher, on average, than that of the null detection, even though the deviation is large for positive detections.

The formation, destruction, excitation, distribution of molecular hydrogen in planetary nebulae are studied. However, many aspects are unknown. Using molecular hydrogen as a probe to investigate planetary nebulae needs more works to do.

Bibliography

Aspin, C., Schwarz, H. E., & Smith, M. C. et al. 1993, A&A, 278, 255

Balick, B. 1987, AJ, 94, 671

Balick, B., Preston, H., & Icke, V. 1987, AJ, 94, 1641

Balick, B., Rugers, M., Terzian, Y., & Chengalur, J. 1993, ApJ, 411, 778

Beckwith, S. C., & Beckwith, S. V. W. 1983, ApJ, 271, 175

Beckwith, S. V. W. 1978, PhD thesis, Caltech

Beckwith, S. V. W., Neugebauer, G., Becklin, E. E. & Matthews, K., 1980, AJ, 85, 886

Beckwith, S. V. W., Beckwith, S. C., & Gatley, I. 1984, ApJ, 280, 648

Bignell, R. C. 1983, IAUS, 103, 69

Black, D. C. & Dalgarno, A. 1976, ApJ, 203, 132

Bragg, S. L., Brault, J. W., & Smith, W. H. 1982, ApJ, 263, 999

Burton, m. G. 1992, Aust. J. Phys., 45, 463

Calvet, N., & Cohen, M. 1978, MNRAS, 182, 687

Cox, P., Maillard, J. P. & Huggins, P. J. et al. 1997, A&A, 321, 907

Dinerstein, H. L., Lester, L. F., Carr, J. S. & Harvey, P. M. 1988, ApJ, 327, L27

Dove, J. & Mandy, M. 1986, ApJ, 311, L93

Draine, B. T., Roberge, W. G., & Dalgarno, A. 1983, ApJ, 264, 485

Dunham, J. L. 1932, Phys. Rev., 41, 713

Evens, N. J., Levreault, R. M., Beckwith, S. & Skrutskie, M., 1987, ApJ, 320, 364

Feibelman, W. A., Hyung, S., & Aller, L. H. 1994, ApJ, 426, 653

Fink, U., Wiggins, T. A., & Rank, D. H. 1965, J. Molec. Spec., 18, 384

Forveille, T., Morris, M., Omont, A. & Likkel, L. 1987, A&A, 176, L13

Gorny, S. K., Stasinska, G., & Tylenda, R. 1997, A&A, 318, 256

Gould, R. J. & Salpeter, E. E. 1963, ApJ, 138, 393

Graham, J., Herbst, T. M. & Matthews, K. et al. 1993, ApJ, 403, L105

Greenhouse, M. A., Hayward, T. L., Thronson, H. A. Jr. 1988, ApJ, 325, 604

-----1988, ApJ, 332, 1092

Herzberg, G. 1950 Molecular Spectra and Molecular Structure I. Spectra of Diatomic Molecules, Van Northtrand Reinhold Company

Hodapp, K., Sellgren, K. & Nagata, T. 1988, ApJ, 326, L61

Hora, J. L., Deutsch, L. K., & Hoffmann, W. F. et al. 1993, 413, 304

Hora, J. L., Deutsch, L. K., Hoffmann, W. F., & Fazio, G. G. 1995, Ap&SS, 224, 361

Hora, J. L., & Latter, W. B. 1994, ApJ, 437, 281

-----1996, ApJ, 461, 288

-----1997, BAAS, 9708

Hua, C. T., & Grundseth, B. 1985, AJ, 90, 2055

Hua, C. T., Grundseth, B., & Maucherat, A. J. 1993, A&AS, 101, 541

Isaacman, R. 1984, A&A, 130, 151

Jacoby, G. H., & Kaler, J. B. 1989, AJ, 98, 1662

Jennings, D. E., Bragg, S. L., & Brault, J. W. 1984, ApJ, 282, L85

Jennings, D. E., & Brault, J. W. 1983, J. Molec. Spec., 102, 265

Kahn, F. D. 1955, Mem. Soc. Roy. Sci. Liege, 15, 578

-----1983, IAUS, 103, 305

Kastner, J. H., Gatley, I., Merrill, K. M., Probst, R., & Weintaub, D. 1994, ApJ, 421, 600

Knacke, R. F., & Young, E. T. 1981, ApJ, 249, L65

Kolos, W., & Wolniewicz, L. 1975, J. Molec. Spec., 54, 303

Kwok, S., & Aaquist, O. B. 1993, PASP, 105, 1456

Kwok, S., & Bignell, R. C. 1984, ApJ, 276, 544

Kwok, S., Hrivnak, B. J., & Langill, P. 1993, ApJ, 408, 586

Kwok, S., Purton, C. R., & Fitzgerald, P. M. 1978, ApJ, 219, L125

Kwok, S. 1982, ApJ, 258, 280

----1993, ARA&A, 31,63

----1994, PASP, 106, 344

Langill, P., Kwok, S., & Hrivnak, B. J. 1994, PASA, 106, 736

Latter, W. B., Kelly, D. M., Hora, J., & Deutsch, L. K. 1995, ApJS, 100, 159

Latter, W. B., Maloney, P., & Kelly, D. et al. 1992, ApJ, 389, 347

Louise, R., Macron, A., Pascoli, B., & Maurice, E. 1987, A&AS, 70, 201

McCrea & McNally, 1960, MNRAS, 121, 238

Meixer, M., Skinner, C. J., & Temi, P. et al. 1993, ApJ, 411, 266

Miranda, L. F. 1995, A&A, 304, 531

-------1995, ApJ, 446, L39

-------1996, ApJ, 461, L111

Miranda, L. F., & Solf, J. 1989, A&A, 214, 353

Penner, S. S. 1959 in Quantitative Molecular Spectroscopy and Gas Emissivities, Addison-Wesley Publishing Company

Phillips, J. P., Reay, N. K., & White, G. L. 1983, MNRAS, 203, 977

Phillips, J. P., White, G. J., & Harten, R. 1985, A&A, 145, 118

Roddier, F., Roddier, C., Graves, J. E. & Northcott, M. J. 1995, ApJ, 443, 249

Rouan, D., Lacombe, F., Omont, A. & Forveille, T. 1988, A&A, 189, L3

Schild, H. 1995, A&A, 297, 246

Shibata, K. M., Tamura, S., & Deguchi, S. et al. 1989, ApJ, 45, L55

Shull, J. M. 1978, ApJ, 219, 877

Shupe, D. L., Armus, L., Matthews, K., & Soifer, B. T. 1995, AJ, 109, 1173

Storey, J. W. V. 1984, MNRAS, 206, 521

Struve, W. S. 1989,in Fundamentals of Molecular Spectroscopy, John Wiley & Sons, p105

Tamura, S., Shibata, K. M., & Kazes, I. 1990, A&A, 232, 195

Treffers, R. R., Fink, U., Larson, H. P., & Gautier, T. N. III 1976, ApJ, 209, 793

Thronson, H. A. Jr. 1982, AJ, 87, 1207

Watson, W. D. 1974, in Atomic and Molecular Physics and the Interstellar Matter, North-Holland, P181.

Webster, B. L., Hewett, P. C., Harding, M. E., & Wegner, G. A. 1988, AJ, 95, 19

Webster, B. L., Payne, P. W., Storey, J. W. V., & Dopita, M. A. 1988, MNRAS, 235, 533

Westbrook, W. E., Willner, S.P., & Merrill, K. M. et al. 1975, ApJ, 202, 407

Willner, S. P., Jones, B., Russell, R. W., Puetter, R. C., & Soifer, B. T. 1979, ApJ, 234, 496

Zhang, C. Y., & Kwok, S. 1993, ApJS, 88, 137

Zuckerman, B., & Aller, L. H. 1986, ApJ, 301, 772

Zuckerman, B., & Gatley, I. 1988, ApJ, 324, 501

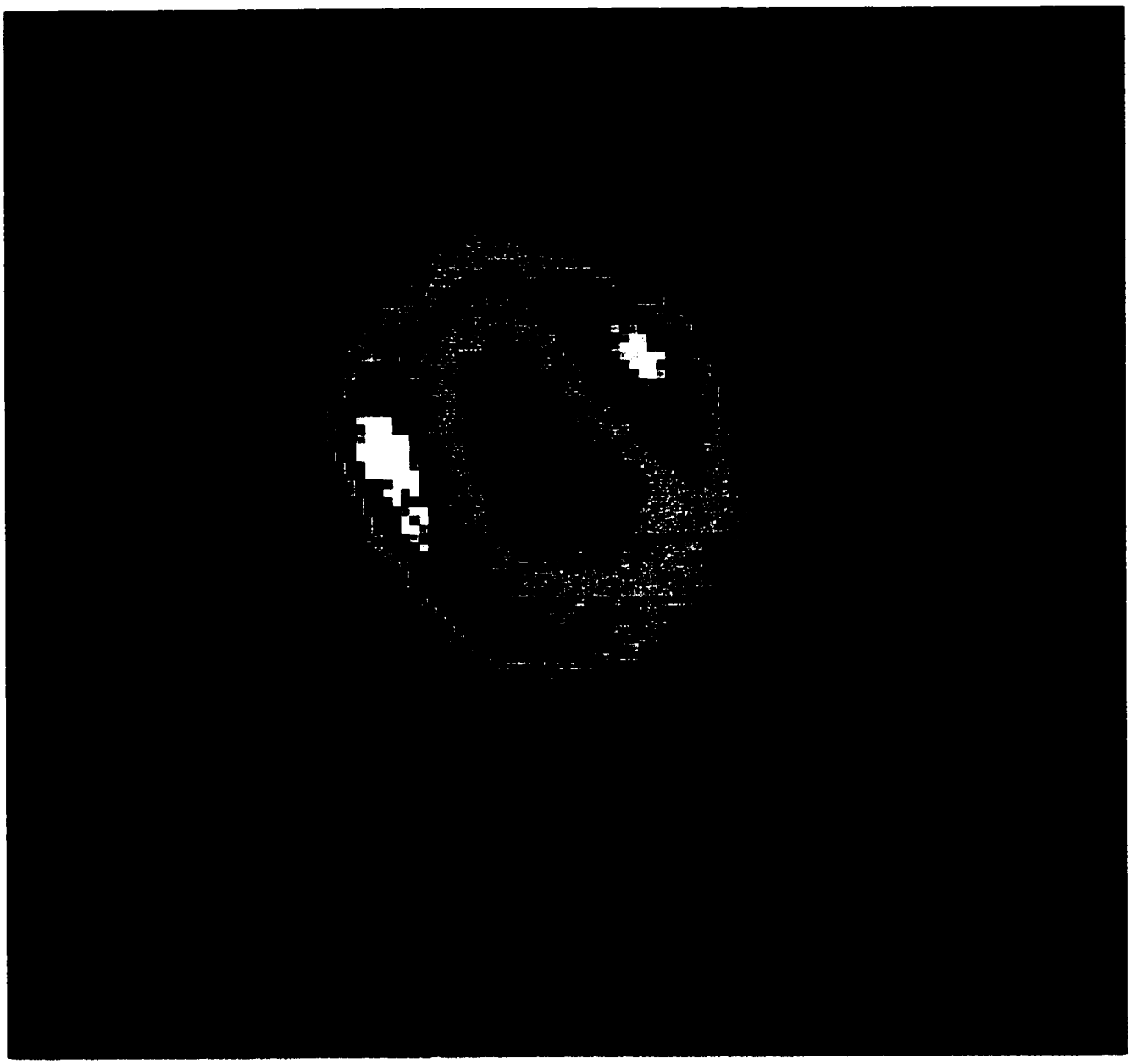

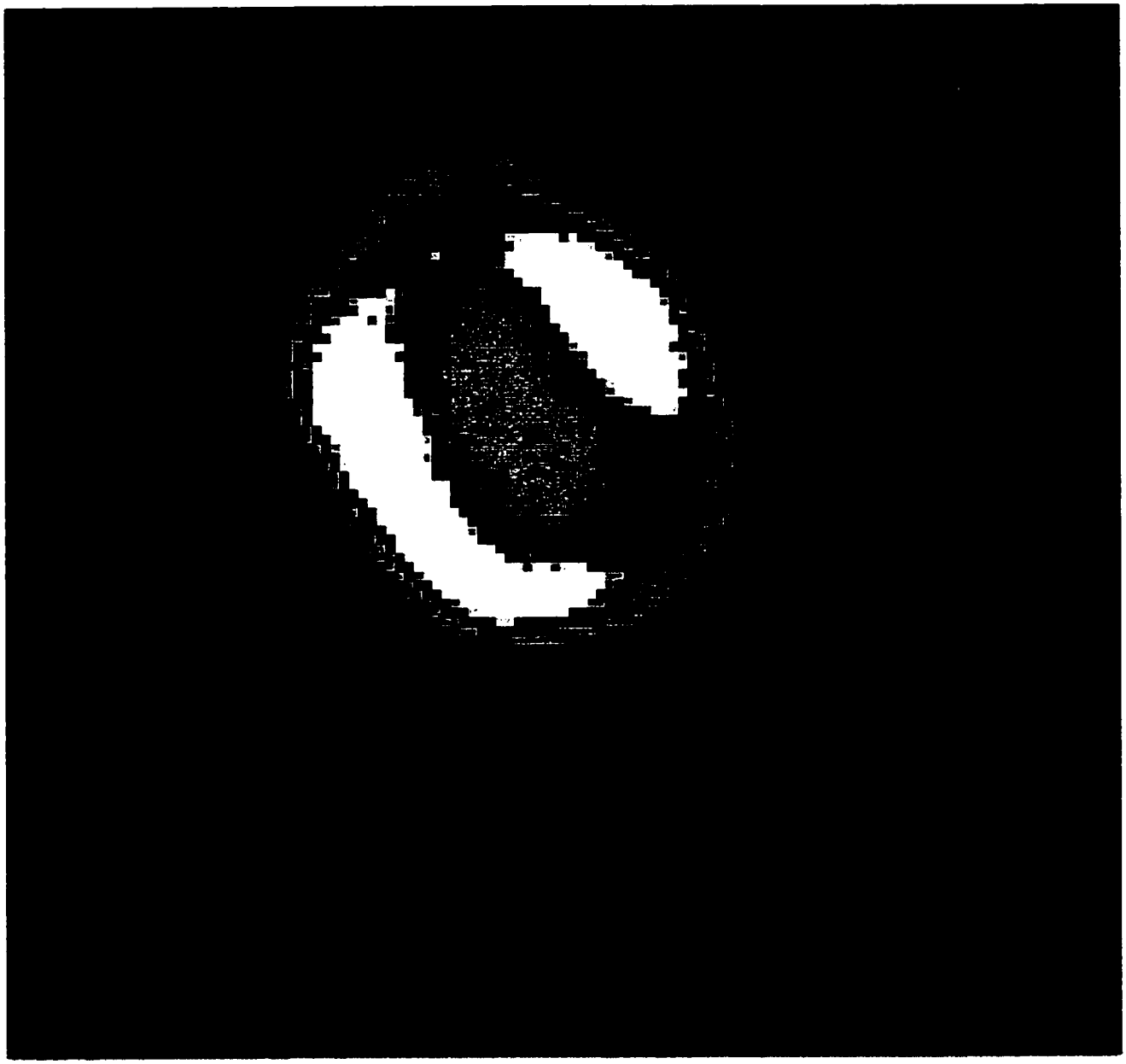

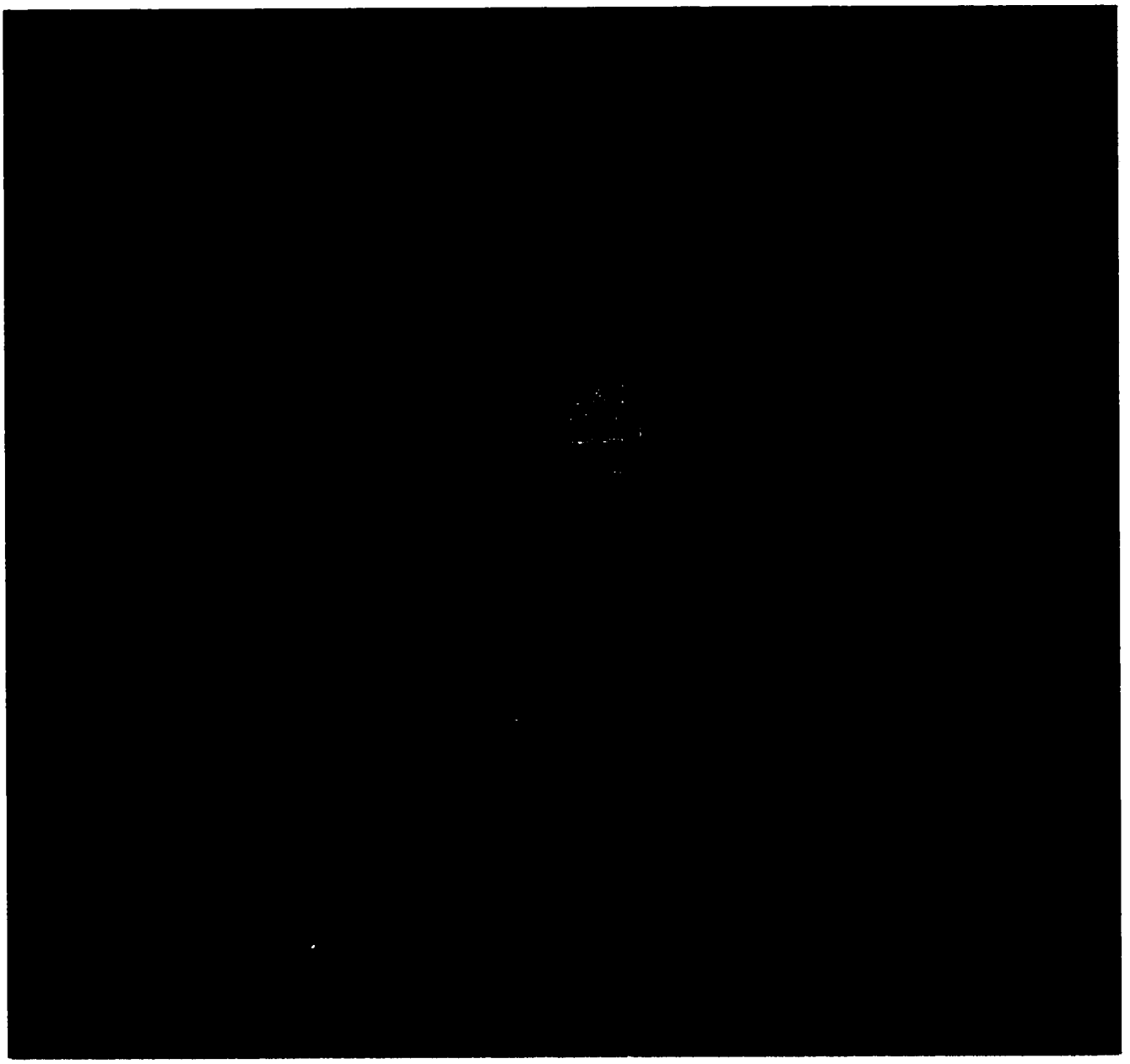

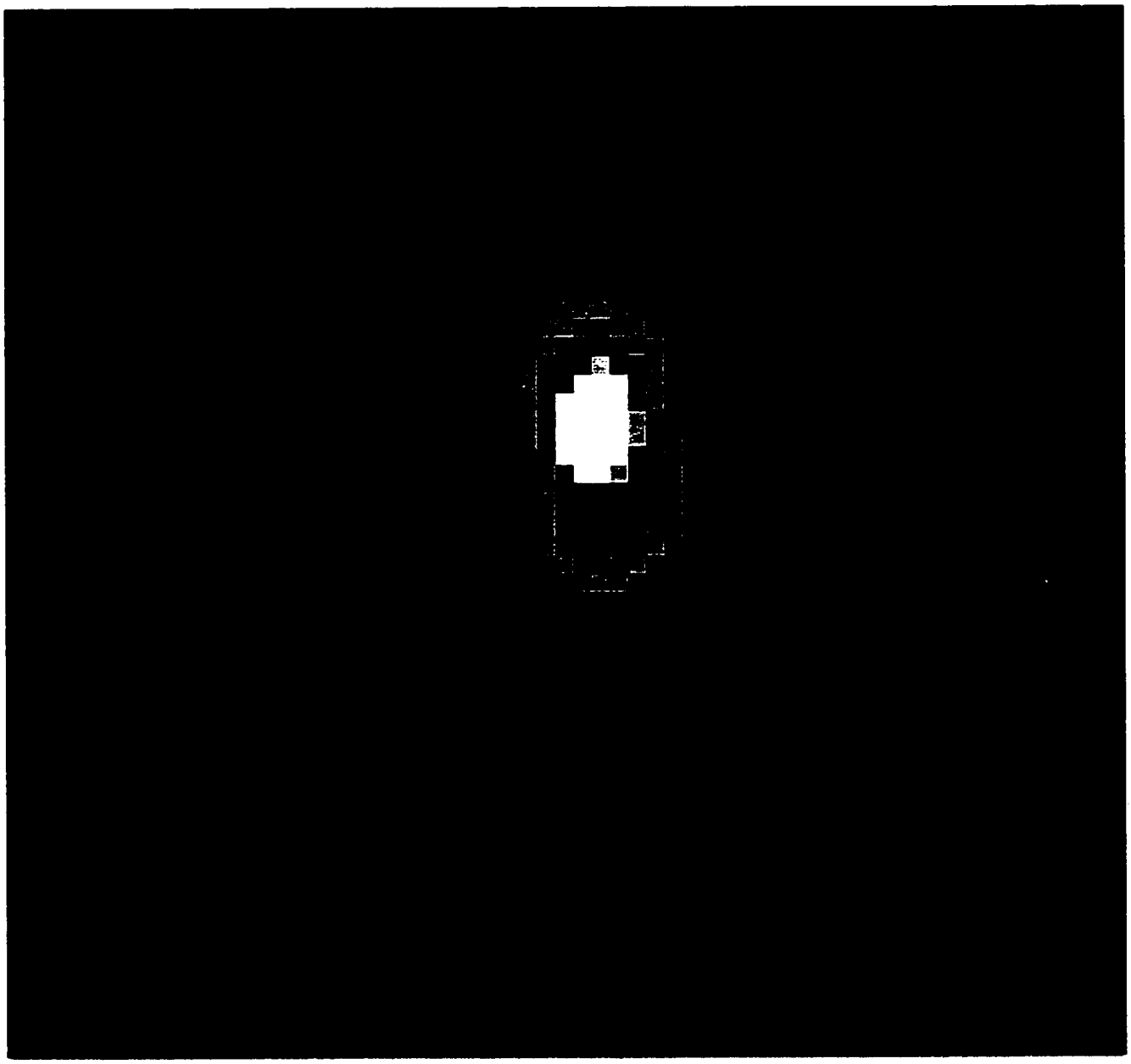

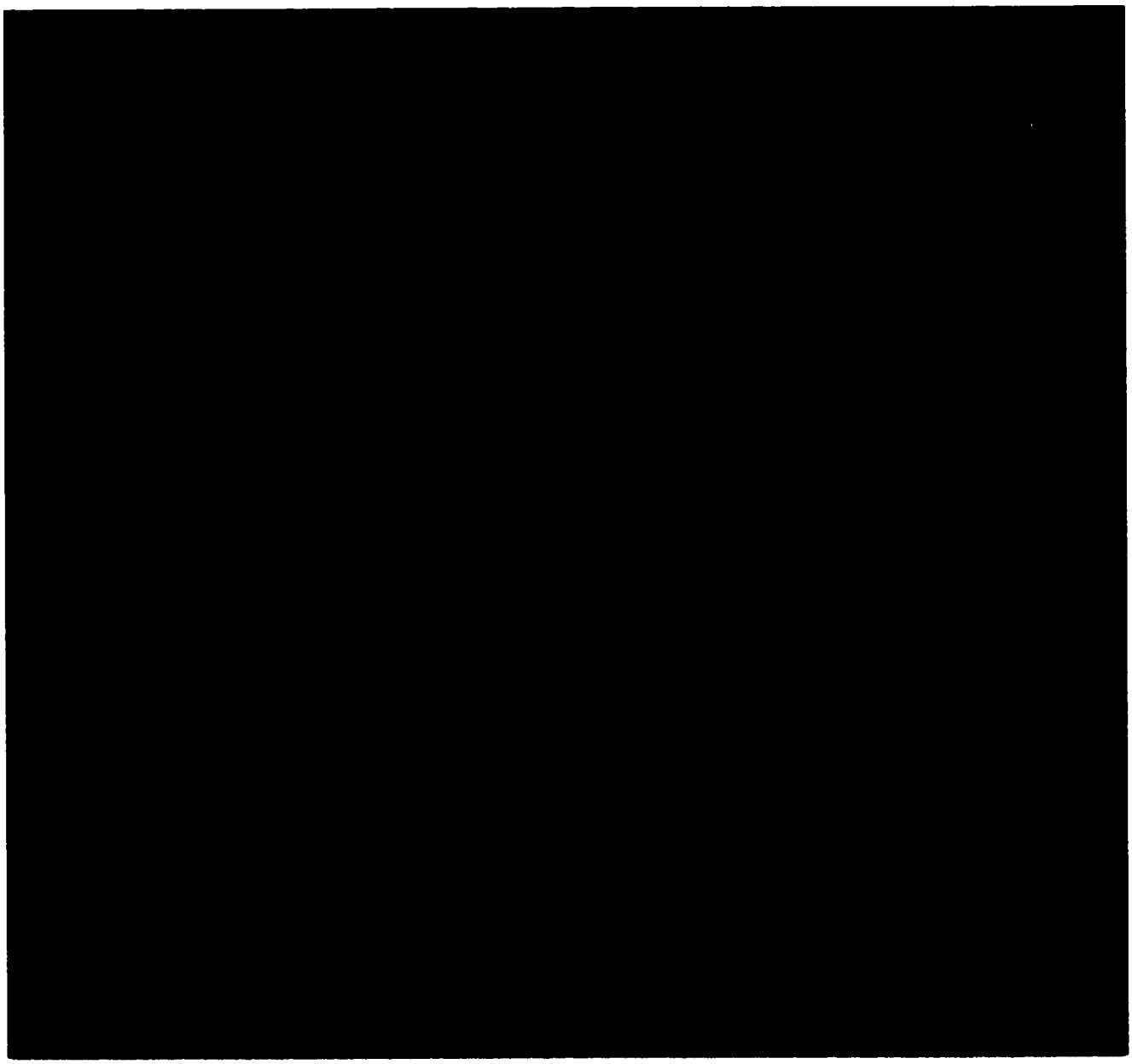

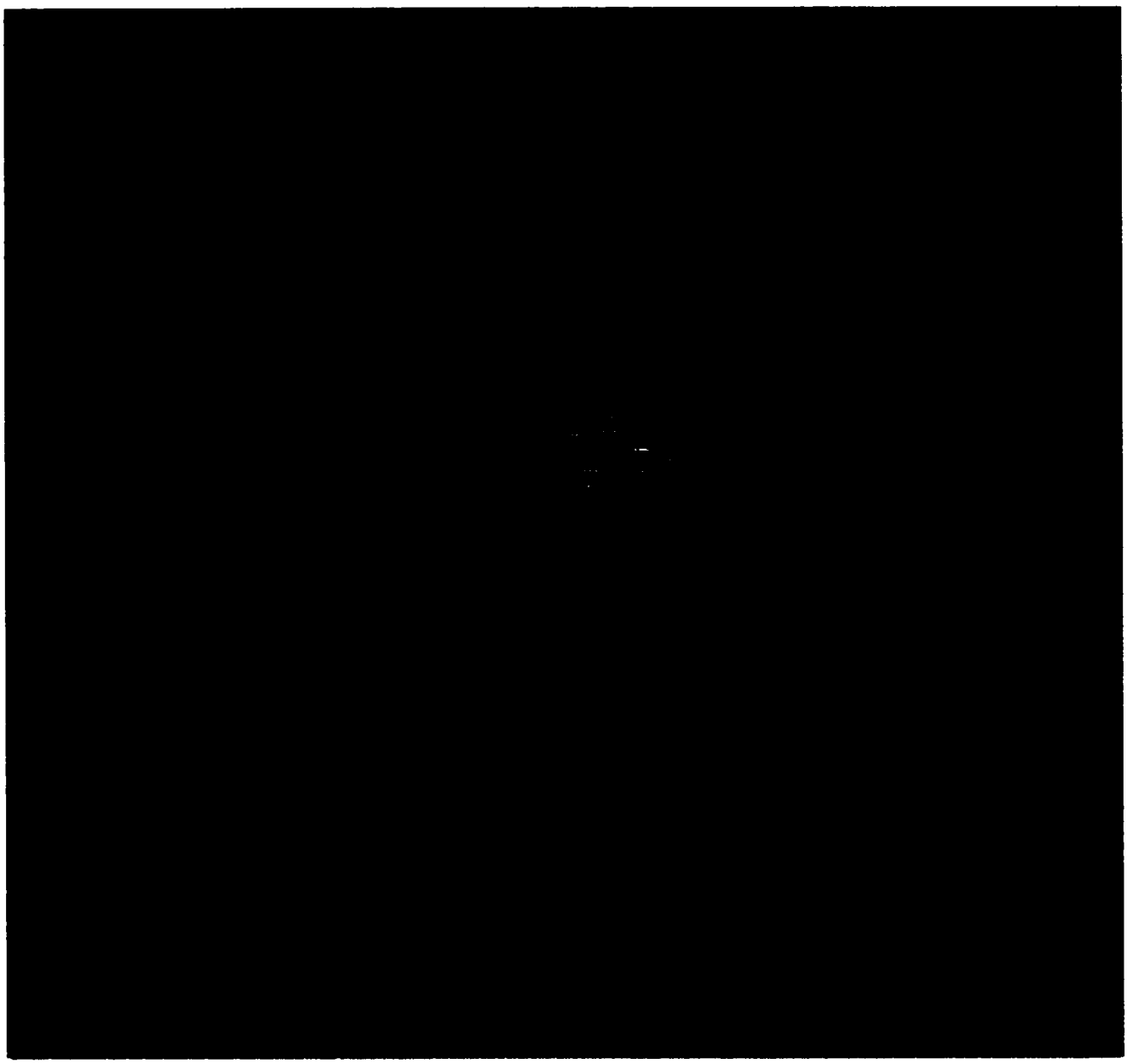

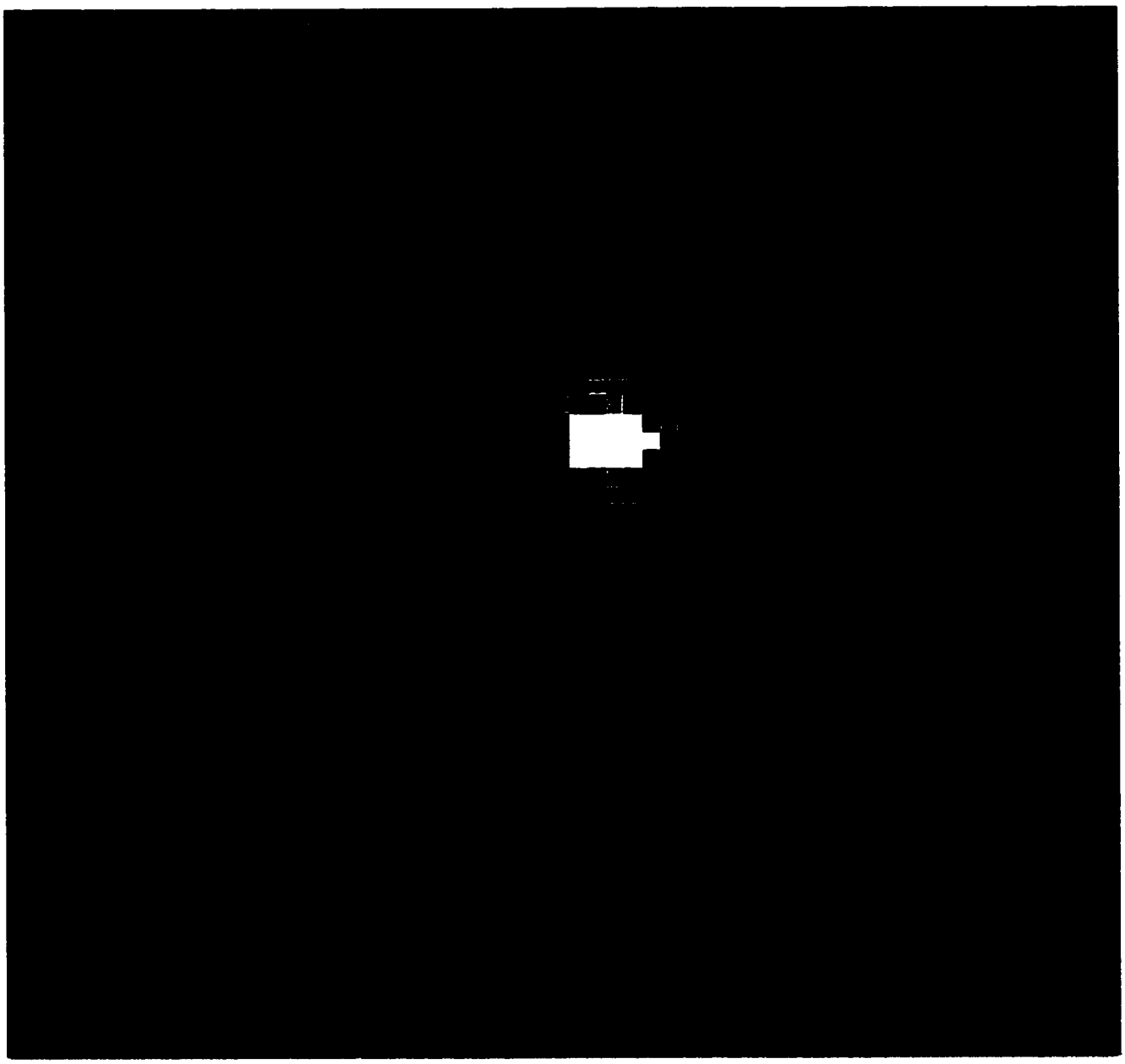

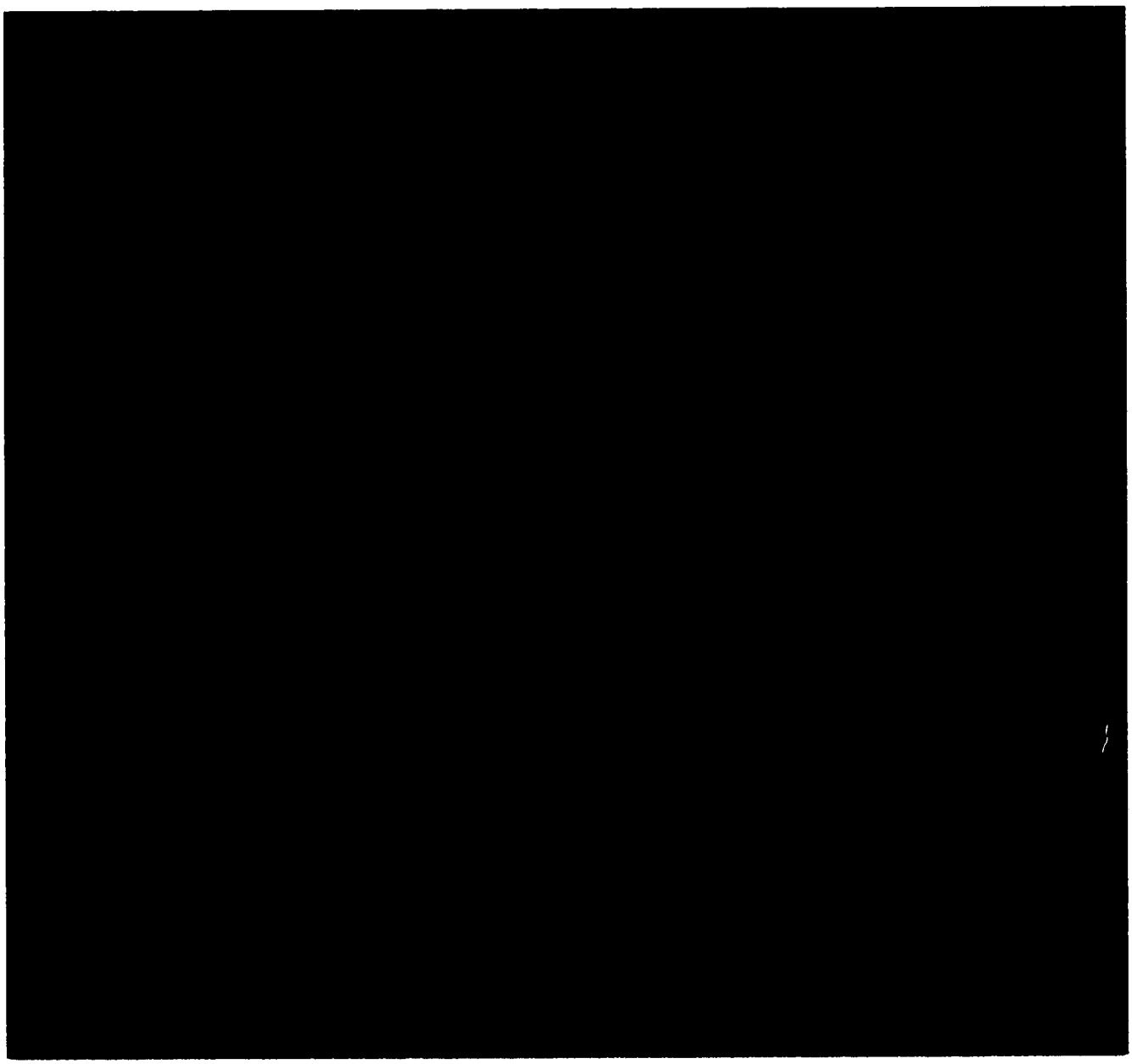

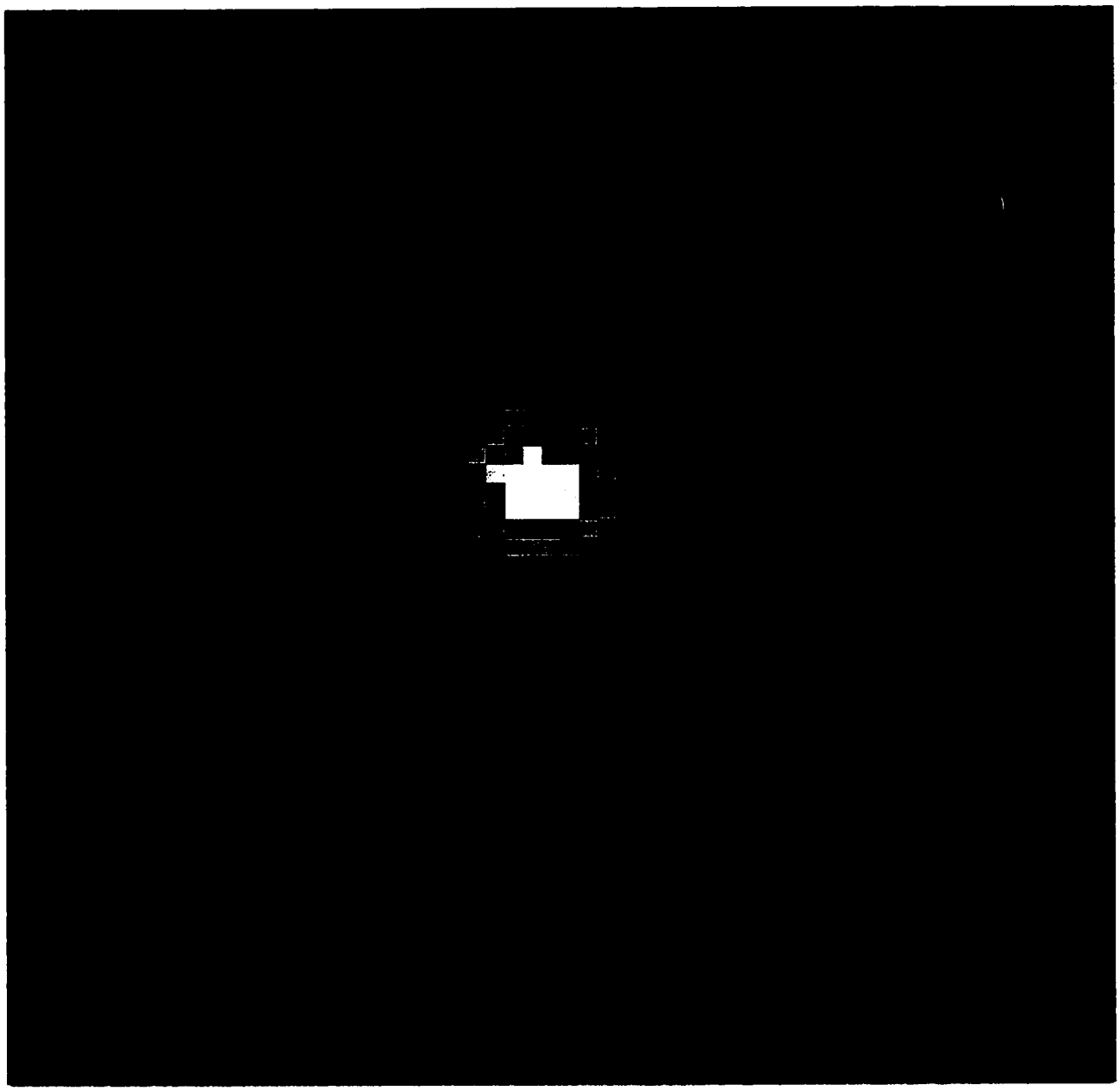

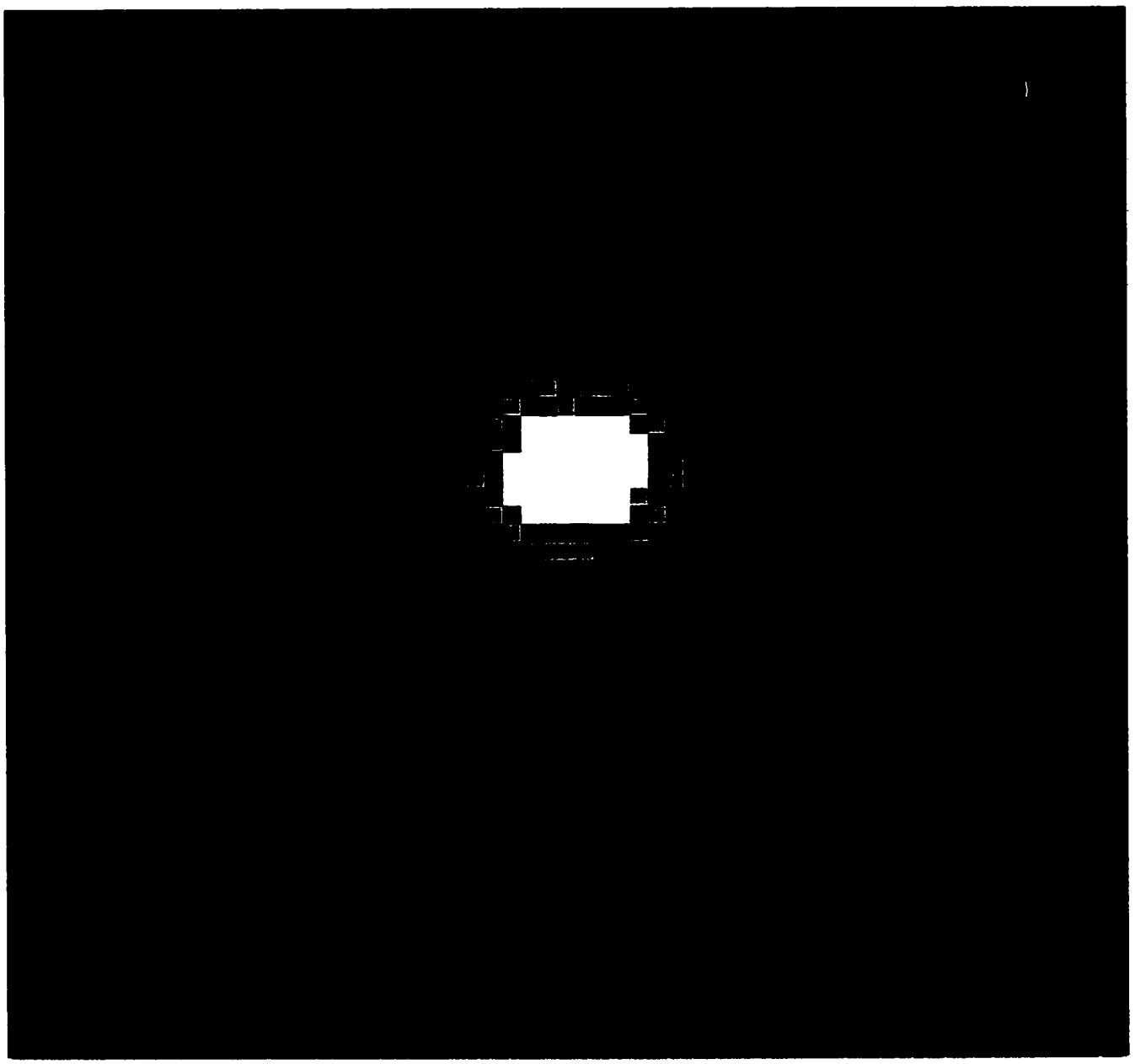

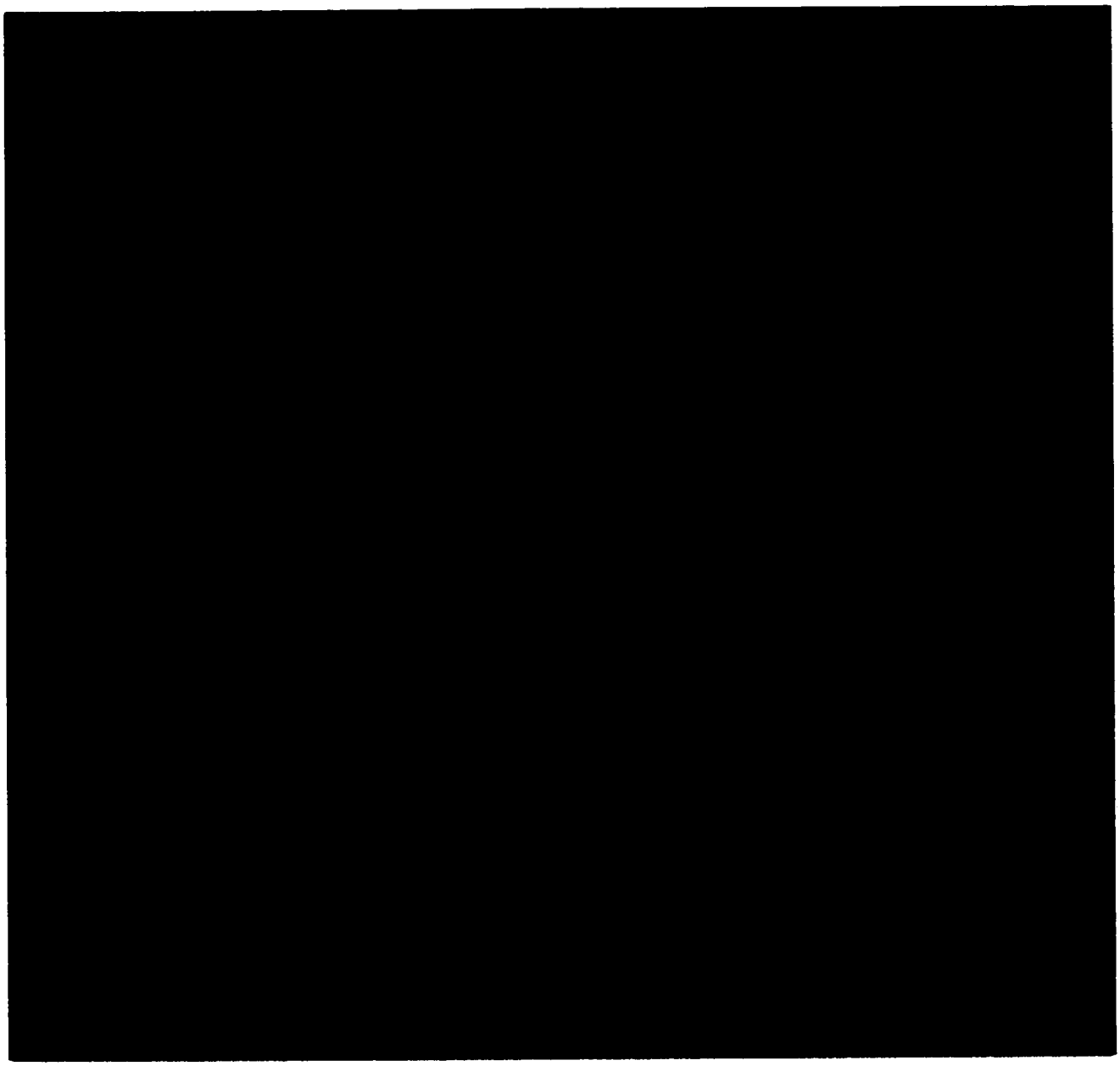

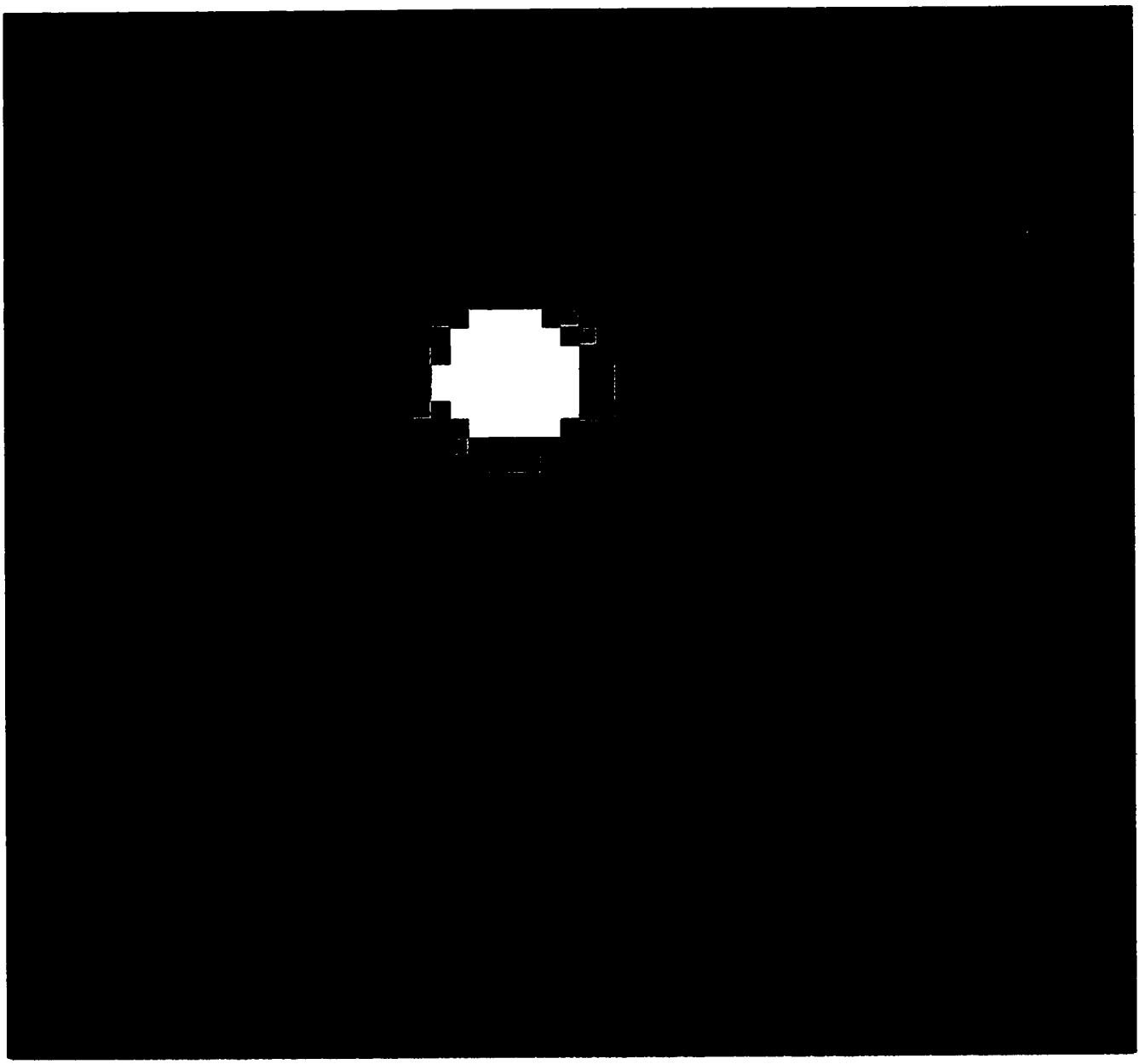

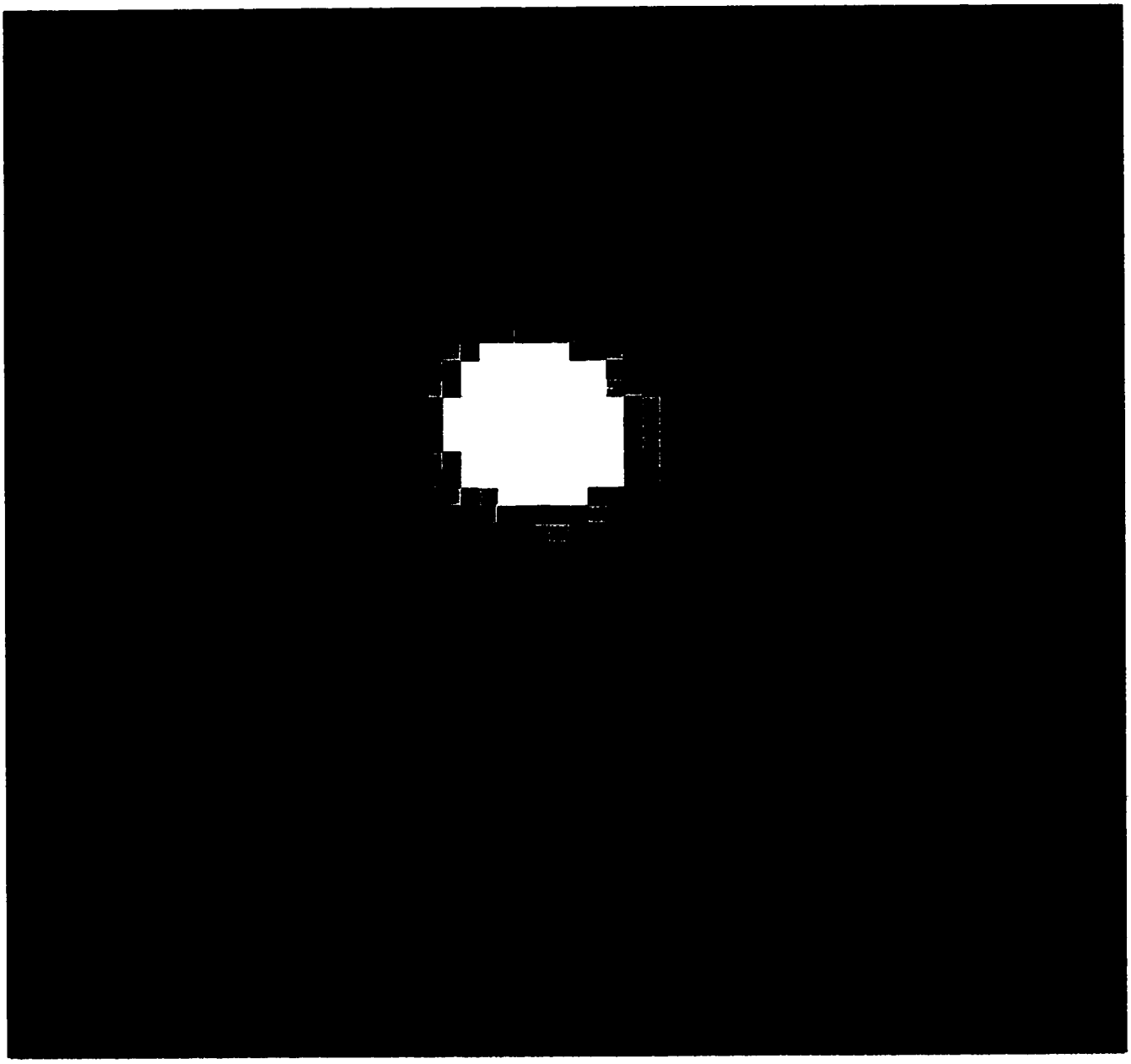

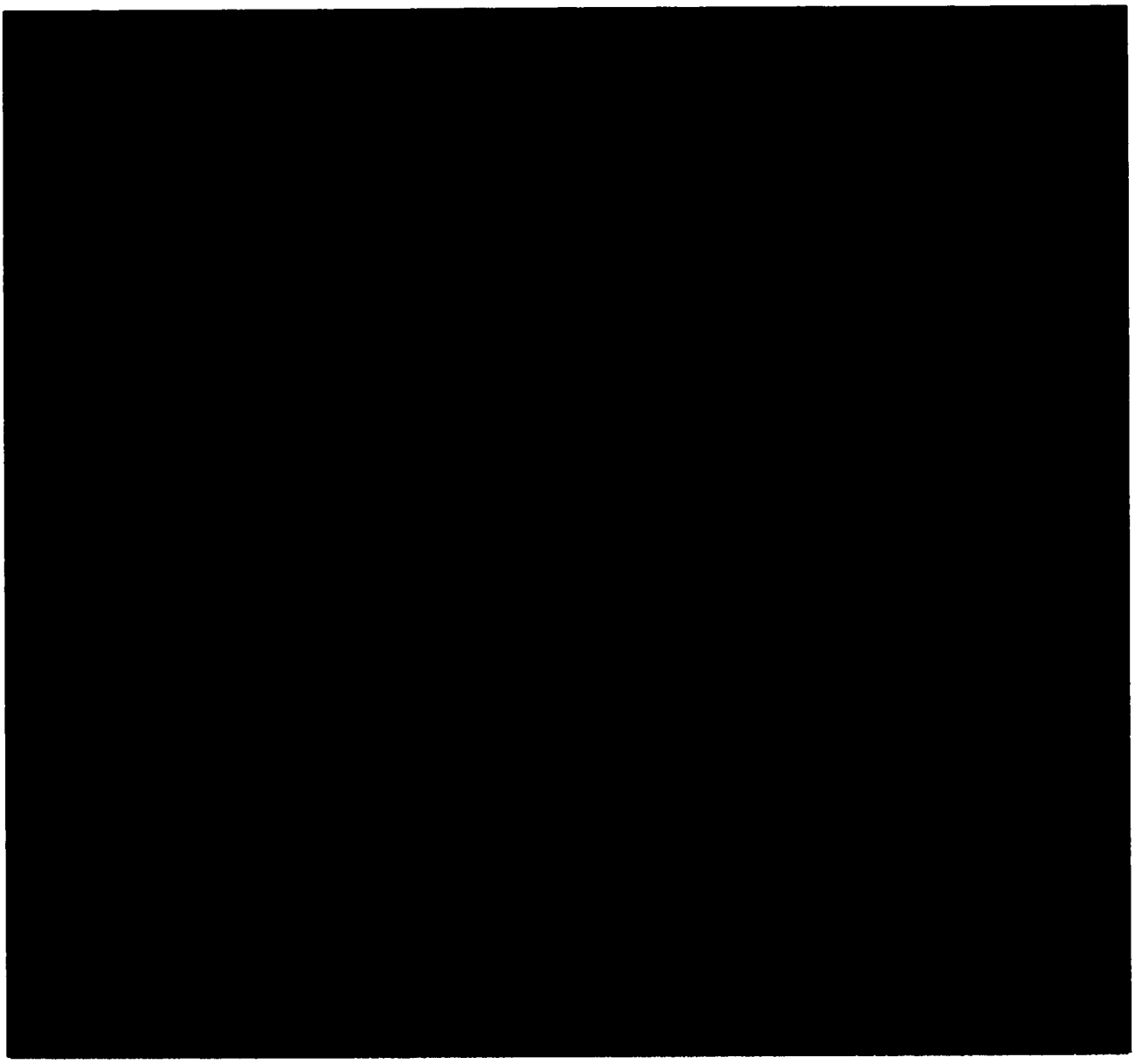

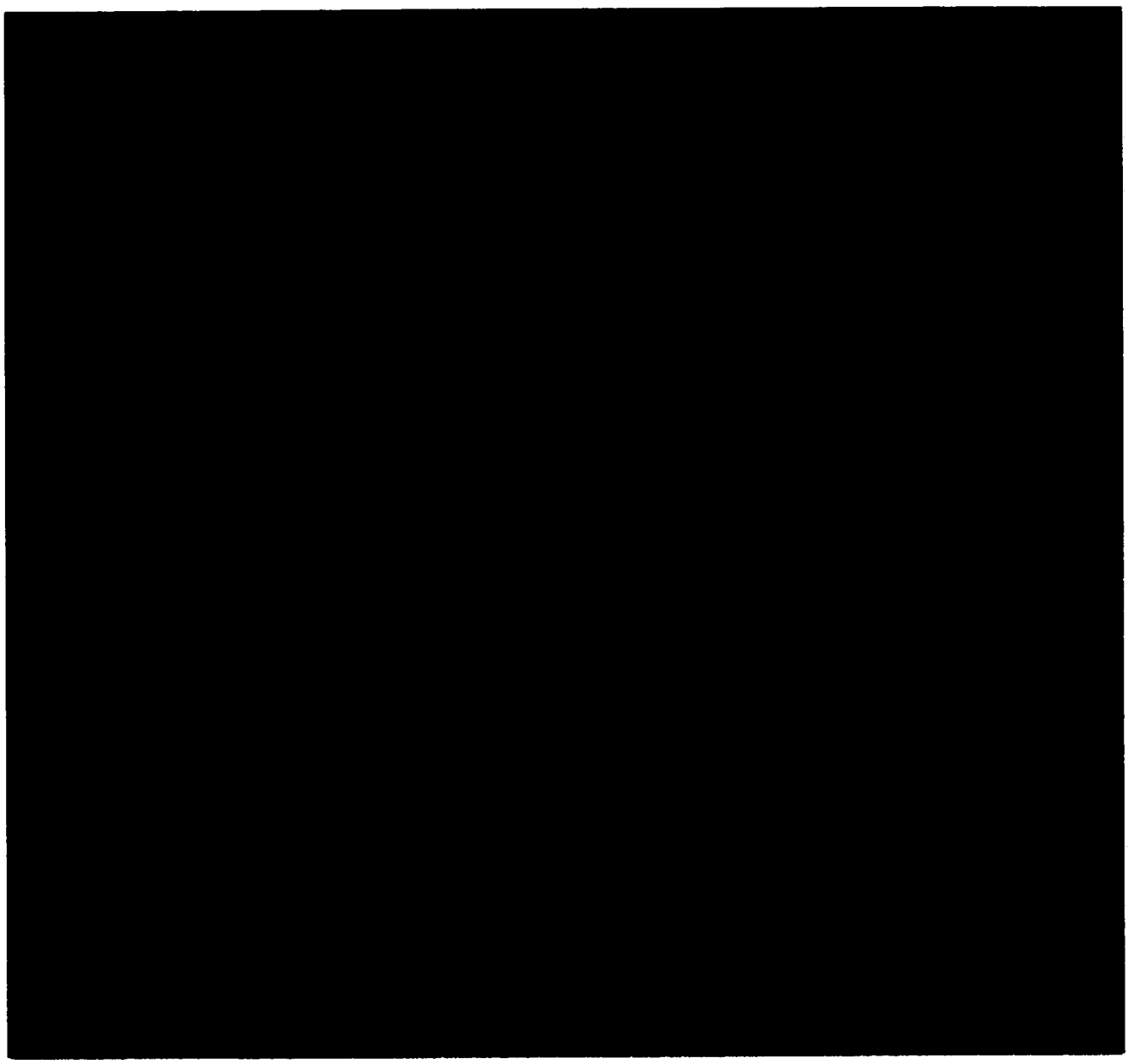

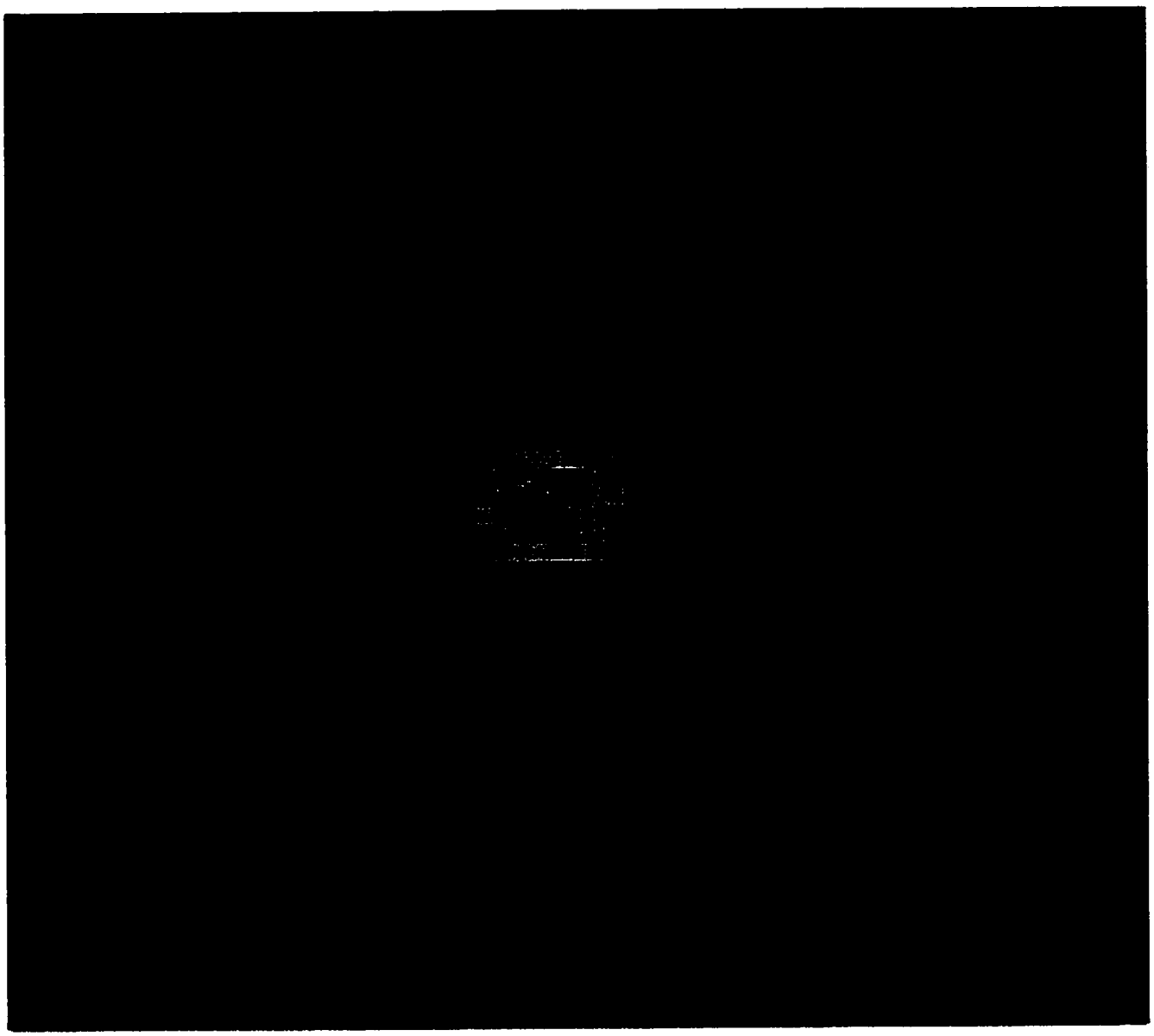

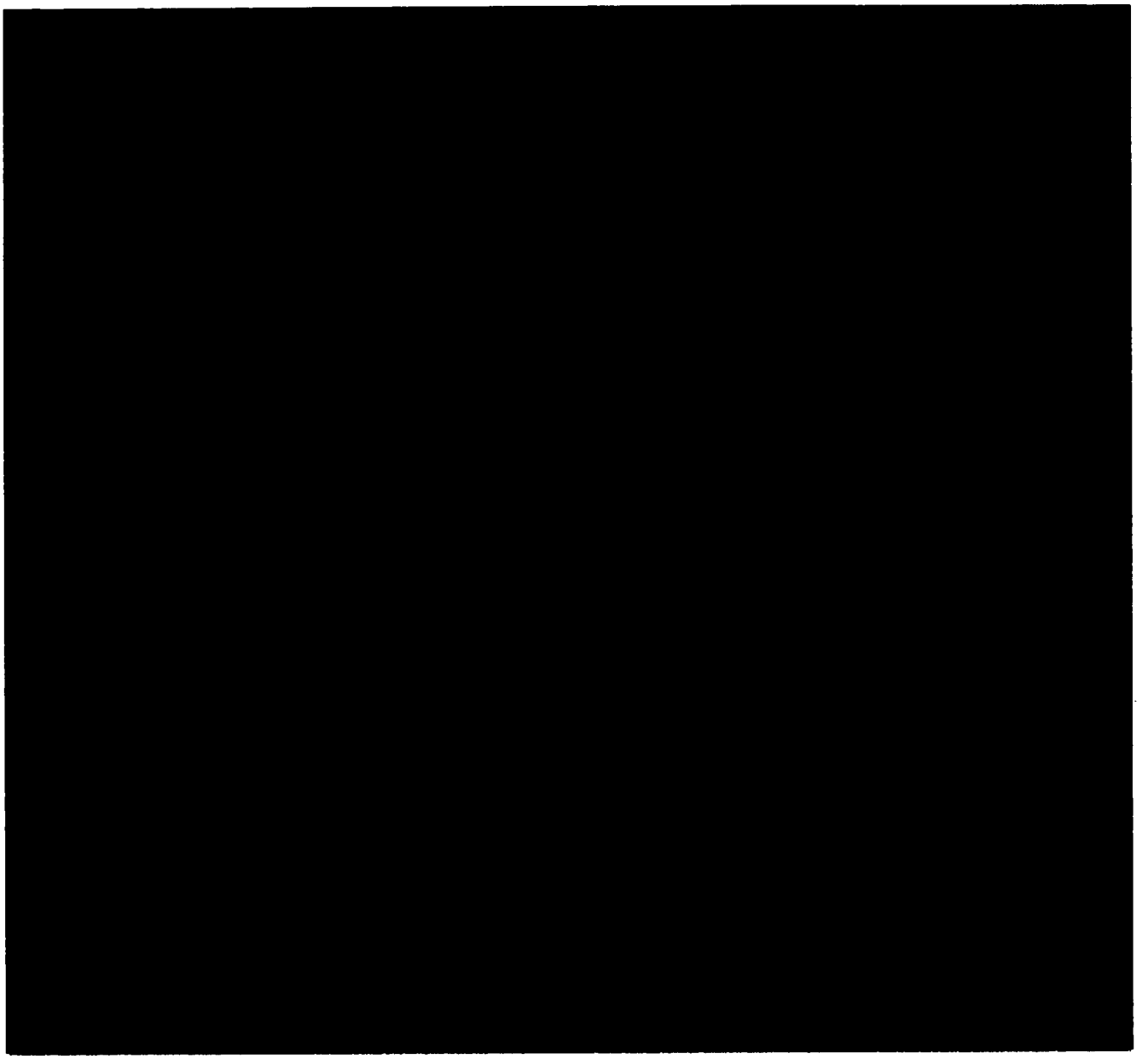

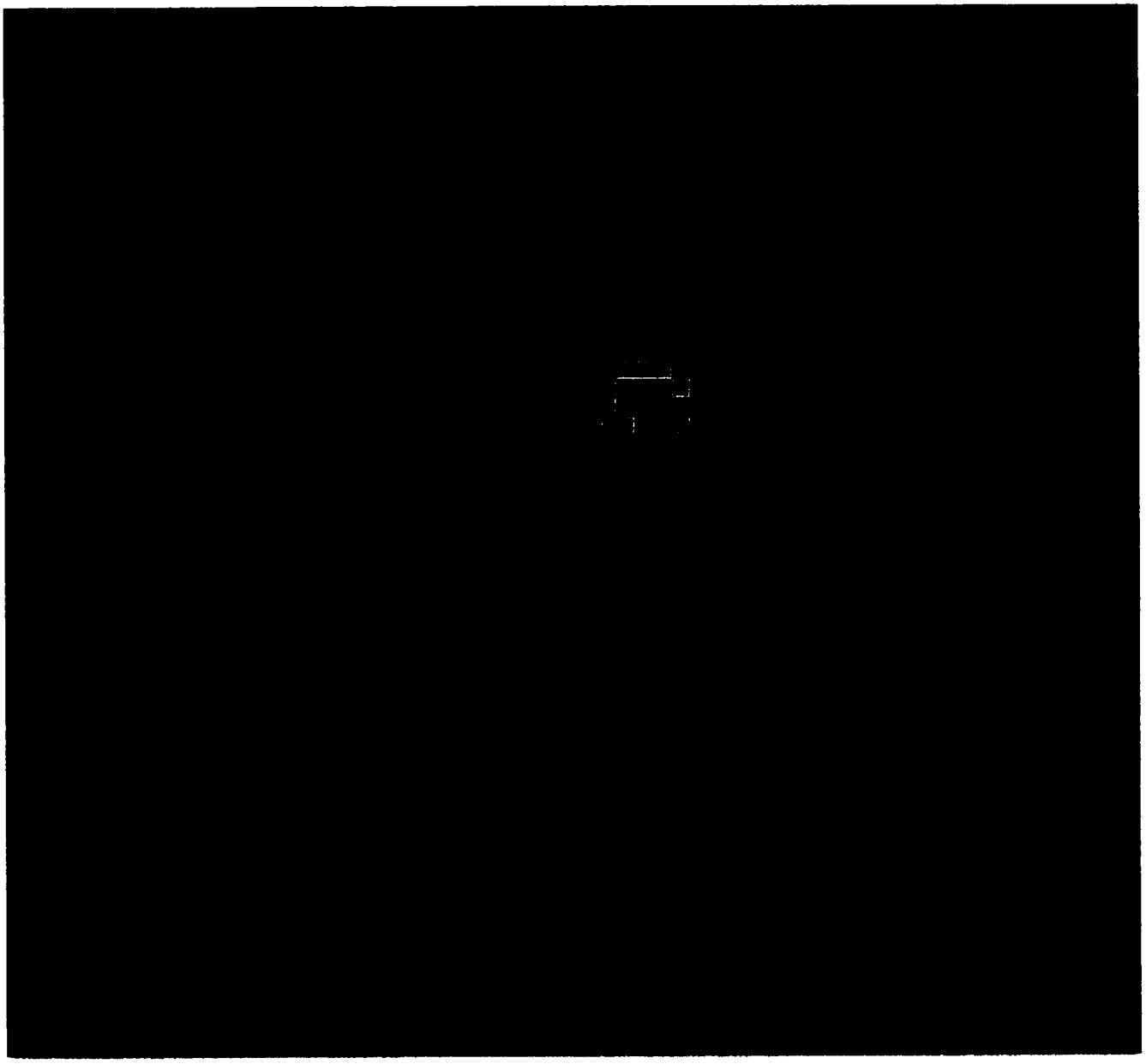

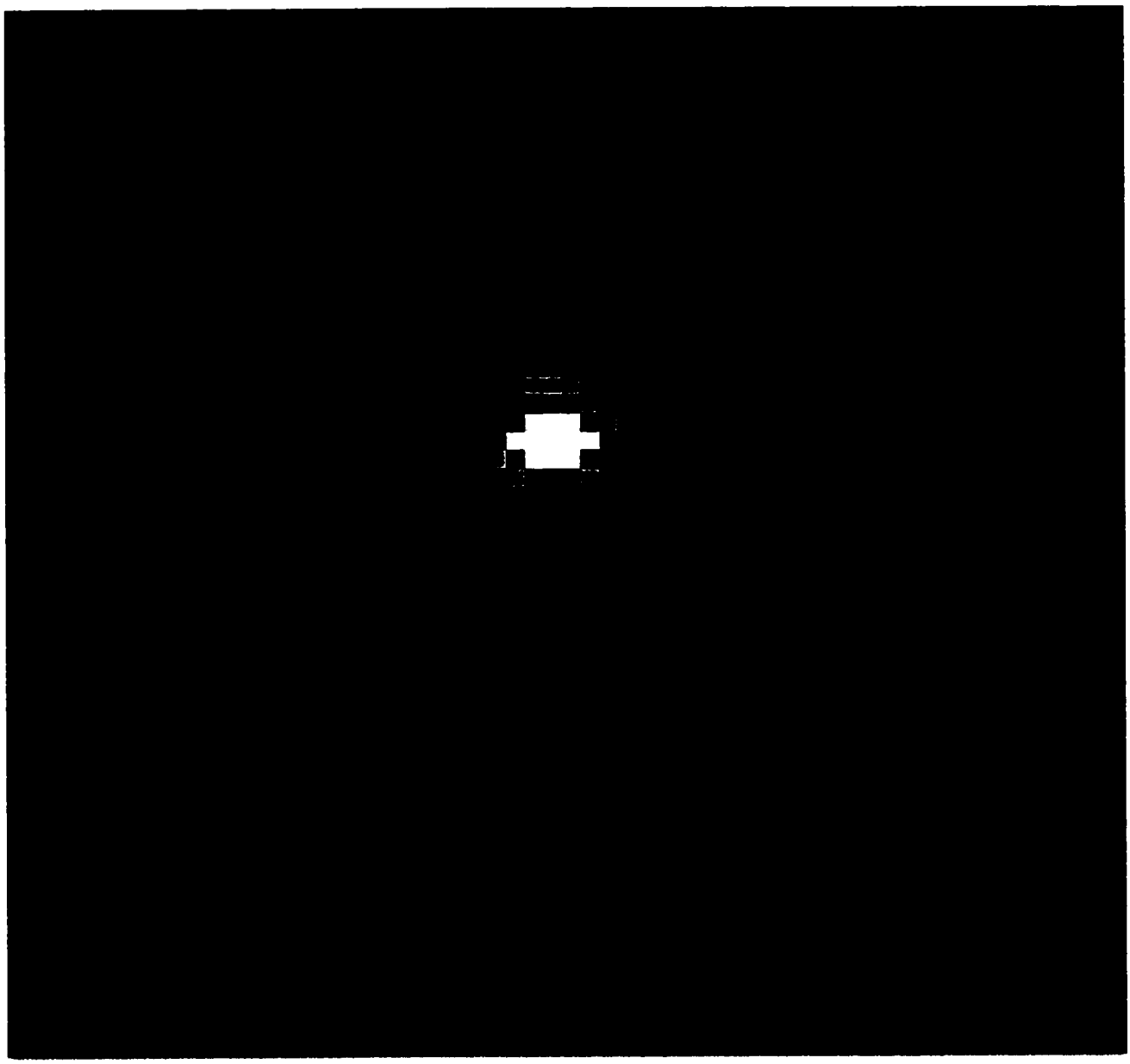

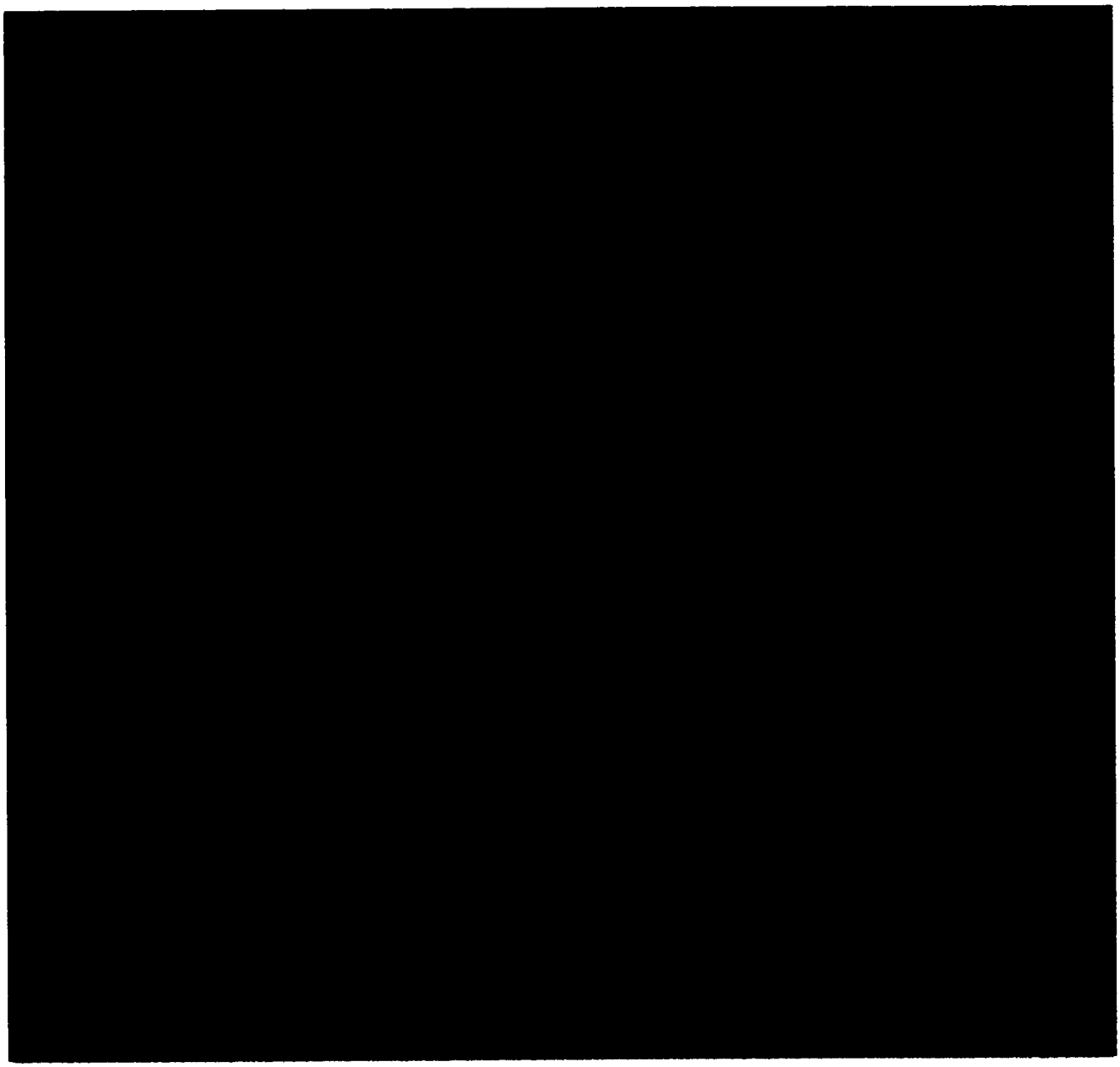

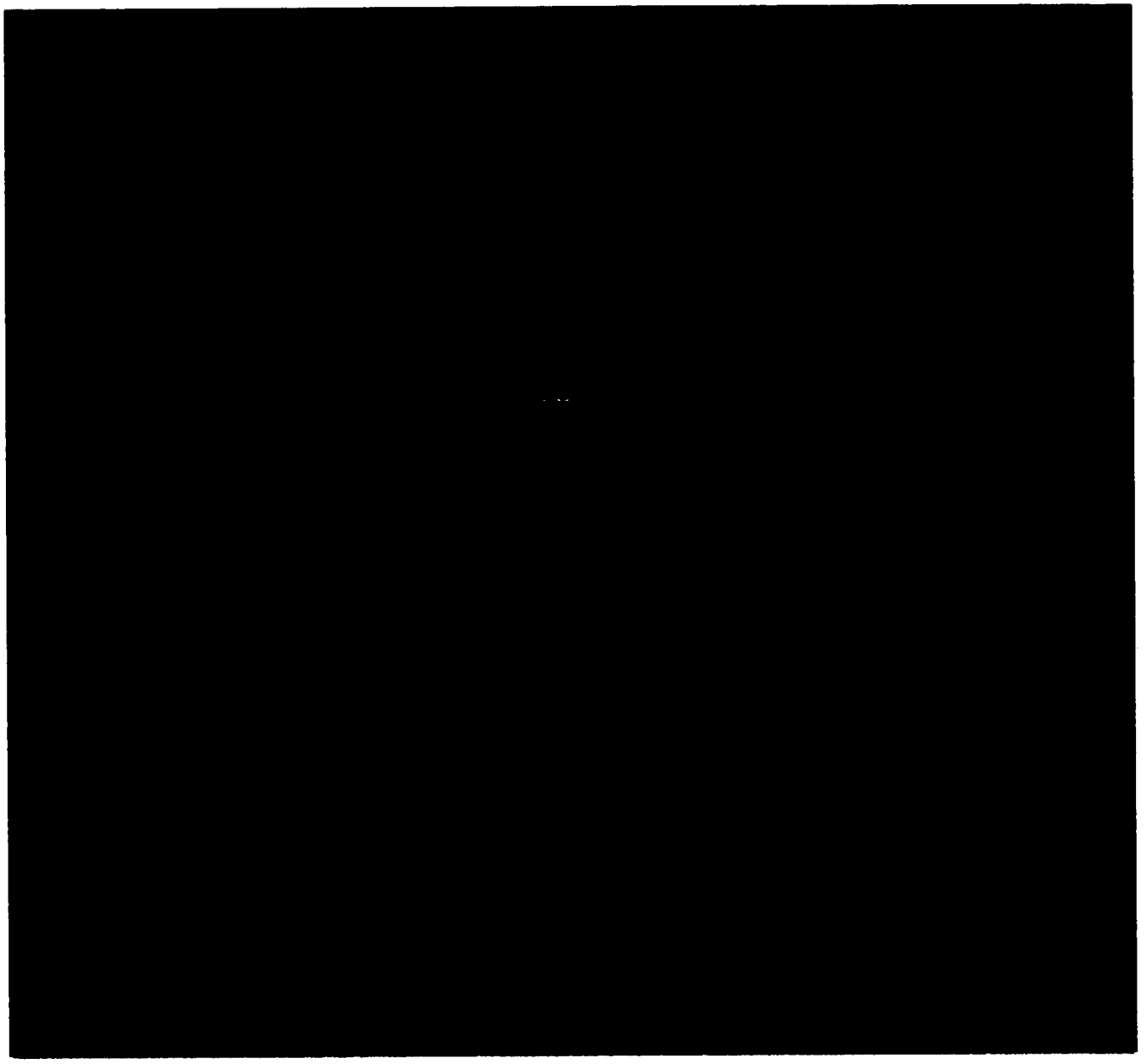

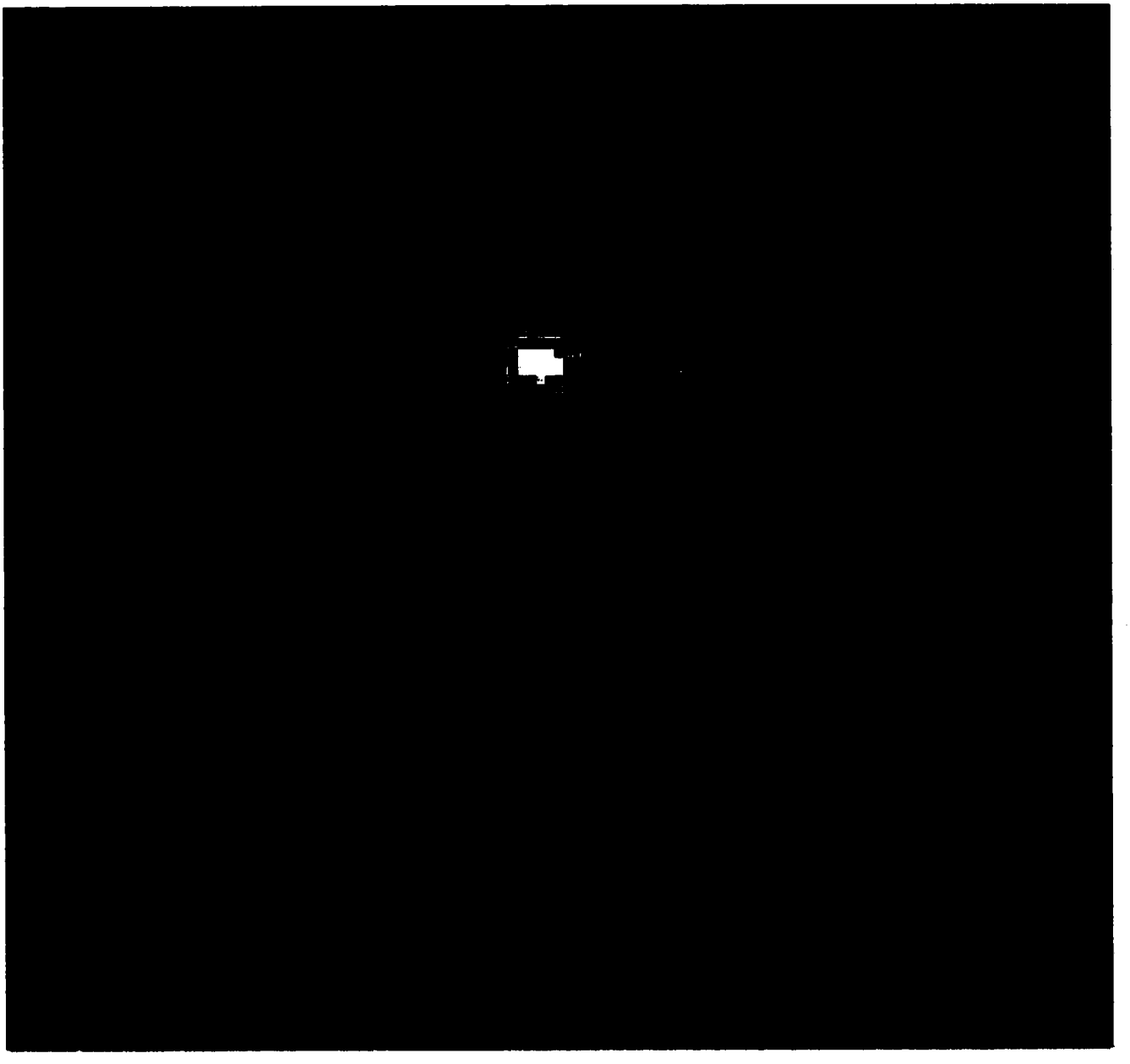

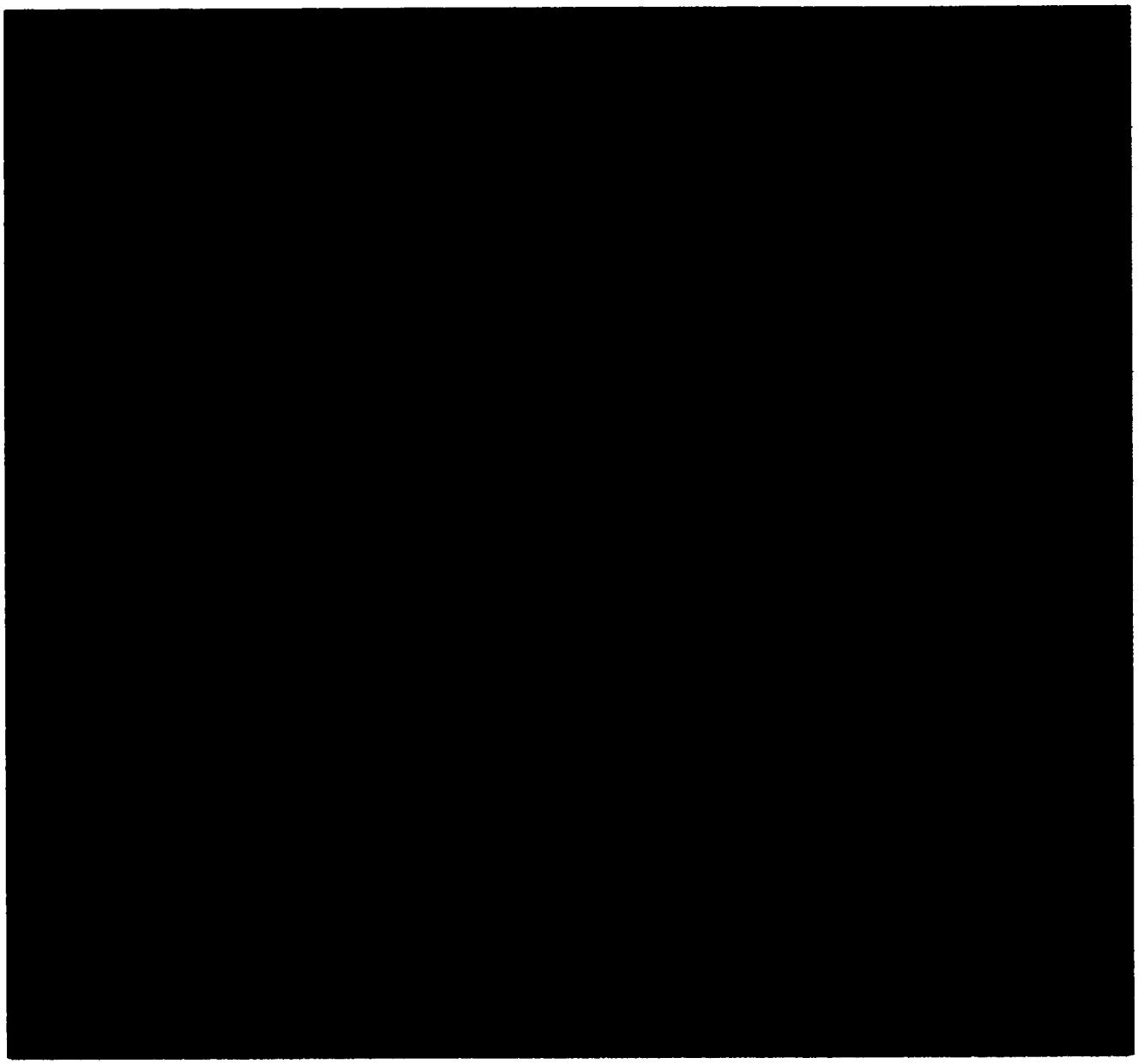

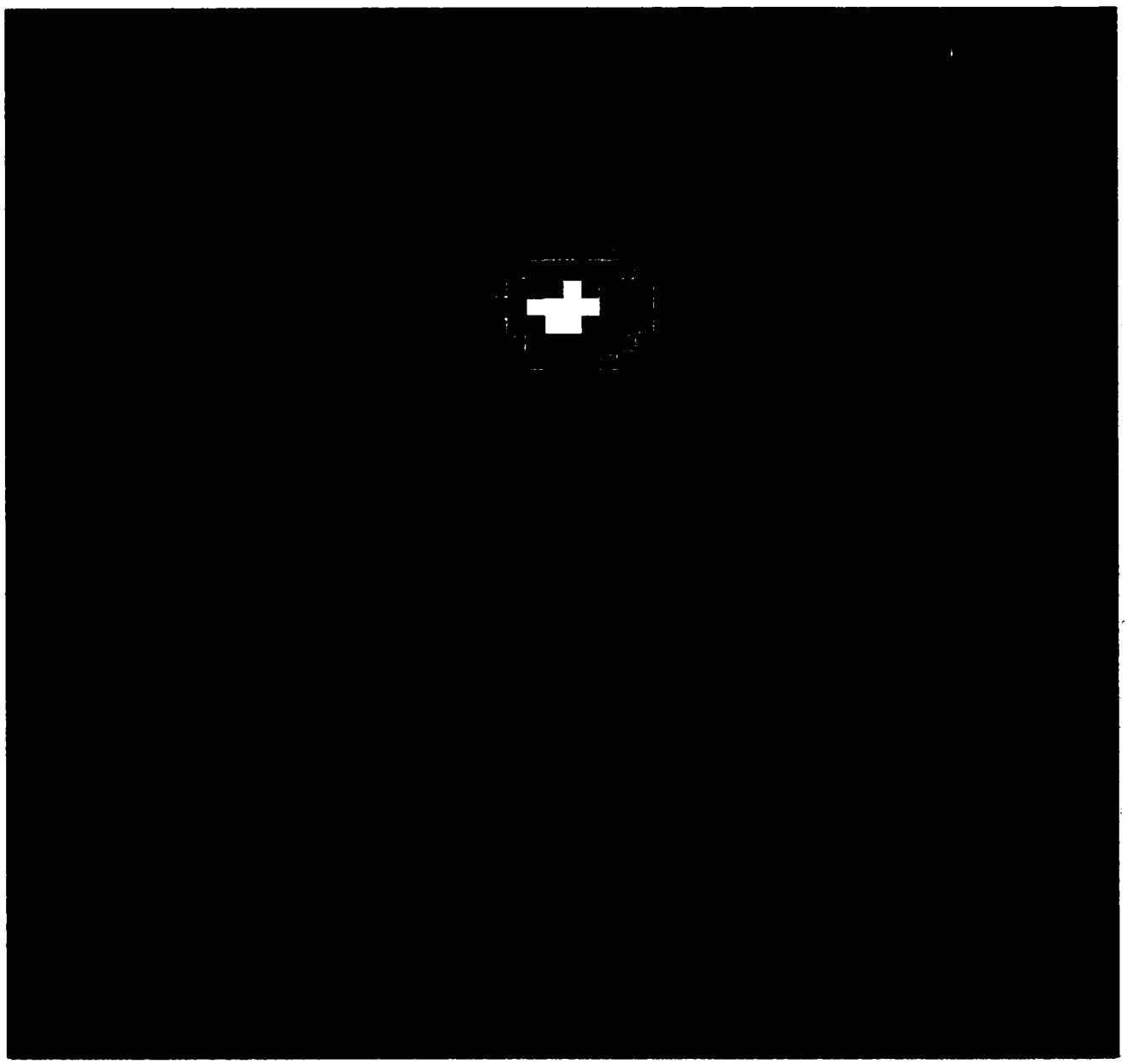

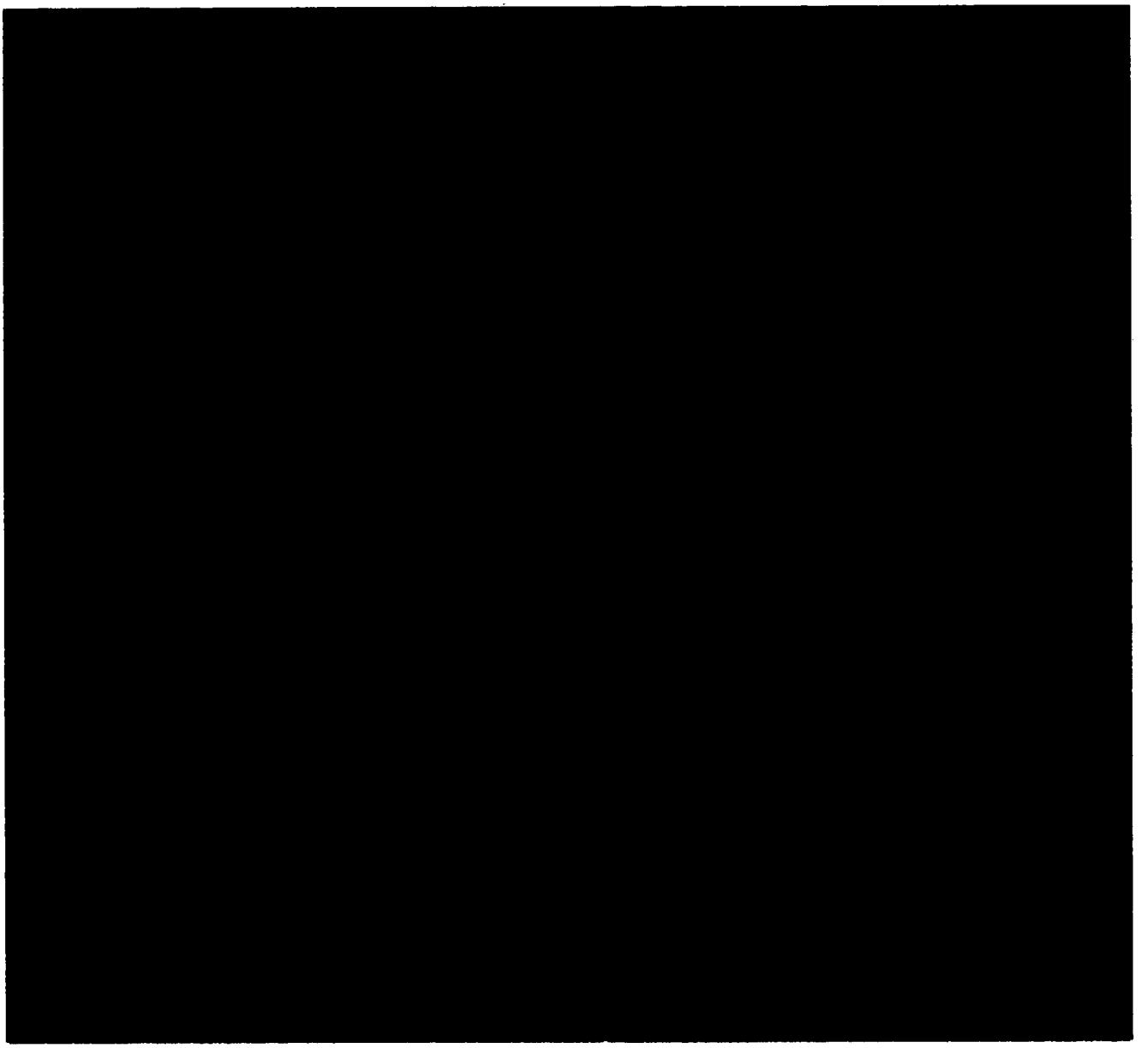

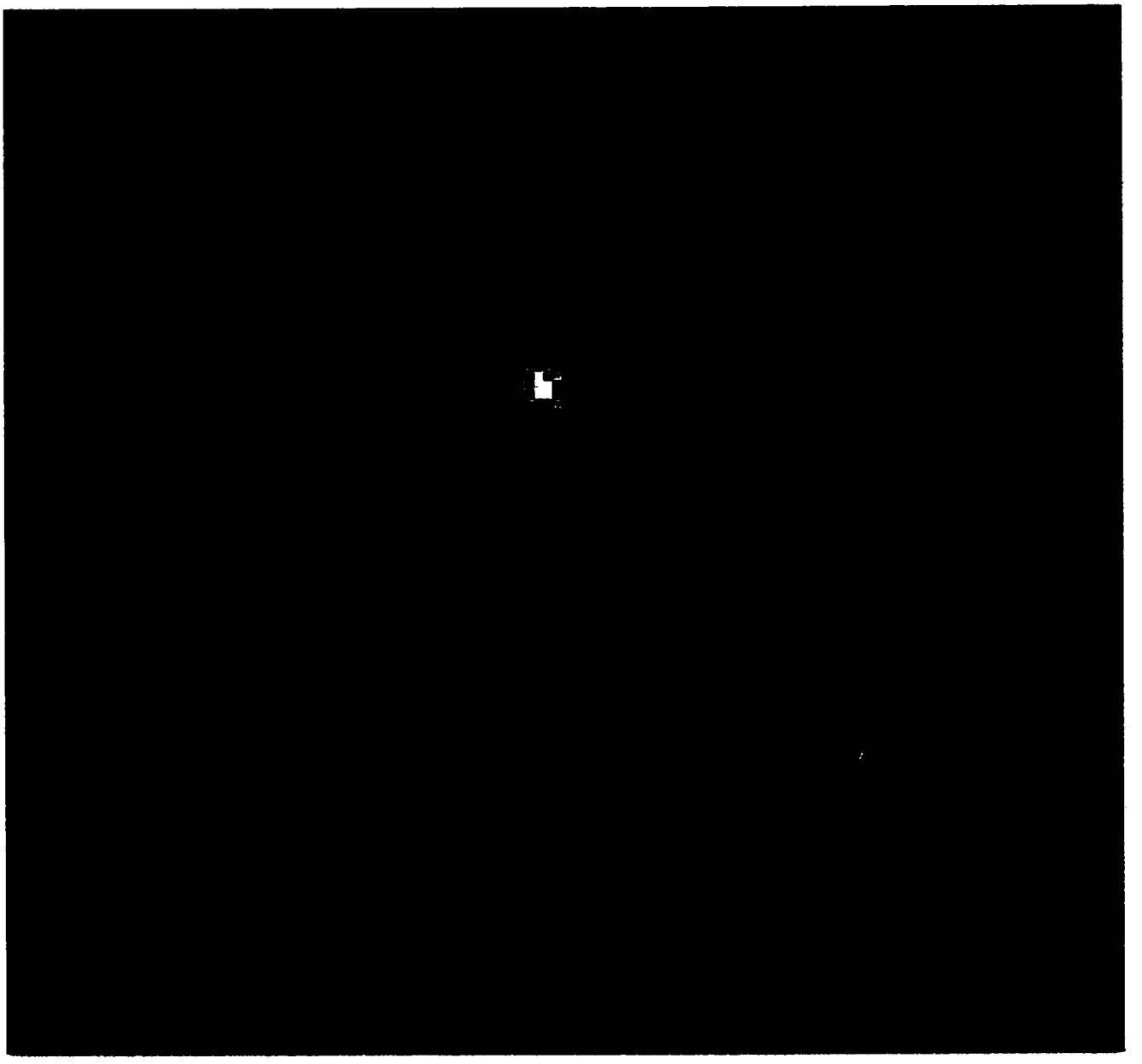

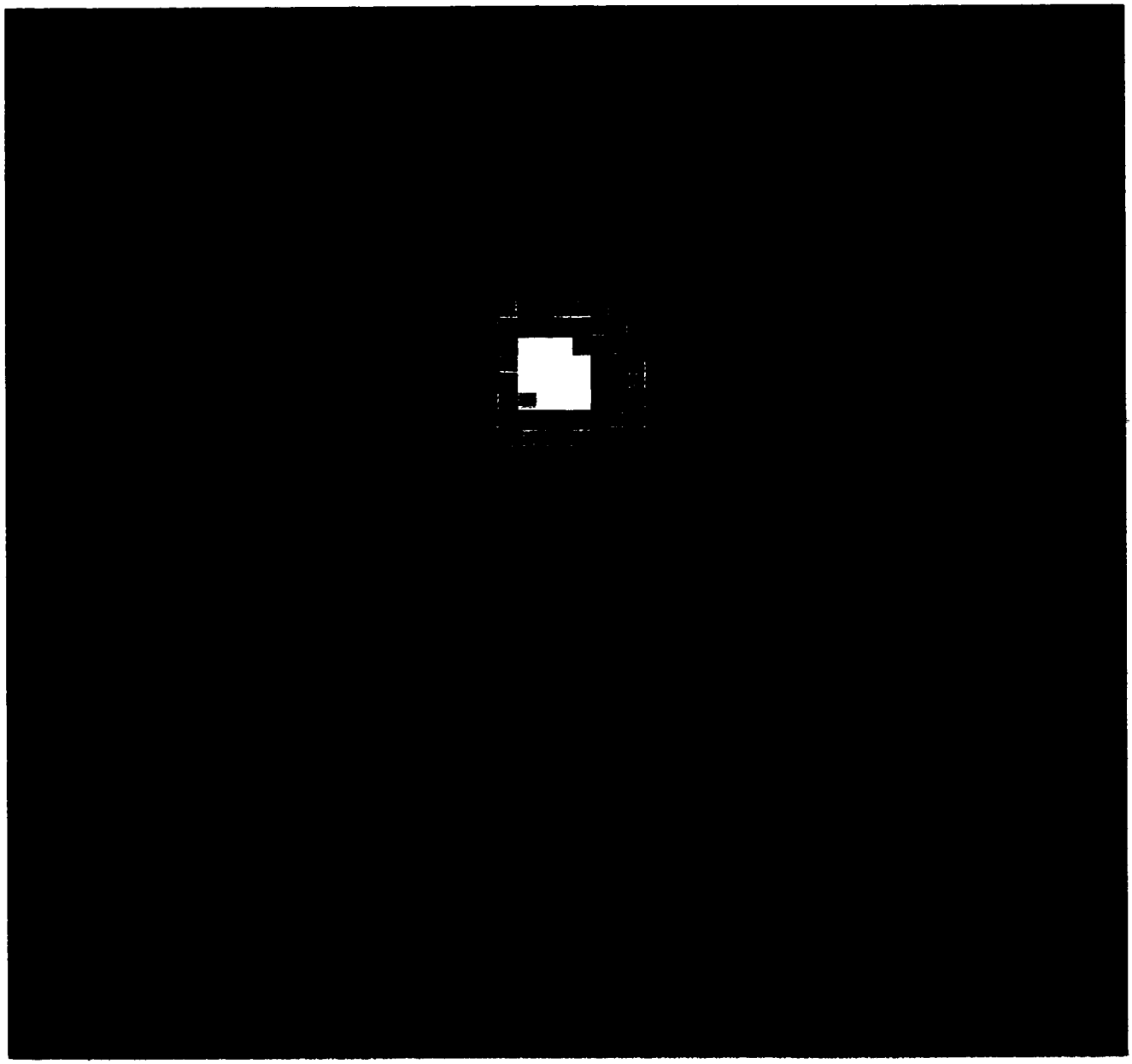

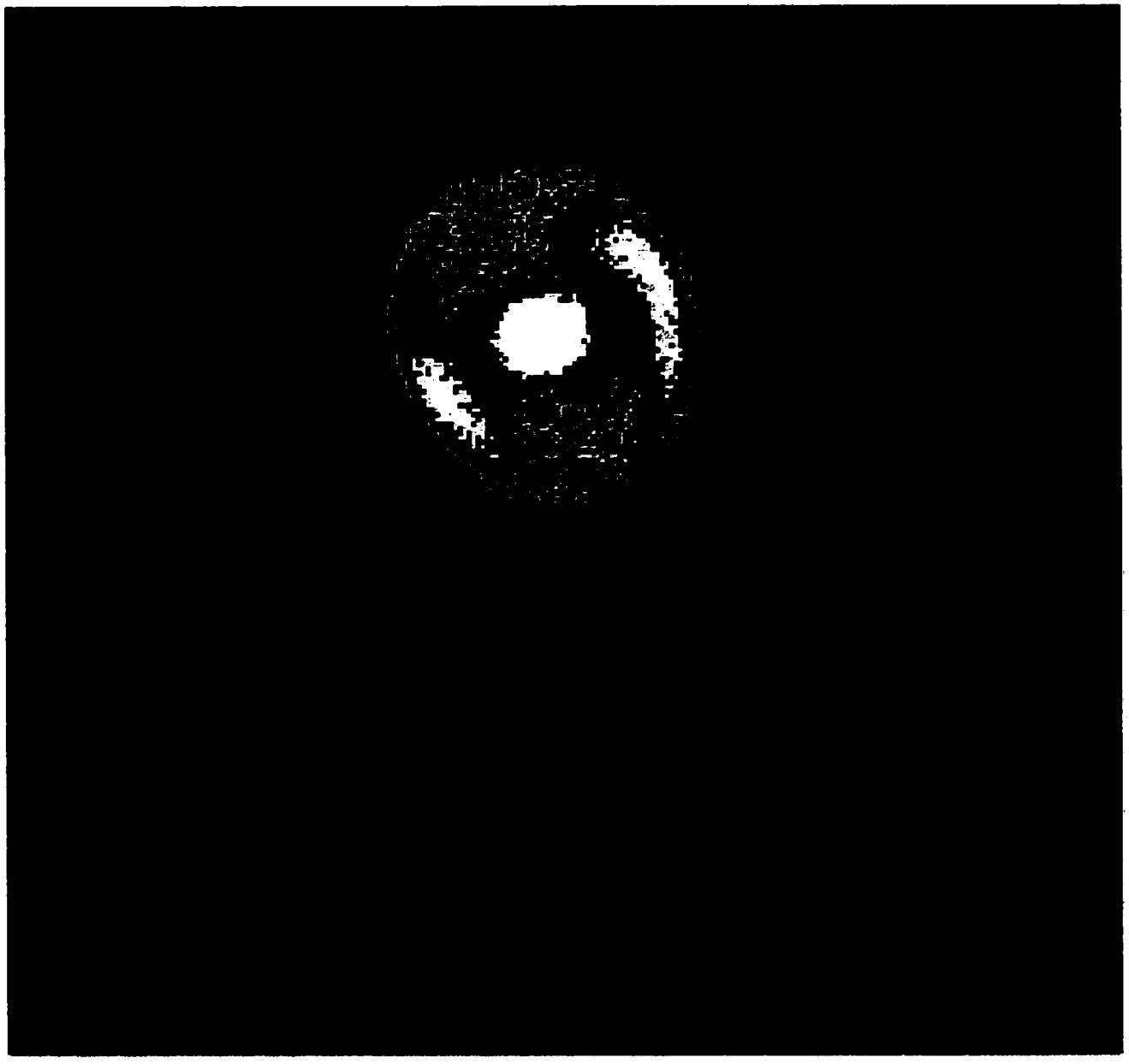

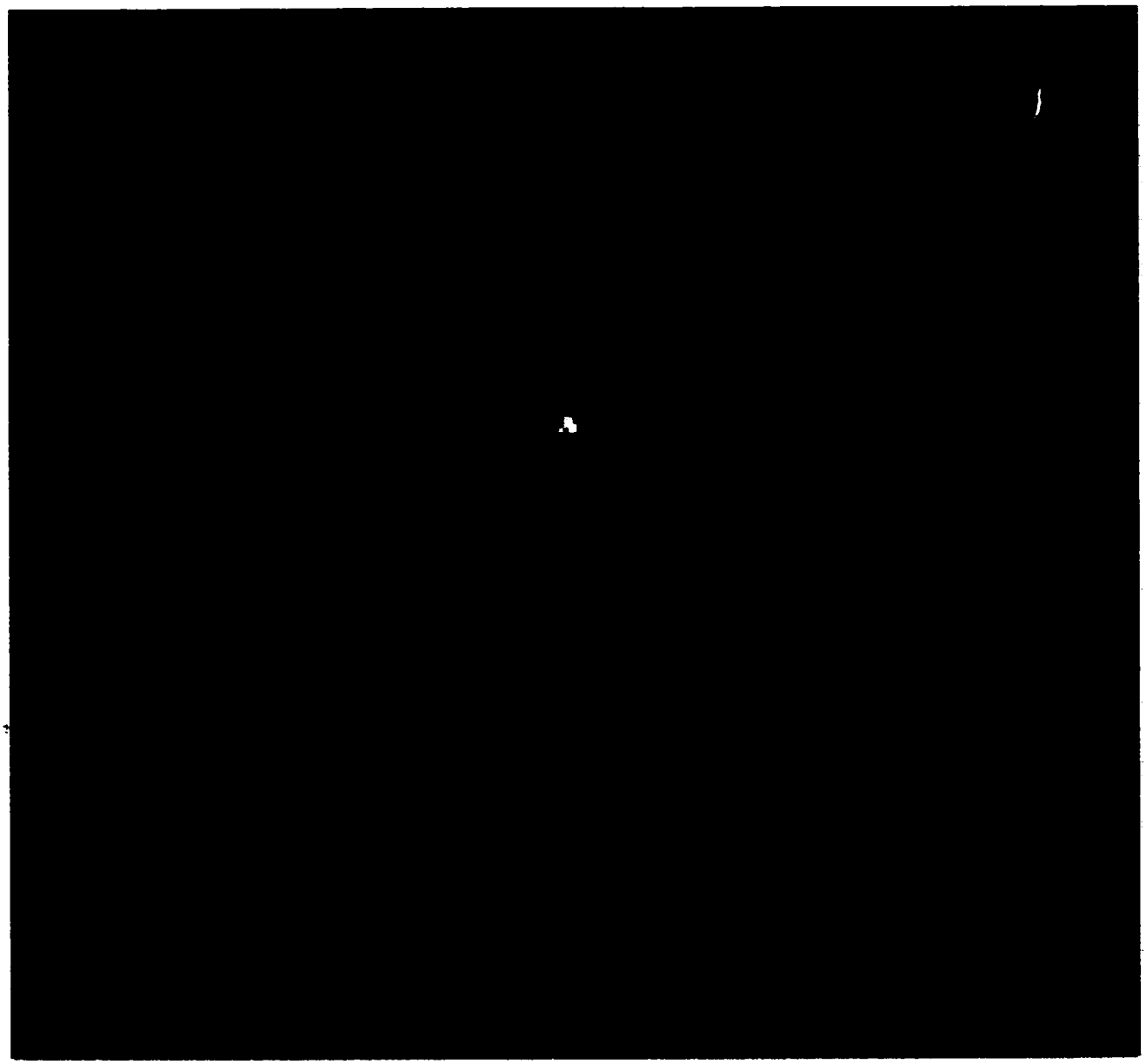

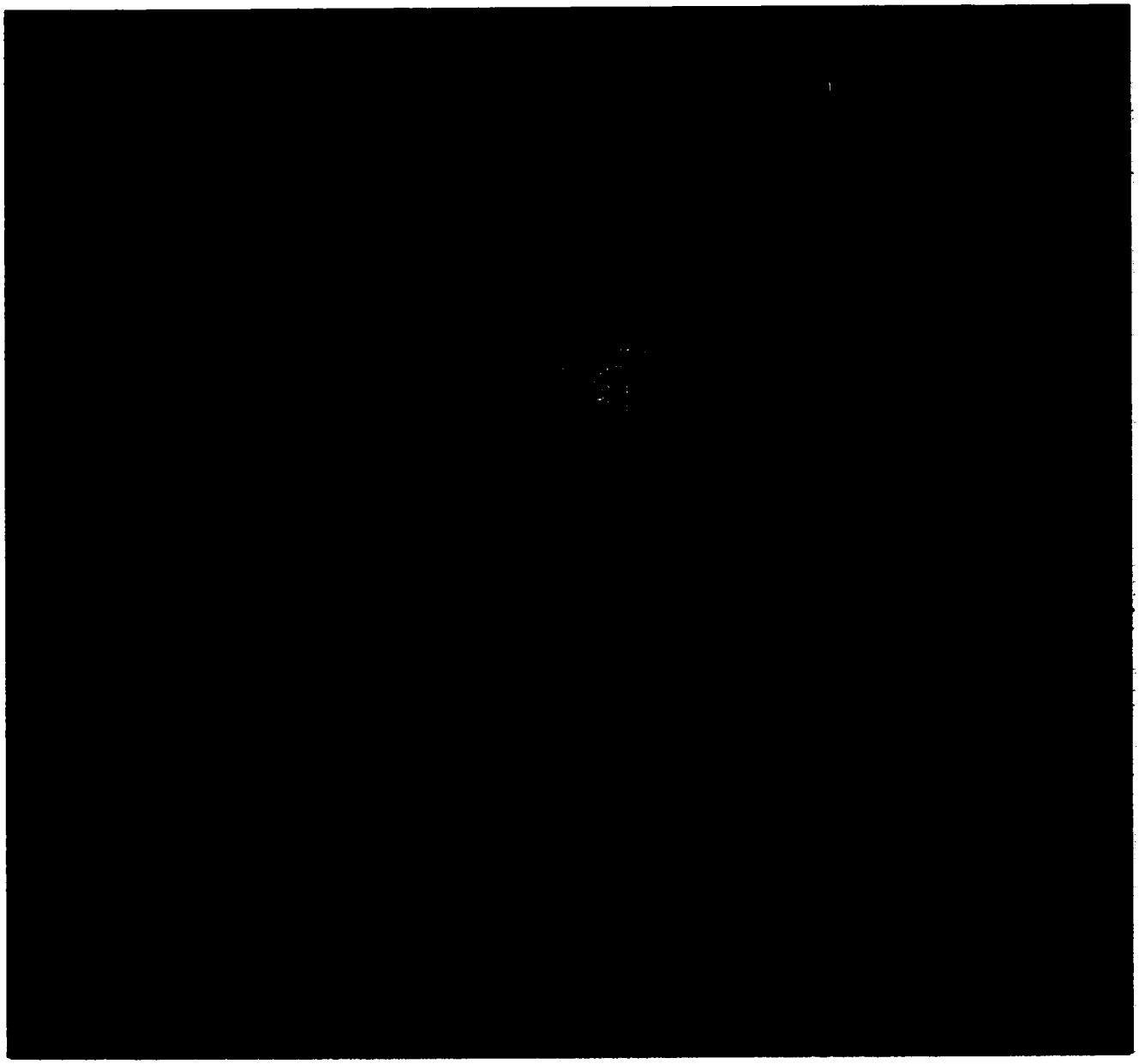

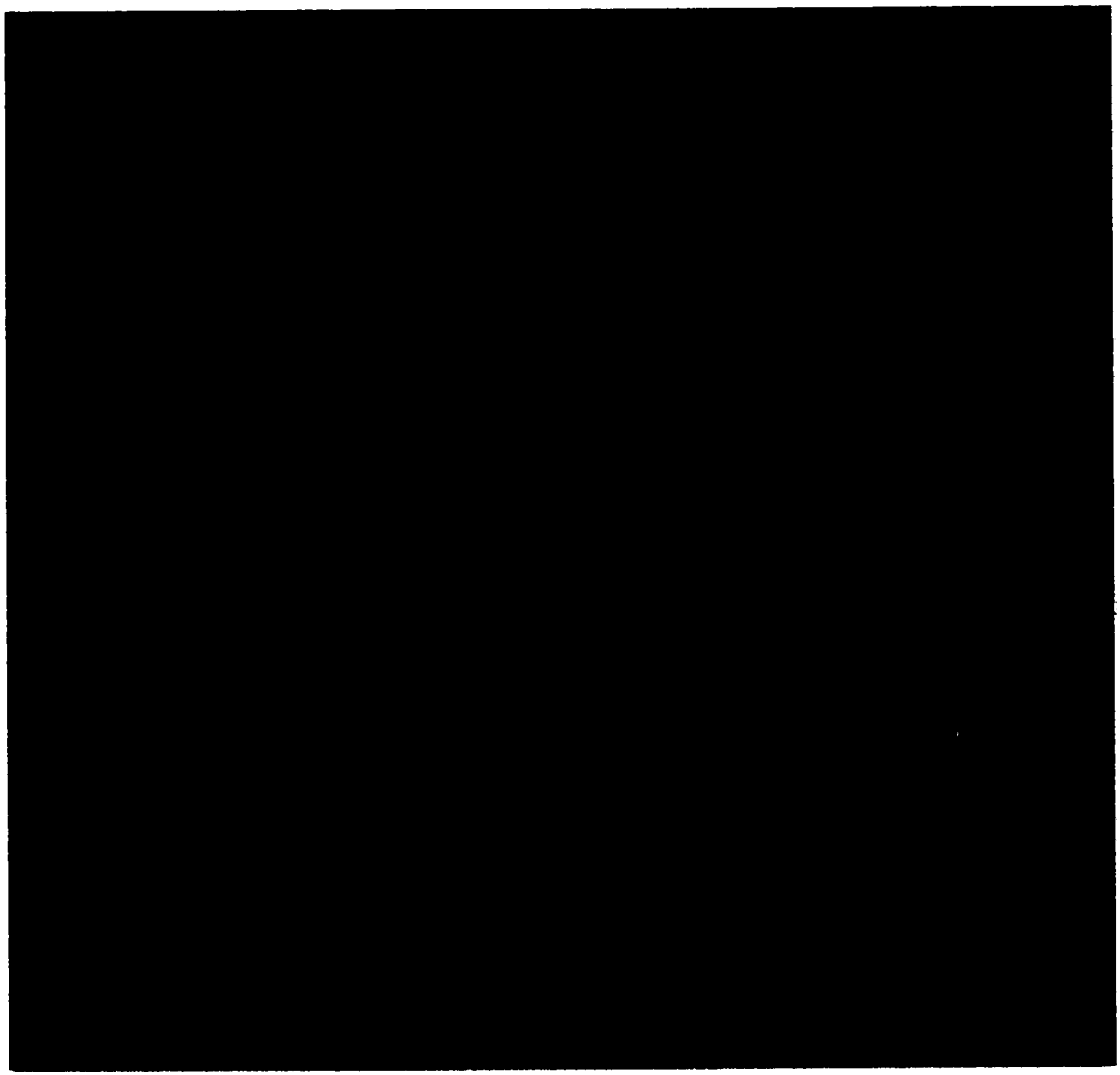

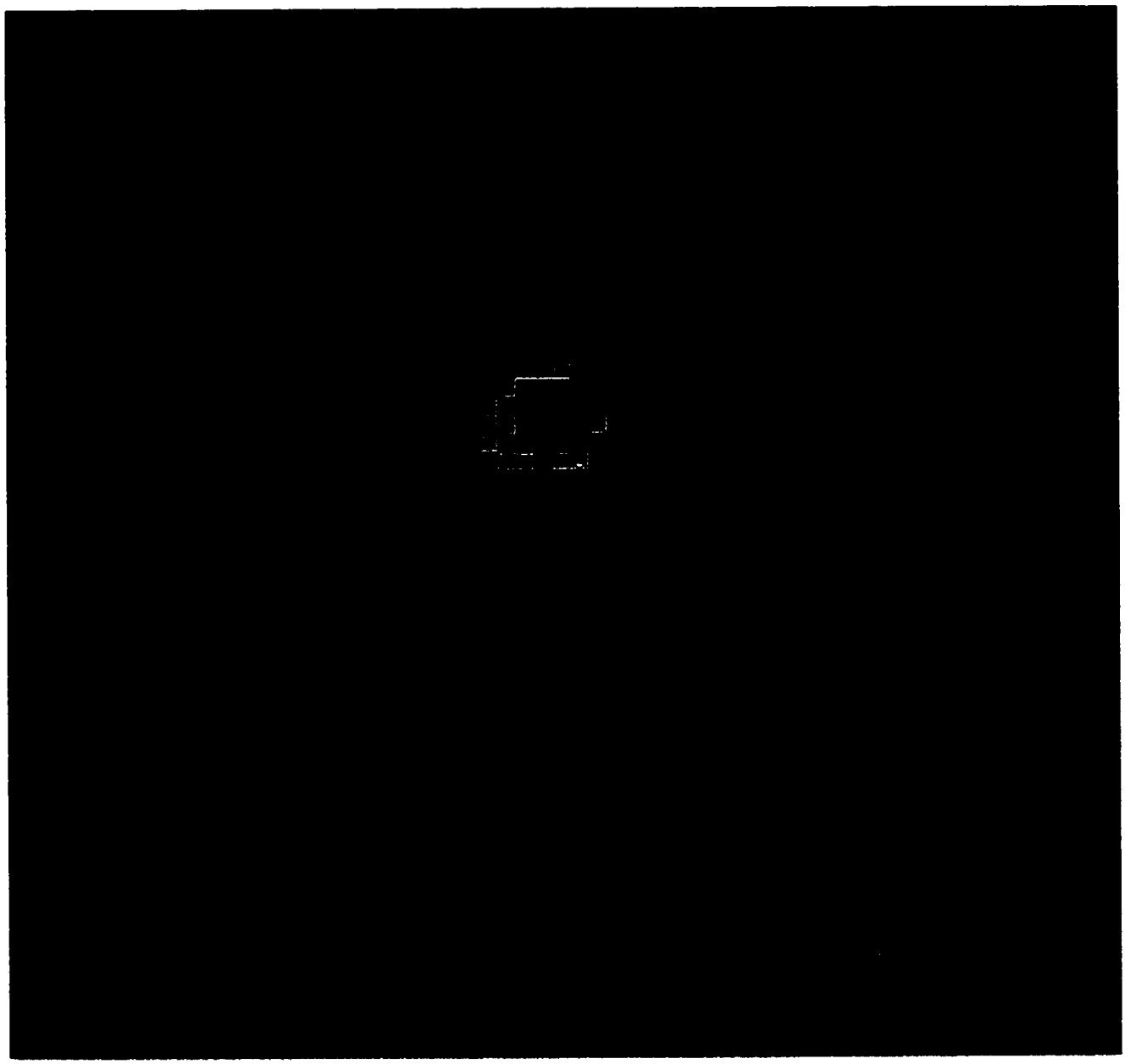

IMAGE EVALUATION
TEST TARGET (QA-3)

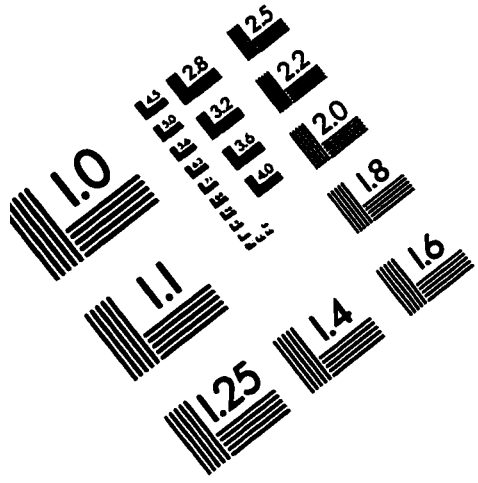

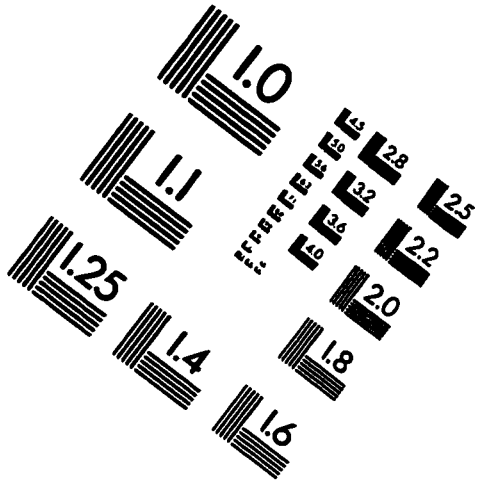

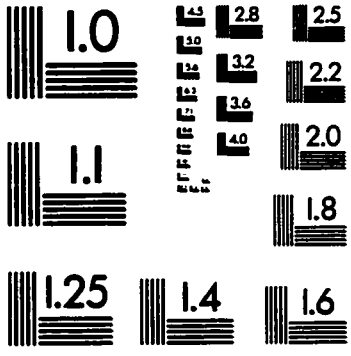

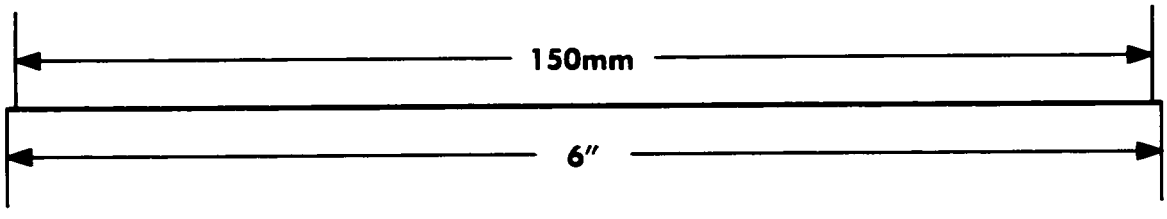

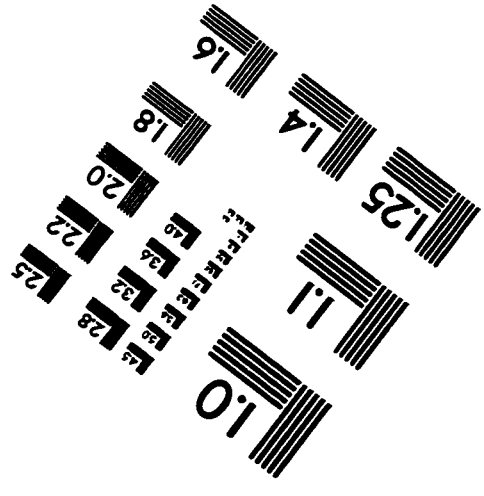

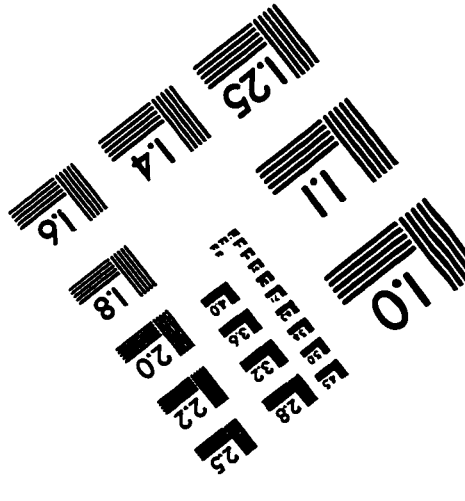

APPLIED IMAGE, Inc
1653 East Main Street
Rochester, NY 14609 USA
Phone: 716/482-0300
Fax: 716/288-5989